

**Modeling of complex surface interactions in low  
and high pressure plasmas**

by

**Mingmei Wang**

A dissertation submitted to the graduate faculty  
In partial fulfillment of the requirements for the degree of  
DOCTOR OF PHILOSOPHY

Major: Chemical Engineering

Program of Study Committee:  
Mark J. Kushner, Major Professor  
Rodney O. Fox  
Monica H. Lamm  
Vikram L. Dalal  
Baskar Ganapathysubramanian

Iowa State University

Ames, Iowa

2011

Copyright © Mingmei Wang, 2011. All rights reserved.

## TABLE OF CONTENTS

	Page
ACKNOWLEDGEMENTS.....	v
ABSTRACT.....	vii
CHAPTER 1. INTRODUCTION .....	1
1.1 Plasma Etching.....	1
1.2 Plasma Modeling .....	4
1.3 Issues in High Aspect Ratio (HAR) Feature Etching .....	4
1.4 Reaction Mechanisms and Proposed Solutions .....	6
1.5 Functionalization of Pore Surfaces in Thin Membranes.....	8
1.6 Summary .....	10
1.7 Figures.....	14
1.8 References.....	23
CHAPTER 2. DESCRIPTION OF THE MODEL .....	30
2.1 Hybrid Plasma Equipment Model (HPEM).....	30
2.1.1 Introduction.....	30
2.1.2 The Fluid Kinetics Module (FKM).....	30
2.1.3 The Electron Monte Carlo Simulation (EMCS) .....	34
2.1.4 Plasma Chemistry Monte Carlo Module (PCMCM) .....	36
2.2 Monte Carlo Feature Profile Model (MCFPM).....	39
2.3 nonPDPSIM .....	48
2.4 Figures.....	51
2.5 References.....	54
CHAPTER 3. HIGH ENERGY ELECTRON BEAMS IN DC-AUGMENTED CAPACITIVELY COUPLED PLASMAS I: FUNDAMENTAL CHARACTERISTICS .....	57
3.1 Introduction.....	57
3.2 Capacitively Coupled Plasmas with DC Augmentation .....	58
A. High Energy Electron Distributions.....	60
B. Collection of dc Current.....	66
C. Two Frequency CCP .....	70
D. Low Frequency .....	71
3.3 Concluding Remarks.....	72
3.4 Figures.....	75
3.5 References.....	85

CHAPTER 4. HIGH ENERGY ELECTRON FLUXES IN DC-AUGMENTED CAPACITIVELY COUPLED PLASMAS II: EFFECTS ON TWISTING IN HIGH ASPECT RATIO ETCHING OF DIELECTRICS .....	86
4.1 Introduction.....	86
4.2 Bulk Plasma Properties.....	89
4.3 Effect of Charging and HEE fluxes on Profiles of HAR Features .....	92
4.4 Concluding Remarks.....	99
4.5 Figures.....	101
4.6 References.....	112
CHAPTER 5. MODELING OF IMPLANTATION AND MIXING DAMAGE DURING ETCHING OF SiO <sub>2</sub> OVER SI IN FLUOROCARBON PLASMAS .....	114
5.1 Introduction.....	114
5.2 IEADs Onto the Wafer.....	117
5.3 Validation of the Model.....	118
5.4 Scaling of Implantation and Mixing .....	120
5.5 Concluding Remarks.....	127
5.6 Figures and Tables .....	129
5.7 References.....	143
CHAPTER 6. ELIMINATING OF POLYMETHYLMETHACRYLATE (PMMA) DEGRADATION BY VUV EXPOSURE AND SI DEPOSITION IN DIELECTRIC ETCHING.....	145
6.1 Introduction.....	145
6.2 Scaling of Etch Selectivity.....	146
6.3 Strategies to Eliminate PR Erosion.....	148
6.3.1 Scaling of Si and VUV Fluxes with DC Power.....	150
6.3.2 Effects of Si and VUV fluxes on PR erosion.....	151
6.3.3 Flux Sensitivity .....	151
6.4 Concluding Remarks.....	152
6.5 Figures.....	154
6.6 References.....	164
CHAPTER 7. PLASMA BREAKDOWN IN INNER PORES OF THIN POROUS MEMBRANES .....	165
7.1 Introduction.....	165
7.2 Plasma Properties in 50- $\mu$ m-thick Membranes.....	168
7.2.1 Gas Breakdown in Unconnected Pores.....	168
7.2.2 Gas Breakdown in Connected Pores.....	169

7.3	Gas Breakdown in Highly Interconnected Pores in 600- $\mu\text{m}$ -thick Membranes.....	171
7.4	Gas Breakdown in Highly Interconnected Pores in 300- $\mu\text{m}$ -thick Membranes.....	173
7.5	Critical Dimension for Plasma Propagation .....	174
7.5.1	0.1- $\mu\text{m}$ -wide ‘Neck’ without Thickness .....	174
7.5.2	0.1- $\mu\text{m}$ -wide and 1- $\mu\text{m}$ -thick ‘Neck’ .....	174
7.6	Concluding Remarks.....	175
7.7	Figures.....	177
7.8	References.....	187
	AUTHOR’S BIOGRAPHY .....	188

## ACKNOWLEDGEMENTS

I would like to express my deepest gratitude to my advisor Prof. Mark J. Kushner for all his help and guidance. I am grateful to him for being patient with me and encouraging and motivating me during difficult times. I am thankful to him for introducing me to the world of plasma physics and for providing me numerous chances to interact with the world's leading engineers and scientists. I have learned tremendous knowledge from him. His scientific attitude and working enthusiasm, I believe, will continue to inspire me in my future career life.

I am grateful to the faculty members of my POS committee – Prof. Rodney O. Fox, Prof. Monica H. Lamm, Prof. Vikram L. Dalal and Prof. Baskar Ganapathysubramanian for their thoughtful comments and suggestions. I acknowledge Dr. Lin Xu for his professional and career guidance. I would also like to acknowledge the support of the Semiconductor Research Corporation, Micron Technology Inc., Tokyo Electron Ltd., and 3M Corp.

I am thankful to the past and present members of the Optical and Discharge Physics Group for their friendship and support –Dr. Peter Ventzek, Dr. Wenli Z. Collison, Dr. Ananth Bhoj, Dr. Ramesh Arakoni, Dr. Ankur Agarwal, Dr. Yang Yang, Dr. Natalia Baeva, Dr. Zhongmin (Andy) Xiong, Dr. Julia Falkovitch-Khain, Juline Shoeb, Junchieh (Jerry) Wang, Sang-Heon Song, Michael Logue, Yiting Zhang and Wei Tian. Special thanks to Paul Jewell at ISU and Jonathan Plummer at U of M for arranging the video-conference. I'd also like to thank Dilok Phanchantraurai in ISS office, Christi Paterson in

CBE department at ISU, Michelle Chapman and Karla Johnson in EECS department at U of M for helping with paperwork during my Ph.D. study.

Thanks must go to my parents, my brother and sister-in-law, my lovely niece Tongtong, and my parents-in-law. What they've done for me could never be expressed adequately in words. Their consistent and selfless support during my Ph.D. study makes the whole story becomes true. Thanks also go to my fiends, Ling Li, Dongdong Peng, Yanjie Zhang, Yanxiang Shi, Bingqi Zhang, Caizhi Zhou, and Yi Ying, with whom my life becomes more colorful and joyful.

Finally, my love and gratitude go to my family: my husband Dr. Xinghua Sun and my son Kevin Sun, both of whom are the most precious asset in my entire life. With you, my life is full of warmth, happiness, and hope. So, I dedicate this thesis to them.

## ABSTRACT

Plasma etching (or dry etching) is widely used in the fabrication of integrated circuits (IC). Anisotropic features are easily obtained by controlling reactive ion trajectories in plasma. Twisting and bowing are two main issues during high aspect ratio (HAR) feature etching. Twisting is, instead of a feature etching vertically, the feature twists or turns to the side. Mixing damage by ion bombardment of underlying materials is also a critical problem in post-etch processing. One of the explanations for twisting is charge accumulation on feature surfaces during ion bombardment. An asymmetric local electric field (E-field) changes ion trajectories incident into the feature to one direction opposite the E-field. This causes twisting. Bowing at the top of the feature near the mask-SiO<sub>2</sub> interface mainly results from bombardment of ions reflecting from eroded mask surface. Ions with energies of many keV are required for HAR etching to get a high etch rate and a straight profile. While, if the ion energy is too high, it will penetrate into the under layer material and produce mixing damage during over etch.

Our research goals are to propose mechanisms to help eliminate twisting by applying high energy electron (HEE) beams, to reduce bowing by protecting the pattern-transferring material photoresist (PR), and to minimize post-etching damage by optimizing operating conditions in HAR etching.

A dc augmented capacitively coupled plasma (CCP) reactor is simulated using the Hybrid Plasma Equipment Model (HPEM) to generate energetic ions as well as HEE beams in Ar/C<sub>4</sub>F<sub>8</sub>/O<sub>2</sub> gas mixture. Energy and angle distributions and fluxes for reactive species obtained from the HPEM are then input into the Monte Carlo Feature Profile

Model (MCFPM) to investigate surface interactions in sub-micron to nano-scale feature etching. HEE generated from secondary emission of the top electrode surface due to ion bombardment is shown to have the ability of neutralizing positive charges accumulated deep into the trench and eliminating twisting. Increasing dc power applied on the top electrode produces more HEE beams with higher energy, which results in a decrease in twisting frequency.

Implantation induced mixing damage is also simulated in the MCFPM by incorporating an IMPLANT model. The depth of implanting and mixing scales with rf power and ion energy. As such, there will be a tradeoff between high etch rate and low post-etch damage during etching at high bias power.

Ion bombardment can degrade the pattern transferring material, usually a polymer photoresist (PR), and, at the same time, it can induce cross-linking of the PR surface. Cross-linked PR surfaces are more resistive to etch than normal PR. More energetic ion sputtering leads to a higher etching selectivity of  $\text{SiO}_2/\text{PR}$  while the PR is eventually eroded in HAR etching. A strategy to protect the PR is to generate Si radicals and VUV photons. Si is generated in the same way as HEE by ion sputtering of the top electrode. Si-C rich layer and Si extracting of F atoms from  $\text{C}_x\text{F}_y$  polymer on the PR surface may produce an etch stop if the Si flux is sufficiently high. VUV photons could be absorbed by PR surface and generates cross-linking. VUV and Si fluxes together have a synergetic effect of protecting the PR and eliminating bowing.

By functionlizing the surface of polymers, we can increase their surface reactivity to favor the adhesion of metals or other compounds on their surface, enhance their wet-

tability or modify their biocompatibility by grafting on their surface specific chemical groups. Functionalization of inner pore surfaces in porous membranes is challenging because the strong electric field (100's kV/cm to 1MV/cm) formed in thin membranes could damage it. Gas breakdown in the inner pores in porous polymeric materials is investigated in air using nonPDPSIM. Since photoionization is one of the dominant ionization mechanisms in small pores or porous channels in thin membranes, increasing photoionization cross section can produce ionization across sharp angles and promote plasma propagation. Electrode shape also affects plasma propagation direction. A round electrode is more likely to generate horizontal elements for the electric field and produce more ionization horizontally. When fixing the ration of electric field to gas number density,  $E/N$ , different gas pressure and bias voltage combinations favor different plasma propagation paths. Higher gas pressure produces higher plasma density which helps the plasma penetrate narrow and thick 'necks' in porous channels.

# 1. INTRODUCTION

## 1.1 Plasma Etching

Plasmas are partially ionized gases, which are typically electrically conductive. Since there is a small amount of electron loss to the walls of bounding containers, plasmas are quasi-neutral on the whole. Densities of the charged species (ions and electrons) are far less than the densities of the neutral species in plasmas, but these densities are sufficient to respond strongly to electromagnetic fields. The energy loss of electrons is neglectable during electron-neutral momentum transfer collisions due to their much smaller mass than that of neutrals. Thus, the free electrons are accelerated to high energies (a few electron volts) sufficient to have inelastic collisions with the gas atoms and molecules. Ionization and excitation of the gas atoms and molecules occur when electron energies exceed the threshold energies of these inelastic collisions.

The development of microelectronics industry has obeyed Moore's law (Fig. 1.1) since the 1970's [1]. The law states that the number of transistors in microprocessors or their functionality doubles approximately every two years. It becomes a necessary to shrink the size of devices and features to improve their capabilities. The process of fabricating these devices may involve hundreds of steps, which is much more complicated than its first onset. The critical dimensions (CDs) of transistors (that is, the tolerances that fabrication of transistors must meet) have shrunk to tens of Å (a few atomic monolayers), which requires more precise and controllable processing of semiconductor materials. Plasma processing of semiconductors (e.g. plasma etching, plasma enhanced chemical vapor deposition [PECVD]) is widely used to meet such needs [2]. Chemically

reactive plasma discharges are widely used for manufacturing very large scale integrated circuits (VLSIs) used in the electronics industry. The primary advantage of plasma-assisted etching (dry etching) over chemical etching (wet etching) is the anisotropic etching of small features in microelectronics fabrication (See Fig. 1.2).

Reactive ion etching (RIE) is a typical dry etching technology widely used in semiconductor processing. In a RIE reactor, the wafer is placed on a substrate inside a vacuum chamber. Feedstock gases are introduced into the reactor from a nozzle or showerhead. Plasmas are generated in the chamber by application of a radio frequency (rf) power source. The ions in the plasma are then accelerated towards the wafer by the applied rf bias voltage on the substrate. The ions react with the wafer surface material forming volatile products thereby etching the wafer. This is the chemical part of reactive ion etching. There is also a physical part, which is known as sputtering. The energetic particles, including ions, neutrals and radicals, can knock atoms of the target material out of the lattices. Among these processes, positive ion bombardment is thought to be most beneficial. Negative ions are excluded because they are not energetic enough to overcome the sheath potential barrier and reach the wafer. Product volatility is also a necessary condition for etching to occur. Otherwise, the products may block the surface due to redeposition and the reaction may be forced to stop.

When etching high aspect ratio (HAR) structures, the feature profile is much more difficult to control than low aspect ratio features [3]. Effects such as aspect ratio dependent etching, microtrenching [4], notching [5], and charging [6–9] have been intensively investigated. On the one hand, ions and neutrals may collide within the sheath near the

wafer surface, resulting in dispersion of their angular distribution and thereby increasing the interaction of the species with the sidewalls to cause deviation from the ideal etching profile. High plasma densities (small Debye lengths and thin sheaths) and low gas pressure (long mean free paths) significantly reduce the probability of collisions in the sheath region, which leads to anisotropic etching. Also, low gas pressure facilitates diffusion and promotes uniformity over large diameter substrates so that more uniform etching can be achieved. In addition, the etched features may be non-uniformly charged. The upper part of the feature is locally charged by the ions that first enter the trench, and this local charge deflects the trajectory of incident ions and reduces the flux reaching the trench bottom. Thus, the etching rate decreases, and the feature profile twists at high aspect ratio due to a wide angle spread for incident species.

The goal of any plasma etching process is to achieve a satisfactory (meaning high) etching rate [10], uniformity [11], selectivity [12, 13], anisotropy [14] and to avoid any radiation damage [15, 16]. Choosing appropriate operating parameters is necessary to achieve these goals – and typically involves a tradeoff between these attributes. People can adjust operating parameters to optimize the etching performance if the reactor's dimensions and construction materials are already given. The parameters include gas mixture [17], flow rate [18], pressure [13], rf bias power [12, 19], self-bias voltage [10], and excitation frequency [20]. As such, it is extremely difficult and expensive to exhaustively adjust these parameters to identify the optimal set of operating conditions. The shrinking size of devices (approaching only a few nanometers) makes the problem more

complex than before. As a result, plasma modeling becomes more attractive in the semiconductor industry than before to guide the experimental process.

## 1.2 Plasma Modeling

Plasma modeling originated from global and 1-dimensional (1-D) models, which are used to represent the basic physical processes in plasmas. Two-dimensional (2-D) models appeared a few years later targeting both process and equipment design [21-31]. Three-dimensional (3-D) [32] modeling is attracting more attention these days due to the availability of faster computational sources than in the past. These models typically address reactor scale or bulk plasma properties. There are also feature scale models (100's  $\mu\text{m}$  to a few  $\text{\AA}$ ) to simulate the surface interactions and topographies. The reactor scale models are often linked to feature scale models and perform self-consistent modeling. There are three dominant algorithms in feature scale: string models [33, 34], Monte Carlo models [35-43] and Molecular Dynamics models [44-47].

## 1.3 Issues in High Aspect Ratio (HAR) Feature Etching

The successful use of radio frequency (rf) capacitively coupled plasmas (CCPs as shown in Fig. 1.3) for the etching of materials during microelectronics fabrication is predicated on being able to control the energy and angular distributions of reactant species to the wafer [48]. In these devices, an rf voltage is applied to a parallel-plate reactor filled with gases with pressures of 10s to 100s of mTorr. A plasma is produced that produces fluxes of radicals and ions to the wafer. The neutrals react with the wafer with activation energy provided by the ions. In conventional single frequency CCPs, there is a tradeoff between controlling the ion energy and angular distribution (IEAD) and the rate

of plasma production (and so radical flux to the substrate) as a function of excitation frequency and gas pressure [49]. More advanced two-frequency CCPs separate these functions by attempting to control the IEAD using low frequency (LF) excitation ( $< 10$ s of MHz) and using a high frequency (HF) excitation ( $> 10$ s of MHz) to control the production of the plasma and so the magnitude of fluxes to the substrate [50].

New designs of CCPs are intended to provide additional control of the reactant fluxes to the substrate. One such example is a dc-augmented CCP (dc-CCP) [51–54]. In this design, the electrode opposite the wafer is biased with a dc voltage ( $V_{dc}$ ) with the intent of producing a high energy electron (HEE) beam having a narrow angular distribution onto the wafer. The HEE is thought to have beneficial effects in controlling the profile of high aspect ratio features during plasma etching. Since the dc biases for dc-CCPs operating at 10s of mTorr are typically many hundreds of volts, ion acceleration into the dc electrode, typically made of Si, can also sputter Si atoms into the plasma. As such, the dc-CCP can also provide some additional control over reaction chemistry.

Plasma etching of high aspect ratio features for microelectronics fabrication is challenging state-of-the-art practices to obtain reproducible features with straight walls and definable shapes. For example, holes with diameters of 10s of nm with aspect ratios (AR) in excess of 70 are being fabricated for memory cells in large arrays. One of the challenging aspects of these processes is preventing the errant and nearly random occurrence of features that twist [55]. This often occurs after a significant fraction of the feature has already been etched. The direction of twisting, its frequency of occurrence and its proximity to other twisted features typically occurs randomly with no discernable pat-

tern (See Fig. 1.4). The feature-to-feature etch rate can also vary significantly.

Bowing is another anomalous behavior in which the sides of the feature bow out late during the etching process [56, 57]. Bowing, however, is typically a more reproducible and systematic effect. As shown in Fig. 1.4, the feature-to-feature bowing has less variation than the twisting and etch rate. Bowing is attributed to the change in the acceptance angle of ions into the feature from the plasma due to erosion of the photoresist (PR, usually is a C-H based polymer) mask and subsequent reflection of ions from the facets of the PR.

#### 1.4 Reaction Mechanisms and Proposed Solutions

Fluorocarbon plasma etching of SiO<sub>2</sub> has 3 dominant steps:

- $\text{SiO}_2(\text{s}) + \text{C}_x\text{F}_y^+(\text{g}) \rightarrow \text{SiO}_2^*(\text{s}) + \text{C}_x\text{F}_y(\text{g})$
- $\text{SiO}_2^*(\text{s}) + \text{C}_x\text{F}_y(\text{g}) \rightarrow \text{SiO}_2\text{C}_x\text{F}_y(\text{s})$
- $\text{SiO}_2\text{C}_x\text{F}_y(\text{s}) + \text{C}_x\text{F}_y^+(\text{g}) \rightarrow \text{SiF}_y(\text{g}) + \text{CO}_2(\text{g}) + \text{C}_x\text{F}_y(\text{g})$
- Further deposition by C<sub>x</sub>F<sub>y</sub>(g) produces thicker polymer layers.

A schematic of the reaction mechanism is shown in Fig. 1.5 [58]. The C<sub>x</sub>F<sub>y</sub> polymer layer is also called a passivation layer, which is used to protect side walls and control the etching rate during HAR etching. Si is used as the stop-layer under SiO<sub>2</sub>. Si etching is mainly through F reactions:

- $\text{Si}(\text{s}) + \text{F}(\text{g}) \rightarrow \text{SiF}_x(\text{g})$

where  $x = 1-4$ . When  $x = 1-3$ ,  $\text{SiF}_x$  is solid.  $\text{SiF}_4$  is volatile.

The etching selectivity for  $\text{SiO}_2$  over Si is caused by  $\text{C}_x\text{F}_y$  polymer deposition. C atoms in  $\text{C}_x\text{F}_y$  gas can react with  $\text{SiO}_2$  and produce volatile species  $\text{CO}_2$ . While on Si surfaces,  $\text{C}_x\text{F}_y$  can only produce polymer deposition. F atoms need to diffuse through a thicker polymer layer to reach the Si surface than to the  $\text{SiO}_2$  surface. The etching selectivity for  $\text{SiO}_2$  over Si is can be larger than 100. It can even be infinite due to an etch stop caused by the thick  $\text{C}_x\text{F}_y$  polymer layer on Si surface in low energy etching case.

One possible explanation for twisting is errant charging and dc-CCPs have been proposed as a remedy [52, 54]. As the feature size shrinks to have an opening area of only 100s of  $\text{nm}^2$  the rate of entry of radicals and ions into the feature begins to become statistical. For example, the time between the arrivals of two ions into a feature of 50 nm in diameter for a flux of  $10^{16} \text{ cm}^{-2} \text{ s}^{-1}$  is 5  $\mu\text{s}$ . This small rate of particle arrival leads to feature-to-feature statistical variations in the neutral and charged fluxes entering a single feature. Ions arriving onto the wafer after acceleration through the sheath have a narrower angular distribution than thermal electrons. The end result is that ions penetrate deeper into features, producing random charging and electric fields that may deflect subsequent ions and produce twisting. The HEE flux with its narrow angular distribution may be able to penetrate into HAR features and possibly neutralize this errant positive charge.

One of the proposed bowing mechanisms is a result of ion-induced changes in the slope of the PR surface [59]. Energetic ions impacting onto the PR surface reflect to the side walls of trenches as shown in Fig. 1.6. The PR initially usually has a domed shape

that does not reflect many energetic ions into the trench side walls since the PR is thick compared to the trench size. As etching proceeds, the PR is eroded. When the PR is thin enough, bowing occurs due to reflection off the facets. Multi-layer masks (PR-hard mask) and deposition of a passivation layer onto the PR surface are thought to protect the PR from being eroded. Ion bombardment and VUV (vacuum ultraviolet radiation) exposure induced a cross-linked surface can also make the PR more resistive to etch.

Anisotropic ions with high energy are required for HAR etching. As the ion energy increases, small ions will penetrate through the passivation layer on the surface and implant into the underlying material (See Fig. 1.7). Implanting of small particles can destroy the crystal structures and producing mixing as the particles travel through these lattices. Implanting and mixing usually happens at the bottom of trenches since ions are anisotropic. This will lead to damage to the under layer (Si here) of processing. Thus the etching rate and post-etch damage have to be balanced during HAR etching.

### **1.5 Functionalization of Pore Surfaces in Thin Membranes**

Plasma treatment is a potentially attractive method for modifying the surface characteristics of a polymer without affecting the bulk properties of the material [60–63]. Plasma treatment also has the advantages of short treatment durations and room temperature operation. Functionalization of polymers can increase their surface reactivity to favor the adhesion of metals or other compounds on their surface, enhance their wettability, or modify their biocompatibility by grafting on their surface specific chemical groups [64–66]. Surface functionalization uses reactive species including ions, electrons, radicals, and photons generated in the plasmas. Atmospheric pressure corona discharges [67,

68] in a dielectric barrier configuration are widely used for this purpose. They are relatively easy to implement and effective for treating large area materials. A typical plasma source is shown schematically in Fig. 1.8. Depending on the gas composition or pulsing frequency [69-71], discharges generated at atmospheric pressure may be either diffusive or filamentary. Gas mixtures, such as air or O<sub>2</sub> containing gases, as well as Ar, He, N<sub>2</sub>, and NH<sub>3</sub> plasmas have been used for polymer surface functionalization [72–78]. Functionalization of polymer surfaces has been investigated in these plasmas for different polymer materials [79-87].

Functionalization of inner pore surfaces in porous polymer materials or woven/non-woven fibers has rarely been reported. There are many challenges to achieve this goal. Internal pores or inter-pore gaps in these materials have dimensions of 10s of  $\mu\text{m}$  to only a few  $\mu\text{m}$ . The initiation of plasmas is governed by Paschen's Law which states that the breakdown voltage of a gap is a function of the product of the gas pressure and the gap size,  $V = f(pd)$ , as seen in equation 1.1 and Fig. 1.9.

$$V_b = \frac{a(pd)}{\ln(pd) + b} \quad (1.1)$$

where  $p$  is the pressure (in Torr) and  $d$  is the gap distance (in cm). Typical  $pd$  values for minimum voltages are:  $pd = 0.5\sim 2$  Torr-cm. For pores of a few  $\mu\text{m}$  in porous membrane, the minimum voltage occurs at pressures of 5-10 atm, and the corresponding electric fields are 100s kV/cm to 1 MV/cm. Such high electric fields would approach the dielectric strength of materials to be treated. Also, large surface-to-volume ratios of internal

structures of porous membrane lead to large plasma losses, which challenge the ability to maintain plasma.

Porous membranes, polyvinylidene difluoride (PVDF), for example, are drawing more attention for their applications in micro-filter, ultra-filter or ion-exchange membranes. PVDF, which is naturally hydrophobic, has advantages including high porosity, thermal stability, chemical resistance, mechanical strength, and low cost etc. Membrane chromatography has higher mass-transfer efficiency, lower pressure drop, and better scalability than traditional packed-bed chromatography [88]. Plasma treatment of PVDF is capable of switching it from hydrophobic to hydrophilic and from bio-resistant to bio-compatible by grafting on its surface with different functional groups. Modeling of plasma development and propagation in these porous membranes may help to understand the mechanisms and optimize the operating conditions to guide the experiments and reduce the costs.

## 1.6 Summary

In this thesis, I report on computational investigations of reducing twisting frequency, understanding the mechanisms of post-etch damage, avoiding bowing in high aspect ratio etching of  $\text{SiO}_2$  using low pressure  $\text{Ar}/\text{C}_4\text{F}_8/\text{O}_2$  plasmas and gas breakdown conditions in porous membranes using atmospheric pressure air plasmas. We found that high energy electron (HEE) beams can penetrate deep into features and neutralize positive charge there to achieve a much lower twisting frequency than etching without HEEs. Mixing due to energetic ion bombardment and implantation produces damage to underlying material. The mixing depth scales proportionally to ion energy and bias power. En-

ergetic ion bombardment and VUV exposure induced cross-linking of the photoresist (PR) surface is able to protect the PR. Deposition of a hard mask layer (Si here) onto the PR surface is also an effective way to prevent the PR from being etched. Breakdown voltages in thin porous membranes are comparable to the theoretical values calculated from Paschen's Law. Higher breakdown voltages in our model compare to the theoretical values are due to a 1% humidity and huge electron losses to the dielectric walls.

This thesis is organized as follows:

In Chapter 2, the modeling algorithms in the 2-D models including the reactor scale Hybrid Plasma Equipment Model (HPEM), the Monte Carlo Feature Profile Model (MCFPM) for low pressure plasma modeling and the nonPDPSIM for atmospheric pressure plasma modeling will be discussed in detail.

In Chapter 3, the characteristics of dc-CCPs will be discussed using results from a computational study. We found that for a given rf bias power, beams of high energy electrons (HEEs) having a narrow angular spread ( $<1^\circ$ ) can be produced incident on the wafer. The maximum energy in the high energy electron flux scales as  $\varepsilon_{max} = -V_{dc} + V_{rf} + V_{rf0}$ , for a voltage on the dc electrode of  $V_{dc}$ , rf voltage of  $V_{rf}$ , and dc bias on the rf electrode of  $V_{rf0}$ . The dc current from the biased electrode must return to ground through surfaces other than the rf electrode and so seeks out a ground plane, typically the side walls. If the side wall is coated with a poorly conducting polymer, the surface will charge to drive the dc current through.

In Chapter 4, we report on results from a computational investigation of plasma etching of  $\text{SiO}_2$  in a dc-CCP using  $\text{Ar}/\text{C}_4\text{F}_8/\text{O}_2$  gas mixtures. We found that HEE beams incident onto the wafer are capable of penetrating into features and partially neutralizing positive charge buildup due to sporadic ion charging, thereby reducing the incidence of twisting. Increasing the rf bias power increases the HEE beam energy and flux with some indication of improvement of twisting, but there are also changes in the ion energy and fluxes, so this is not an unambiguous improvement. Increasing the dc bias voltage while keeping the rf bias voltage constant increases the maximum energy of the HEE and its flux while the ion characteristics remain nearly constant. For these conditions, the occurrence of twisting decreases with increasing HEE energy and flux.

In Chapter 5, we implement an implantation and mixing model into the MCFPM to simulate the mixing and damage to the underlying Si during high aspect ratio (HAR) etching of  $\text{SiO}_2$  trenches. Fluxes to the surface are provided by HPEM. The feature scale model is validated by Molecular Dynamics (MD) simulations. Scaling of mixing damage in underlying Si during HAR of  $\text{SiO}_2$  etching in  $\text{Ar}/\text{C}_4\text{F}_8/\text{O}_2$  plasmas for rf bias powers of 1 kW~4 kW will be discussed. We found that mixing damage at the bottom of HAR features, though increasing in magnitude with increasing ion energy, does not scale as dramatically as on flat surfaces. This is due to the reflection of ions off side walls, which moderate the ion energies.

In Chapter 6, we discuss methods to protect photoresist (PR) from erosion and so minimize detrimental effects such as bowing. The methods include energetic ion bombardment, Si deposition and VUV exposure. Ion sputtering and VUV exposure can de-

grade the PR polymer chain and induce cross-linking at the same time. Cross-linked PR surfaces are more resistive to etch than normal PR. Si fluxes obtained in a dc-CCP reactor can form Si-C bonds or extract F atoms from the  $C_xF_y$  polymer, which promotes further polymer deposition. The Si-C rich layer combined with a thicker  $C_xF_y$  polymer layer can lead to an etch stop if the Si flux is sufficiently high.

In Chapter 7, gas breakdown in different pores or porous channels in thinner and thicker membranes will be discussed. The breakdown conditions depend on the thickness of the membrane and the size of pores or porous channels. Different plasma properties under different gas pressure and different voltage will also be discussed in this chapter.



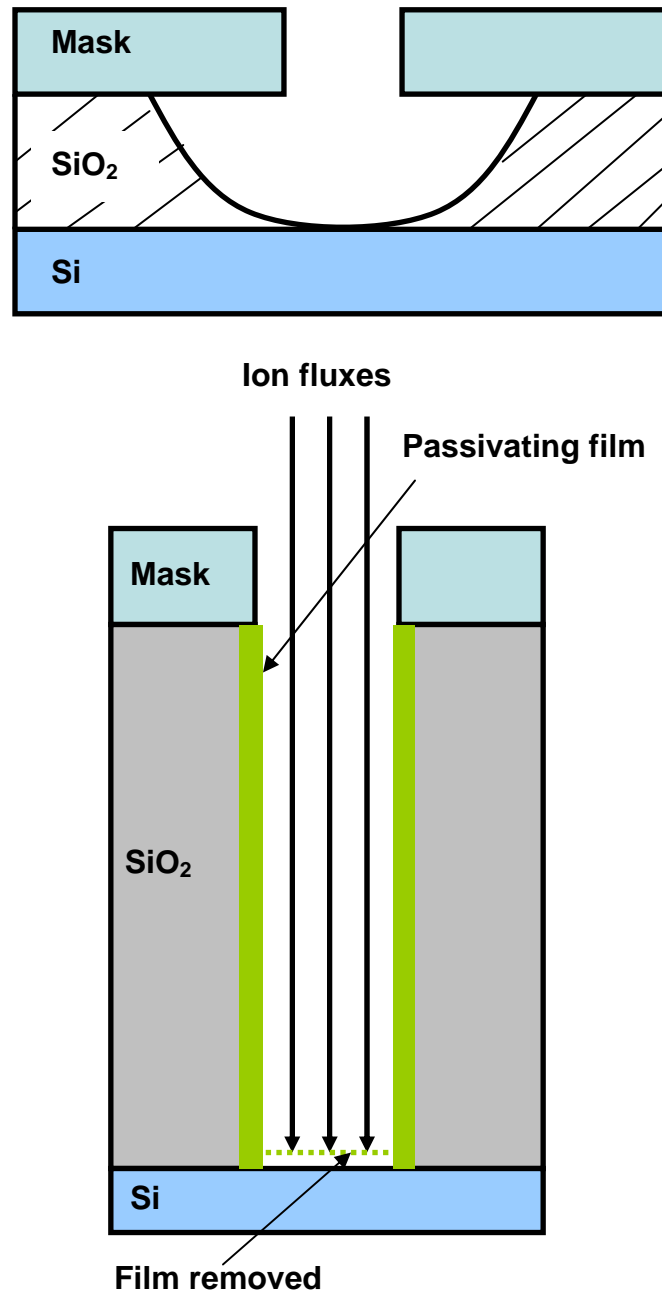
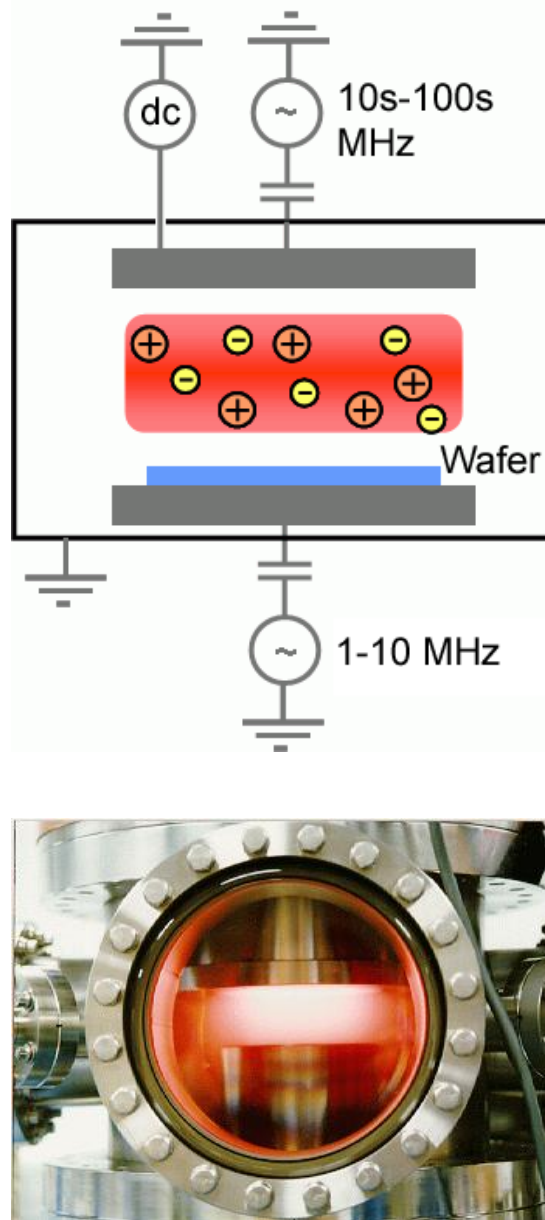
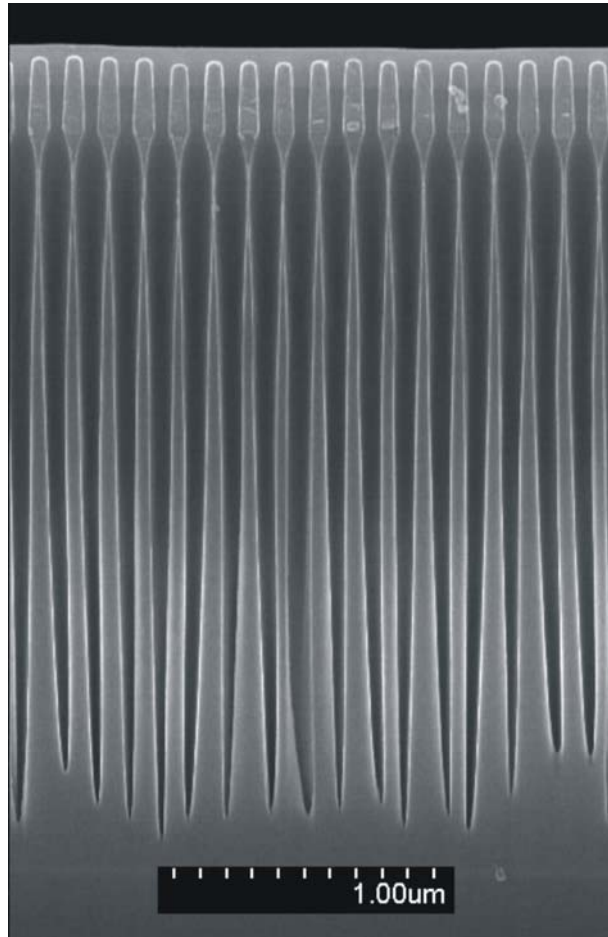


Fig. 1.2 (Top) Isotropic etching profile; (Bottom) Anisotropic etching profile.



**Fig. 1.3 (Top) Schematic of a CCP reactor powered by two rf frequencies and an optional dc bias; (Bottom) Image of a laboratory rf plasma (ref: L. Overzet, U of Texas at Dallas)**



**Fig. 1.4 SEM image of HAR trench array\* . (\*Micron Inc.)**

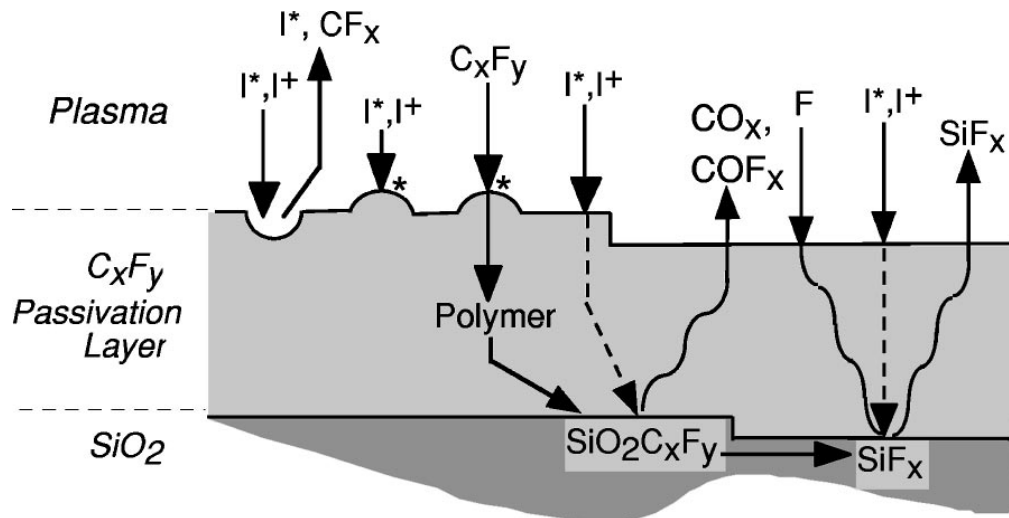


**Fig. 1.5** Schematic of surface reaction mechanism for fluorocarbon etching of  $\text{SiO}_2/\text{Si}$  [58].

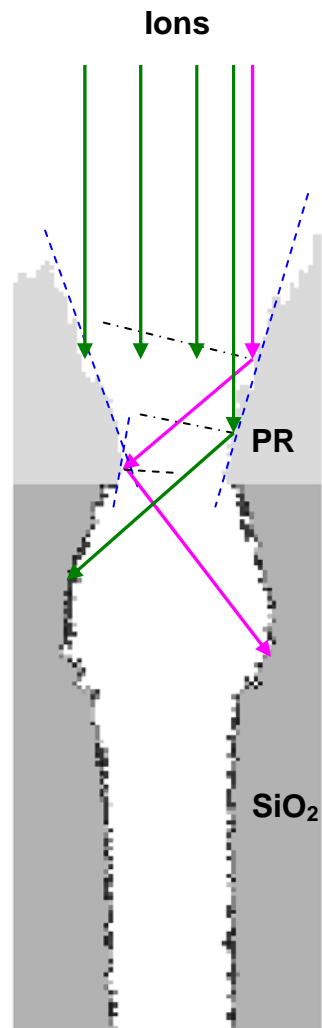


**Fig. 1.6 Schematic of bowing mechanism in HAR etching.**

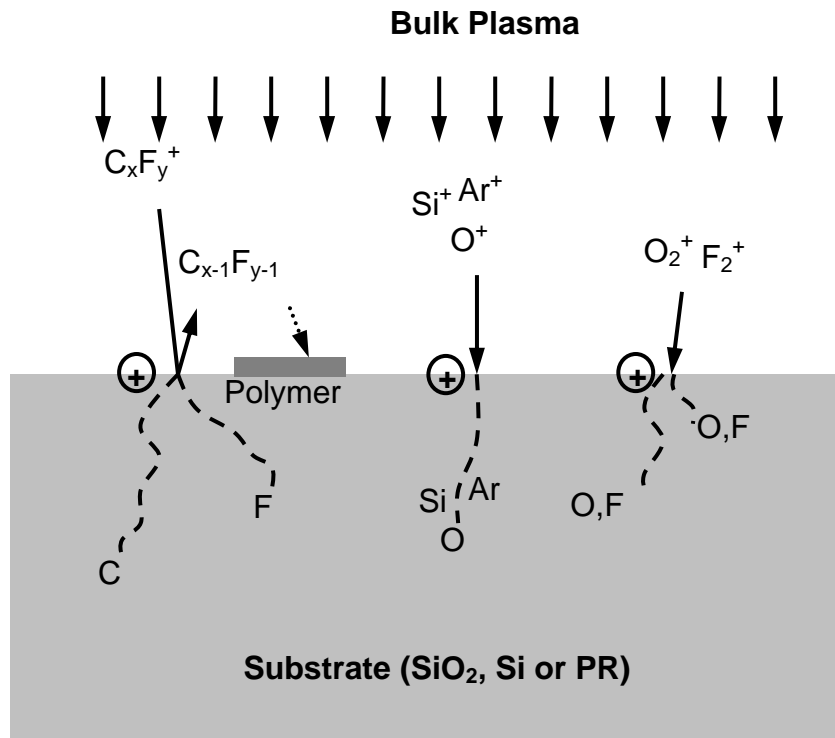


**Fig. 1.7 Schematic of surface dissociation reactions and implantation mechanisms.**

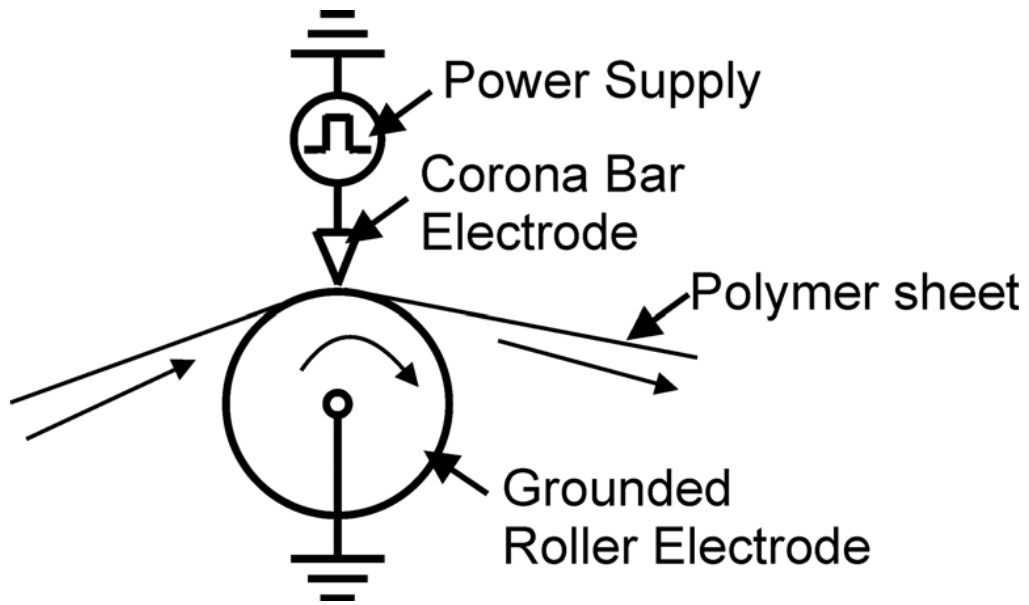


**Fig. 1.8** Schematic of the web treatment arrangement used for the continuous plasma treatment of polymer sheets.

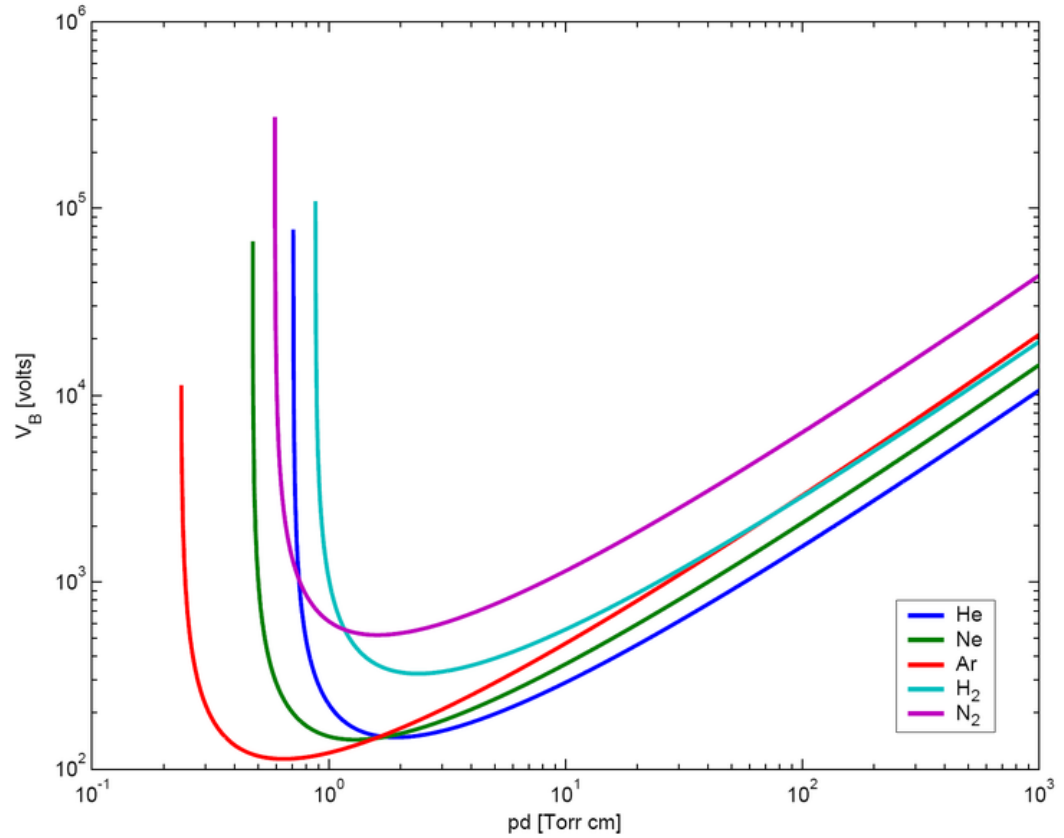


**Fig. 1.9** Paschen curves obtained for Helium, Neon, Argon, Hydrogen and Nitrogen, using the expression for the breakdown voltage as a function of the parameters A,B that interpolate the first Townsend coefficient.

[http://commons.wikimedia.org/wiki/File:Paschen\\_Curves.PNG](http://commons.wikimedia.org/wiki/File:Paschen_Curves.PNG)

## 1.8 References

1. C. Y. Chang and S. M. Sze, ULSI Technology (McGraw-Hill, 1996).
2. J. W. Coburn and H. F. Winters, *Annu. Rev. Mater. Sci.* **13**, 91 (1983).
3. I.W. Rangelow, *J. Vac. Sci. Technol. A* **21**, 1550 (2003).
4. R.J. Hoekstra and M.J. Kushner, *J. Vac. Sci. Technol. B* **16**, 2102 (1998).
5. G.S. Hwang and K.P. Giapis, *J. Vac. Sci. Technol. B* **15**, 70 (1996).
6. K.P. Giapis, G.S. Hwang, *Thin Solid Films* **374**, 175 (2000).
7. W.Z. Collison and M.J. Kushner, *Appl. Phys. Lett.* **68**, 903 (1995).
8. T. Shimada, T. Yagisawa and T. Makabe, *Jpn. J. Appl. Phys.* **45**, L132 (2006).
9. H. Ohtake, B. Jinnai, Y. Suzuki, et al. *J. Vac. Sci. Technol. A* **24**, 2172 (2006).
10. M. Schaepkens, R.C.M. Bosch, T.E.F.M. Standaert, et al. *J. Vac. Sci. Technol. A* **26**, 2099 (1998).
11. P. Subramonium and M.J. Kushner, *J. Appl. Phys.* **96**, 82 (2004).
12. A. Agarwal and M.J. Kushner, *J. Vac. Sci. Technol. A* **23**, 1440 (2005).
13. N.R. Rueger, M.F. Doemling, M. Schaepkens, et al. *J. Vac. Sci. Technol. A* **17**, 2492 (1999).
14. Y. Hoshino, T. Ozake and S. Samukawa, *J. Vac. Sci. Technol. B* **23**, 2063 (2005).

15. S. Noda, T. Ozaki and S. Samukawa, *J. Vac. Sci. Technol. A* **24**, 1414 (2006).
16. K. Endo, S. Noda, M. Masahara, et al. *IEEE T. Electron Dev.* **53**, 1826 (2006).
17. A. V. Vasenkov, X. Li, G.S. Oehrlein, et al. *J. Vac. Sci. Technol. A* **22**, 511 (2004).
18. Y. Morikawa, T. Koidesawa, T. Hayashi, et al. *Thin Solid Films* **515**, 4918 (2006).
19. M. Schaepkens, G.S. Oehrlein and J.M. Cook, *J. Vac. Sci. Technol. B* **18**, 848 (2000).
20. M. Schaepkens, G.S. Oehrlein and J.M. Cook, *J. Vac. Sci. Technol. B* **18**, 856 (2000).
21. G. DiPeso, V. Vahedi, D. W. Hewett, and T. D. Rognlien, *J. Vac. Sci. Technol. A* **12**, 1387 (1994).
22. J. H. Tsai and C. Wu, *Phys. Rev. A* **41**, 5626 (1990).
23. L. C. Pitchford, P. Belenguer, and J. P. Boeuf, *Microwave Discharges: Fundamentals and Applications*, 359 (1993).
24. M. Dalvie, M. Surendra, and G. S. Selwyn, *Appl. Phys. Lett.* **62**, 3207 (1993).
25. D. P. Lymberopoulos and D. J. Economou, *J. Appl. Phys.* **73**, 3668 (1993).
26. J. P. D. Passchier and W. J. Goedheer, *J. Appl. Phys.* **74**, 3744 (1993).
27. W. J. Goedheer, P. M. Meijer, J. Bezemer, J. D. P. Passchier, and W. G. J. H. M. van Sark, *IEEE T. Plasma Sci.* **23**, 644 (1995).

28. P. L. G. Ventzek, R. J. Hoekstra, T. J. Sommerer, and M. J. Kushner, *Appl. Phys. Lett.* **63**, 605 (1993).
29. P. L. G. Ventzek, R. J. Hoekstra, T. J. Sommerer, and M. J. Kushner, *J. Vac. Sci. Technol. B* **12**, 461 (1994).
30. U. Kortshagen, I. Pukropski, and L. D. Tsendin, *Phys. Rev. E* **51**, 6063 (1995).
31. D. J. Economou, T. J. Bartel, R. S. Wise, and D. P. Lymberopoulos, *IEEE T. Plasma Sci.* **23**, 581 (1995).
32. T. Panagopoulos, D. Kim, V. Midha, and D. Economou, *J. Appl. Phys.* **91**, 2687 (2002).
33. J. I. Ulacia F. and J. P. McVittie, *J. Appl. Phys.* **65**, 1484 (1989).
34. T. S. Cale, G. B. Raupp, and T. H. Gandy, *J. Appl. Phys.* **68**, 3645 (1990).
35. P. W. May, D. F. Klemperer, and D. Field, *J. Appl. Phys.* **73**, 1634 (1993).
36. G. S. Hwang and K. P. Giapis, *J. Appl. Phys.* **81**, 3433 (1997).
37. G. S. Hwang and K. P. Giapis, *J. Appl. Phys.* **82**, 572 (1997).
38. G. S. Hwang and K. P. Giapis, *Phys. Rev. Lett.* **79**, 845 (1997).
39. G. S. Hwang and K. P. Giapis, *Appl. Phys. Lett.* **71**, 29282930 (1997).
40. J. P. Chang, A. P. Mahorowala, and H. H. Sawin, *J. Vac. Sci. Technol. A* **16**, 217 (1998).

41. A. P. Mahorowala, H. Sawin, R. Jones, and A. H. Labun, *J. Vac. Sci. Technol. B* **20**, 1055 (2002).
42. A. P. Mahorowala and H. Sawin, *J. Vac. Sci. Technol. B* **20**, 1084 (2002).
43. R. J. Hoekstra, M. J. Grapperhaus, and M. J. Kushner, *J. Vac. Sci. Technol. A* **15**, 1913 (1997).
44. D. B. Graves and D. Humbird, *Appl. Sur. Sci.* **192**, 72 (2002).
45. D. Humbird, D. B. Graves, A. A. E. Stevens and W. M. M. Kessels, *J. Vac. Sci. Technol. A* **25**, 1529 (2007).
46. T. Ohchi, S. Kobayashi, M. Fukasawa, K. Kugimiya, T. Kinoshita, T. Takizawa, S. Hamaguchi, Y. Kamide, and T. Tatsumi, *Jap. J. Appl. Phys.* **47**, 5324 (2008).
47. A. Matsuda, Y. Nakakubo, Y. Takao, K. Eriguchi, K. Ono, *Thin Solid Films* **518**, 3481 (2010).
48. S. -B. Wang and A. E. Wendt, *J. Appl. Phys.* **88**, 643 (2000).
49. T. Novikova, B. Kalache, P. Bulkin, et al. *J. Appl. Phys.* **93**, 3198 (2003).
50. T. Kitajima, Y. Takeo, Z. Lj. Petrovic, et al. *Appl. Phys. Lett.* **77**, 489 (2000).
51. E. Kawamura, M. A. Lieberman, A. J. Lichtenberg, et al. *J. Vac. Sci. Technol. A* **25**, 1456 (2007).

52. E. Kawamura, A. J. Lichtenberg, and M. A. Lieberman, *Plasma Sources Sci. Technol.* **17**, 045002 (2008).
53. K. Denpoh and P. L. G. Ventzek, *J. Vac. Sci. Technol. A* **26**, 1415 (2008).
54. L. Xu, L. Chen, M. Funk, et al. *Appl. Phys. Lett.* **93**, 261502 (2008).
55. S. Welch, K. Keswick, P. Stout, et al. *Semicond. Int.* **32**, 18 (2009).
56. N. Ikegami, A. Yabata, T. Matsui, et al. *Jpn. J. Appl. Phys., Part I* **36**, 2470 (1997).
57. D. Kim and E. A. Hudson, *Thin Solid Films* **515**, 4874 (2007).
58. A. Sankaran and M. J. Kushner, *Appl. Phys. Lett.* **82**, 1824 (2003).
59. J. -K. Lee, H. -Y. Jang, S. -H. Lee, et al. *J. Electrochem. Society* **157**, D142 (2010).
60. T. Yagi, A. E. Pavlath and A. G. Pittman, *J. Appl. Polym. Sci.* **27**, 4019 (1982).
61. J. P. Manion and D. J. Davies, U.S. Patent No. 3674667 (1982).
62. M. Strobel, S. Corn, C. S. Lyons and G. A. Korba, *J. Polym. Sci. A: Polym. Chem.* **25**, 1295 (1987).
63. N. Inagaki, S. Tasaka and M. Imai, *J. Appl. Polym. Sci.* **48**, 1963 (1993).
64. B. Bae, B. H. Chun and D. Kim, *Polymer* **42**, 7879 (2001).
65. A. N. Bhoj and M. J. Kushner, *J. Phys. D: Appl. Phys.* **39**, 1594 (2006).

66. C. Lopez-Santos, F. Yubero, J. Cotrino, et al. *J. Phys. D: Appl. Phys.* **41**, 225209 (2008).
67. U. Kogelschatz, *Plasma Chemistry and Plasma Processing* **23**, 1 (2003).
68. H.-E. Wagner, R. Brandenburg, K.V. Kozlov, A. Sonnenfeld, P. Michel and J.F. Behnk, *Vacuum* **71**, 417, (2003).
69. F. Massines and G. Gouda, *J. Phys. D: Appl. Phys.* **31**, 3411 (1998).
70. U. Kogelschatz, *IEEE T. Plasma. Sci.* **30**, 1400 (2002).
71. J. Rahel and D. M. Sherman, *J. Phys. D: Appl. Phys.* **38**, 547 (2005).
72. G. Borgia, C. A. Anderson, N. M. D. Brown, *Appl. Surf. Sci.* **221**, 203 (2004).
73. J. B. Lynch, P. D. Spence, D. E. Baker and T. A. Postlethwaite, *J. Appl. Polym. Sci.* **71**, 319 (1999).
74. Yu. S. Akishev, M. E. Grushin, A. E. Monich, A. P. Napartovich, and N. I. Trushkin, *High Energ. Chem+* **37**, 286 (2003).
75. S. De, R. Sharma, N. Ali, and M. K. Mazumder, *IEEE IAS*, **39**, 932 (2004).
76. S. Guimond, I. Radu, G. Czeremuskin, D. J. Carlsson, and M. R. Wertheimer, *Plasmas and Polymers* **7**, 71 (2002)
77. G. Borgia, C. A. Anderson and N. M. D. Brown, *Plasma Sources Sci. T.* **14**, 259 (2005).

78. M. Sira, D. Trunec, P. Stahel, V. Bursikova, Z. Navratil and J. Bursik., *J. Phys. D: Appl. Phys.* **38**, 621 (2005)
79. N. Sellin and J. S-C. Campos, *Mater. Res.* **6**, 163 (2003).
80. G. Borgia, N. M. D. Brown, D. Dixon and R. McIlhagger, *Surf. Coat. Tech.* **179**, 70 (2004).
81. J. Comyn, L. Mascia, G. Xiao and B.M. Parker, *Int. J. Adhesion and Adhesives* **16**, 301 (1996) .
82. G. Borgia, N. Dumitrascu and G. Popa, *Surf. Coat. Tech.* **197**, 316 (2005).
83. U. Schulz, P. Munzert and N. Kaiser, *Surf. Coat. Tech.* **142-144**, 507 (2001).
84. K. Schroder, G. Babucke and A. Ohl, *Surf. Interface Anal.* **36**, 702 (2004).
85. L-A. O'Hare, J. A. Smith, S. R. Leadley, B. Parbhoo, A. J. Goodwin and J. F. Watts, *Surf. Interface Anal.* **33**, 617 (2002).
86. S. Ishikawa, K. Yukimura, K. Matsunaga and T. Maruyama, *Surf. Coat. Tech.* **130**, 52, (2000).
87. N. Dumitrascu, G. Borgia and G. Popa, *J. Appl. Polym. Sci.* **81**, 2419 (2001).
88. S. Brandt, R. A. Goffe, S. B. Kessler, J. L. O'Connor, S. E. Zale, *Bio-technology* **6**, 779 (1988).

## 2. DESCRIPTION OF THE MODEL

### 2.1 Hybrid Plasma Equipment Model (HPEM)

#### 2.1.1 Introduction

The Hybrid Plasma Equipment Model (HPEM) is a 2-dimensional model that consists of separate modules that address different physical phenomena. This model has been developed for simulating low-temperature, low-pressure plasma processes such as plasma etching and plasma-assisted deposition [1–17]. Each module in HPEM consists of a time integration over many rf cycles, during which plasma quantities (e.g., densities, temperatures) are either recorded as a function of position and phase or recorded only as position-dependent quantities averaged over the rf cycle. These values are then passed to the next module and the process iterated to a cycle-average steady state. The modules used in this study are: the 1) Electron Monte Carlo Simulation (EMCS) for sheath accelerated secondary electrons, 2) the Fluid Kinetics Module (FKM) to obtain densities, fluxes, and energies of all charged and neutral species, as well as the electric potential from the solution of Poisson’s equation and 3) the Plasma Chemistry Monte Carlo Module (PCMCM) to obtain the energy and angular distributions of neutrals and charged species striking the wafer.

#### 2.1.2 The Fluid Kinetics Module (FKM)

In the FKM, continuity, momentum, and energy equations are separately solved for all non-electron species (neutrals and ions). Coupling between these fluids is through collisional exchange for momentum and energy. For bulk electrons, only continuity and

energy equations are solved where fluxes are provided by the Sharfetter-Gummel formulation [18]. The equations solved include the following:

The continuity equation for all species is

$$\frac{\partial N_i}{\partial t} = -\nabla \cdot \Gamma_i + S_i \quad (2.1)$$

which can be used to solve for the species densities where  $N_i$ ,  $\Gamma_i$ , and  $S_i$  are the respective density, flux, and sources for species  $i$ .

The electron flux  $\Gamma_i$  is determined by the drift diffusion equation

$$\Gamma_i = \mu_i q_i N_i \bar{E}_s - D_i \nabla N_i \quad (2.2)$$

where  $\mu_i$  is the mobility of species  $i$ ,  $D_i$  is the diffusion coefficient,  $q_i$  is the species charge in units of elementary charge, and  $\bar{E}_s$  is the electrostatic field. Combining upwind and downwind techniques, the flux  $\vec{\varphi}_{i+\frac{1}{2}}$  between density mesh points ( $i, i+1$ ) separated by  $\Delta x$  is given by

$$\vec{\varphi}_{i+\frac{1}{2}} = \frac{\alpha \bar{D}(n_{i+1} - n_i \exp(\alpha \Delta x))}{(1 - \exp(\alpha \Delta x))} \quad (2.3)$$

where

$$\alpha = -q \bar{\mu} \left( \frac{\bar{\Phi}_{i+1} - \bar{\Phi}_i}{\Delta x} \right)$$

and  $\bar{D}$  and  $\bar{\mu}$  are the average diffusion coefficient and mobility in the interval. The ion and neutral flux calculation can be done using the drift diffusion equation or by including the effects of momentum by the replacement of the diffusional term with terms for pressure, advection, and collision

$$\begin{aligned} \frac{\partial \Gamma_i}{\partial t} = & -\frac{1}{m_i} \nabla(N_i k T_i) - \nabla \cdot (N_i \bar{v}_i \bar{v}_i) + \frac{q_i}{m_i} N_i (\bar{E}_s + \bar{v}_i \times \bar{B}) \\ & - \nabla \cdot \bar{v}_i - \sum_j \frac{m_j}{m_i + m_j} N_i N_j (\bar{v}_i - \bar{v}_j) \nu_{ij} \end{aligned} \quad (2.4)$$

where  $T_i$  is the species temperature,  $\bar{v}_i$  is the species velocity given by  $\Gamma_i / N_i$ , and  $\nu_{ij}$  is the collision frequency between species  $i$  and species  $j$ . The viscosity is included for neutrals only. Determination of the time-dependent electrostatic fields is accomplished either by solution of Poisson's equation or based on quasi-neutrality allowing an ambipolar approximation. Poisson's equation using a predictor corrector technique for charge is given by

$$\nabla \cdot ((\epsilon - \Delta t \sigma + \Delta t \sum_i q_i^2 \mu_i N_i^2) \nabla \phi^{t+\Delta t}) = -\rho^t + \Delta t \nabla \cdot (\sum_i q_i D_i \nabla N_i^t - \sum_j q_j \Gamma_j^t) \quad (2.5)$$

where  $\sigma$  is the material conductivity and is nonzero only outside of the plasma region and  $e$  is elemental charge;  $q_i$ ,  $\mu_i$ ,  $N_i$ , and  $\Gamma_i$  are the charge state, mobility, density, and flux of species  $i$  at time  $t$ , respectively;  $\Gamma_j$  is the flux for species  $j$  at time  $t$ ; and  $\phi^{t+\Delta t}$  is the electric potential at time  $t + \Delta t$ . Poisson's equation is calculated semi-implicitly by approximating the charge density linearly as

$$\rho^{t+\Delta t} = \rho^t + \Delta t \cdot \left. \frac{\partial \rho}{\partial t} \right|^{t+\Delta t} \quad (2.6)$$

where  $\rho^{t+\Delta t}$  is the charge density at time  $t+\Delta t$ , and  $\rho^t$  is the charge density at time  $t$ . The evolution rate of the charge density  $\partial \rho / \partial t$  is determined by the divergence of the total current density  $j$ :

$$\frac{\partial \rho}{\partial t} = -\nabla \cdot j + S \quad (2.7)$$

where  $S$  is the source function of charges. In the plasma region,  $j = q_i(-D_i \nabla n_i + q_i \mu_i (-\nabla \phi))$  for electrons and  $j = qI$  for ions. In materials,  $j = \sigma(-\nabla \phi)$  where  $\sigma$  is the material conductivity. By making the potential fully implicit in this scheme while using explicit terms for the assumedly more slowly varying species properties such as density and temperature, the time step used in the Successive-over-Relaxation (SOR) solution can be lengthened beyond the dielectric relaxation time and greatly accelerate solution over the fully explicit formulation.

For bulk electrons, transport coefficients are provided as a function of electron temperature by solving Boltzmann's equation. These values are updated every iteration using heavy particle mole fractions, including excited states, averaged over the reactor weighted by the local electron density.

Acceleration techniques are used to speed the rate convergence of computed quantities. During execution of the FKM, the cycle averaged time rate of change of densities is recorded over a period of many rf cycles. The integration is then paused and the

densities of species are increased (or decreased) proportional to these average rates and the integration restarted. As different rates of acceleration are applied to different species depending on their derivatives, it is difficult to assign a precise time interval for which the densities are projected into the future. For example, a well converged case will consist of approximately 100-200 iterations through the modules with 0.5-1  $\mu$ s of actual integration time (5-10 cycles at 10 MHz) occurring in the FKM (or up to 2,000 cycles). For 10 cycles of actual time integration, acceleration will typically be applied after 2-3 cycles of the first 6 cycles, with no acceleration for the last cycles of the iteration. Based on convergence rates, this is effectively the equivalent of 50-100 times as many cycles. Since different species are accelerated at different rates, it is possible that the net charge density is not conserved through the acceleration process. To prevent unphysical transients in plasma potential and charging of surfaces, the charge density in each cell in the volume and on surfaces is recorded before acceleration. After the acceleration, the electron density is adjusted so that the charge density in each cell is the same as before the acceleration.

### 2.1.3 The Electron Monte Carlo Simulation (EMCS)

The transport of secondary electrons emitted from surfaces is tracked using the EMCS [19]. The electric field as a function of position and phase produced in the FKM is recorded, and these values are interpolated for position and phase during execution of the EMCS. The fluxes and energies of ions striking surfaces are recorded as a function of position which, convolved with the secondary electron emission coefficient, provides the flux of secondary electrons as a function of position along the surface. The secondary electrons are emitted with a Lambertian distribution (essentially a cosine with angle

measured in respect to the vertical) and an energy of 4 eV. Each pseudoparticle carries a weighting of number of particles-per-second, or a current. A total of 25,000 electron pseudoparticles are released in the EMCS for each iteration through the HPEM.

The trajectories of the secondary electrons are tracked by integrating their equations of motion while accounting for collisions using Monte Carlo techniques.

The electron energy range is divided into discretized energy bins for collision determination. The collision frequency,  $\nu_i$ , within any energy bin is computed by summing all possible collisions within the energy range

$$\nu_i = \left(\frac{2\varepsilon_i}{m_e}\right)^{\frac{1}{2}} \sum_{j,k} \sigma_{ijk} N_j \quad (2.8)$$

where  $\varepsilon_i$  is the average energy within the bin,  $\sigma_{ijk}$  is the cross section at energy  $i$ , for species  $j$  and collision process  $k$ , and  $N_j$  is the number density of species  $j$ . The time between the collisions is randomly determined using the maximum collision frequency for all energy bins.  $\Delta t = -\frac{1}{\nu} \ln(r)$ ,  $r = (0,1)$ . The pseudoparticles are tracked until they are collected by a surface, attach, recombine, or fall below an energy corresponding to the minimum electron excitation threshold,  $\varepsilon_T$ . Particle trajectories are integrated using the Lorentz equation

$$\frac{d\bar{\mathbf{v}}}{dt} = \frac{q_e}{m_e} (\bar{\mathbf{E}} + \bar{\mathbf{v}} \times \bar{\mathbf{B}}) \quad (2.9)$$

where  $\bar{v}$ ,  $\bar{E}$ , and  $\bar{B}$  are the electron velocity, local electric field, and magnetic field respectively.

If an ionization produces a secondary electron having an energy above  $\varepsilon_T$ , its trajectory will also be integrated. When removing an electron, its trajectory is checked to make certain it is not at a turn-around point occurring, for example, in a sheath. The electron current striking surfaces is recorded as a function of position. This current is then used in the FKM to either charge dielectric surfaces (which then appears as displacement current) or to contribute to conduction current if the surface is a metal or has a finite conductivity. The current of electrons falling below  $\varepsilon_T$  is also recorded as a function of position and used as a source of negative charge in the electron continuity equation in the FKM.

As the pseudoparticle is moved, its energy is recorded on the numerical mesh weighted by the time required to traverse that cell. The resulting electron energy distributions have real units of current/volume. These distributions are convolved with inelastic cross sections to provide source functions for ionization and excitation which are then used in the continuity equations in the FKM.

#### 2.1.4 Plasma Chemistry Monte Carlo Module (PCMCM)

To obtain the energy and angular distributions of reactive species to the substrate, the PCMCM was developed for the HPEM. The PCMCM calculates the trajectories of plasma species in the gas phase and their collisions with surfaces. This module was originally a postprocessor to the HPEM. It used volumetric sources of plasma species, time-dependent electric fields, and sheath properties exported from the HPEM to obtain the

angular and energy distributions of the fluxes using Monte Carlo techniques. The PCMCM functions in a similar manner but also accounts for nonthermal, or in-flight fluxes, resulting from sputter sources in addition to the volumetric sources. Sputtered atoms and neutralized ions which are reflected from the target have kinetic energies of several eV. These species are not initially in thermal equilibrium with the buffer gas, which has a temperature of  $\leq 0.3$  eV. Under certain process conditions, these energetic particles may not thermalize prior to reaching the wafer. The trajectories and energies of these nonequilibrium particles are already tracked by the sputter algorithms in the FKM. Statistics on the energy and angular distributions of the particles as they strike selected surfaces are collected and passed to the PCMCM.

Based on these quantities, a rate of generation of species  $i$  as a function of position,  $G_i(\vec{r})$  ( $\text{cm}^{-3}\text{s}^{-1}$ ), is computed. This generation term accounts for all sources of species  $i$  on the right-hand side of reactions in the mechanism. The rate  $G_i(\vec{r})$  also includes source functions on surfaces due to, for example, sputtering. In a similar fashion, a consumption rate  $C_i(\vec{r})$  ( $\text{cm}^{-3}\text{s}^{-1}$ ) is computed based on all reactions containing species  $i$  on the left-hand side of reactions in the mechanism. A local elastic collision frequency with each species is also computed. These elastic frequencies are added to the local consumption frequency  $C_i(\vec{r})\Delta V(\vec{r})$ , where  $\Delta V(\vec{r})$  is the volume of the computational cell at location  $\vec{r}$  to yield a total interaction frequency  $\nu_T(\vec{r})$ . Null collision techniques are used at each spatial location to provide a reactor wide collision frequency  $\nu_i$  for each species  $i$ .

Pseudoparticles of species  $i$  are launched from each computational cell at a time

randomly chosen in the rf cycle with a weighting (or total number) proportional to

$C_i(\vec{r})\Delta V(\vec{r})$ . The velocity is randomly chosen from a Maxwell-Boltzmann distribution having a local temperature  $T_i(\vec{r})$  for volumetric sources where the spatially dependent temperature for each species is computed by HPEM. The trajectories of the pseudoparticles are integrated for the time

$$\Delta t = -\frac{1}{v_i} \ln(r) \quad (2.10)$$

where  $\Delta t$  is the time step for movement of the pseudoparticle and  $r$  is a random number distributed on  $(0,1)$ . For ions, acceleration by the local electric field is accounted for. The time step used to increment the trajectory is limited by the time required to cross a specified fraction of the cell (typically 0.2). For ions, additional constraints are applied including a specified fraction of the rf cycle (typically 0.05), or the time to cross a specified fraction of the sheath width (typically 0.01).

At the end of the time step, Monte Carlo techniques are used to determine if the collision is real or null. If real, another random number is used to determine if the collision is elastic or consuming. If consuming, the particle is removed from the simulation. If elastic, the collision partner is identified using another random number and the velocity of the pseudoparticle is changed appropriately using standard elastic collision techniques. The one exception is for charge exchange collisions which are separately accounted for in the sum of collision frequencies. If an ion undergoes a charge exchange collision, its identity is changed to the neutral counterpart and the trajectory is retained. The trajec-

ries are advanced until the pseudoparticles reach the vicinity of a surface. If the surface is chosen as one for which statistics on incident species are desired, ions are then integrated through the sheath, a computationally expensive process. For surfaces not selected, the particles are removed from the simulation. A similar process is followed for the neutrals, except for integration through the sheath.

## 2.2 Monte Carlo Feature Profile Model (MCFPM)

The fluxes of reactant species and their energy angular distributions (EADs) from the PCMCM are then used as input to the Monte Carlo Feature Profile Model (MCFPM) [21–23]. The MCFPM resolves the surface (e.g., PR, polymer, semiconductor) of the wafer using a two-dimensional rectilinear mesh. Poisson's equation is solved to obtain charge-induced potentials and electric fields in and around the feature. Charges from incident electrons and ions are accumulated and summed on the mesh. The charge may subsequently move, as explained below. If a mesh cell with charge is removed by virtue of neutral chemical reactions, its charge is retained in the mesh by redistributing it to the adjacent mesh cells. A simple flow of computational models and their functions is shown in Fig. 2.1.

In the MCFPM, pseudoparticles representing ions and neutral species are launched towards the surface with a frequency, energy, and angle randomly chosen from the EADs produced by the PCMCM. Each particle carries a weighting of atoms/second, or current. The number of atoms per pseudoparticle is equal to the number atoms in a solid mesh cell. However, this choice only affects resolution in the absence of charging, when including charging the results are sensitive to the size of the cell. (See discussion

below.) Each gas phase particle is tracked until it is either incorporated into the solid mesh or leaves the computational domain. The trajectories of gas phase particles produced by the interaction of fluxes with the surface (e.g., an etch product) are then also followed until that particle is incorporated into the solid mesh or leaves the domain. Since the residence time of a particle in a feature is at best a nanosecond, whereas the time between incident particles having the largest fluxes is many microseconds, the likelihood of finding two incident particles in the feature at the same time is small. As a result, only a single gas phase pseudoparticle is tracked at a time. If more than a single gas phase particle is produced as a result of a surface reaction, the trajectory of the first particle is completed before the trajectories of the second (and subsequent particles) are followed.

We assumed that all ions striking a surface deposit their charge at the site of the collision. The ion then reflects as a hot neutral, diffusively at low energy and progressively more specularly as its energy increases. Electrons striking the surface either deposit their charges or are reflected based on the secondary emission coefficient for electrons by electrons,  $\gamma_{ee}$ . Electrons striking a surface having values of  $\gamma_{ee} < 1$  on the average deposit negative charge. Electrons striking a surface with values of  $\gamma_{ee} > 1$  on the average produce positive charge. The energy and angular dependence of  $\gamma_{ee}$  we used were obtained from Ref. 20. Given the limited materials for which properties were available, we used  $\gamma_{ee}$  values for quartz to represent  $\text{SiO}_2$ , Si, and photoresist, and values of  $\gamma_{ee}$  for Teflon for fluorocarbon polymer. These algorithms were implemented in the following manner: when an electron strikes the surface, its energy and angle of incidence were used to obtain  $\gamma_{ee}$ . A random number  $r$  [distributed (0, 1)] was selected. If  $r > \gamma_{ee}$ , the

electron was collected on the surface. If  $r < \gamma_{ee}$  the electron was reflected.

The EADs of ions and neutral particles, and of HEE fluxes, were obtained from the PCMCM of the HPEM, as discussed in Section 2.1. The fluxes of thermal electrons are not directly obtained from the PCMCM and so these fluxes are computed in the following manner. Since the wafer is capacitively coupled to ground, the net cycle averaged charged particle flux to its surface must sum to zero. The fluxes obtained from the PCMCM for ions and HEEs are separately summed. The net current at this point is positive due to the absence of thermal electrons. The charge neutrality requirement is then achieved by adding a thermal electron flux having Maxwellian energy distribution and a Lambertian angular distribution. The electron temperature is obtained from the HPEM.

Given the charge accumulation on surfaces, Poisson's equation,  $\nabla \cdot \epsilon \nabla \Phi = -\rho$  is solved using the method of Successive-Over-Relaxation (SOR) to provide the electric potential,  $\Phi$ , in and around the feature for permittivity  $\epsilon$  and charge density  $\rho$ . The conductivity,  $\sigma$ , and permittivity of solid materials are specified. Since it is computationally expensive to solve Poisson's equation, the electric fields are not necessarily updated after the trajectory of each charged particle is completed (which may produce charge on the surface of the feature). Instead, Poisson's equation is solved after launching a specified number of charged particles—typically 30 in the cases discussed here. We parameterized this number to insure that computed values of  $\Phi$  were well represented. The boundary conditions were  $\Phi = 0$  at the top and bottom boundaries of the computation domain, and  $d\Phi/dx = 0$  at the left and right boundaries.

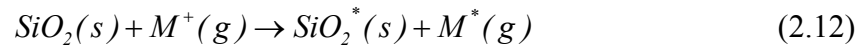
We also included dispersal of the charge in the solid materials due to conduction

currents. The charge density for cell  $j$  used in solution of Poisson's equation was given by

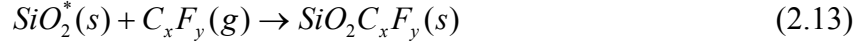
$$\frac{d\rho_j}{dt} = \frac{d}{dt} \left( \sum_i \frac{q_i}{V_j} \right) - (\nabla \cdot \sigma(-\nabla \Phi)) \quad (2.11)$$

where  $q_i$  is the charge of incident particle  $i$ ,  $V_j$  is the volume of cell  $j$ , and  $\sigma$  is the material conductivity. Since the likelihood that two gas phase charged particles will be in the feature at the same time is extremely small, we did not include charge in the gas phase in solution of Poisson's equation. Collected charge remains on surfaces until neutralized by subsequently collected particles or dispersed by conduction through the material. We did not allow that a sputtered material cell would carry away its charge into the gas phase. So when a cell with charge is sputtered, its charge is dispersed to adjoining solid cells. We do, however, allow charge to be buried. That is, if a cell is charged and deposited over by polymer, the charge remains below the surface.

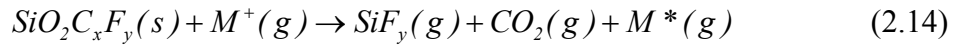
The reaction mechanism for etching of Si and SiO<sub>2</sub> in fluorocarbon plasmas is described in detail in Ref. 21. Briefly, etching of SiO<sub>2</sub> is dominantly through formation of a fluorocarbon complex. SiO<sub>2</sub> sites on the surface are first activated by ion bombardment,



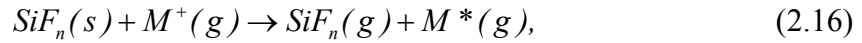
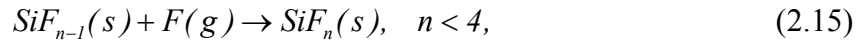
where SiO<sub>2</sub><sup>\*</sup> represents an activated site on surface, M<sup>+</sup> is an ion and M\* is its hot neutral counterpart. Then C<sub>x</sub>F<sub>y</sub> neutrals react with the activated SiO<sub>2</sub> sites to produce a complex layer,



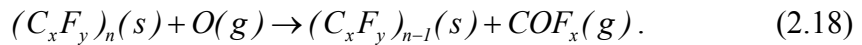
Further deposition by  $C_xF_y$  neutrals produces a thicker polymer layer  $(C_xF_y)_n$ . Energetic ions and hot neutrals penetrate this polymer layer and reach the complex to sputter it, with carbon from the polymer layer providing a means to remove the oxygen in the oxide,



The remaining Si is etching dominantly by F atoms diffusing through the polymer layer, passivating the Si followed by ion activation,



Oxygen radicals produced by electron impact of  $O_2$  are used to control the thickness of the polymer layer during etching.



Sputtering and redeposition of the PR mask were also included using a similar mechanism as polymer removal though at a lower rate. The reaction probabilities for the PR were chosen to provide an etch selectivity of about 10-to-1 with respect to  $SiO_2$ . (That is, the each rate of the PR is 0.1 that of  $SiO_2$ .)

Experimentally, twisting can be rare, occurring in only a few percent or less of all features. Computationally, this presents challenges as many hundreds to thousands of features would need to be simulated in order for a statistically significant number of twisted features to be obtained. The required resolution of the mesh also presents challenges. It is common that the numerical mesh in Monte Carlo simulations be larger than atomic dimensions, typically a few nm. A mesh cell could then represent hundreds of atoms, which would also apply to the gas phase pseudo-particles. When including charging, we found that there was a mesh size dependence to the calculation which was only resolved by having the mesh size (and gas phase pseudo-particles) represent single atoms. Unfortunately, this resulted in total simulation times for hundreds of cases for each process condition, which were unacceptably large. After extensive parameterizations on this dependency, we chose a mesh size of 5 nm and reduced the charge per particle so that computer times were acceptable and the results were essentially the same as when using meshes with atomic dimensions. We also chose values that accentuated the propensity of twisting so that acceptable statistics could be obtained with only tens of cases per process conditions as opposed to hundreds to thousands of cases. We again confirmed that other than increasing the frequency of twisting, other etch properties were well represented compared to using smaller cells and charge.

An IMPLANT model is incorporated into the MCFPM to track the trajectory of implanting particles and simulate mixing after implantation. Although both monoatomic and polyatomic ions are incident onto the surface, for the purposes of the implantation model, we assumed that large polyatomic ions dissociate on impact and monoatomic fragments continue into the surface. In the context of fluorocarbon etching in Ar/C<sub>4</sub>F<sub>8</sub>/O<sub>2</sub>

gas mixtures, the ions we allowed to penetrate into the surface are  $\text{Ar}^+$ ,  $\text{F}^+$ ,  $\text{Si}^+$ ,  $\text{C}^+$  and  $\text{O}^+$ . We included the same algorithms for the hot atom counterparts of these ions. The energy and angle of incidence of the atomic ions (or hot atoms) determine the distance of penetration and deposition of energy into the lattice. The energy deposition along the slowing down path results in dislocations and mixing of the crystal. The slowed ions implant into the lattice, displacing atoms that produce additional mixing. Nonreactive, interstitially implanted ions, such as Ar, then diffuse through the crystal, eventually returning to the plasma.

These algorithms were incorporated into the MCFPM to track the trajectory of implanting particles and to simulate mixing during implantation. The algorithms are schematically shown in Fig. 2.2. And a simple flow chart of the implantation and mixing algorithm is shown in Fig. 2.3. The average stopping range that particles travel in materials (for these simulations, photoresist,  $\text{SiO}_2$ , polymer and Si),  $\bar{\lambda}$ , was estimated using SRIM (Stopping and Ranges of Ions in Matter) as a function of energy [24]. To approximate photoresist (PR), we used PMMA (polymethylmethacrylate) and to approximate fluorocarbon polymer, we used PTFE (polytetrafluorethylene or Teflon). When a particle strikes the wafer surface, a random number  $r = (0, 1)$  is used to determine its theoretical penetration distance into the material.

$$\lambda = -\bar{\lambda} \ln(1-r) \quad (2.19)$$

(Note that for each expression that requires a random number, a different random number generator is used.) Based on the particle's current position, the physical distance that the particle needs to travel along its trajectory through the current mesh cell to reach the next

mesh cell is computed,  $\lambda_a$ . If  $\lambda_a < \lambda$  then the particle is assumed to continue on its trajectory. During its transition along the initial path, the particle loses an amount of energy for initial energy  $\varepsilon_{in}$ ,

$$\Delta\varepsilon = \varepsilon_{in}(1 - \exp(-\lambda_a / \lambda)) \quad (2.20)$$

If,  $\Delta\varepsilon/\varepsilon_{in} > r$ , where  $0 < r < 1$  is a random number, then the amount of energy deposited along the path may produce lattice dislocations. Otherwise, atoms simply oscillate in the same lattice location after absorbing  $\Delta\varepsilon$ . The dislocation depends not only on the energy absorbed but also on steric hindrance. When a lattice dislocation occurs, the identity of adjacent numerical mesh cells is exchanged to denote formation of a dislocation, or a mixing event. If the region of the mesh is totally one material, this exchange will not produce a stoichiometric effect, but will produce a structural effect. If the local environment is heterogeneous (that is, near a boundary between materials), the mixing exchange will blur the boundary.

When the particle enters the next cell, we return to the first step (Equation 2.20) and repeat the process with a reduced particle energy  $\varepsilon_{in} = \varepsilon_{in} - \Delta\varepsilon$ . If  $\lambda_a > \lambda$ , we deem that the particle has stopped and implanted. Before implanting the particle, the adjacent cells are randomly moved to evacuate the implantation site, thereby constituting additional mixing. The cell occupying the implantation site is randomly moved to a neighboring site, freeing up the original site into which the implanted atom is placed. The cell that occupied the site now occupied by the first displaced cell is then moved in a random direction to displace another cell. The successive displacement of cells continues

until a cell is pushed above the material surface to the gas interface or the number of displacement steps exceeds a maximum value based on the incident energy of the ion. The number of steps was determined by  $n = \varepsilon_{in} / 2$  by comparison to experiments.

In our model, energetic ion bombardment of hydrocarbon PR can lead to chain scission of the polymer backbone (degradation) followed by cross-linking (gelling) of adjacent dangling bonds. This cross linking produces a hardened material that is more resistive to sputtering and etching. For example, the hardness of PMMA significantly increases upon high energy ion bombardment due to this scission-cross linking process [25]. The etch rate of PMMA in Ar plasmas initially decreases and then is constant, presumably due to a saturation of the cross linking in the near surface layers [26]. To account for these processes, we included bond-breaking in the PR and conversion to cross-linked sites. The sputtering yield of the cross-linked PR sites is five times smaller than that of normal sites.

Penetration of VUV photon is also included in IMPLANT using a simpler algorithm. Relaxation of excited  $\text{Ar}^*$  produces optical emission lines at around 105 nm. These VUV photons have energy of 11.8 eV, which is higher than binding energies for all chemical bonds (such as C-H, C=O, C-F etc.) and is able to break these bonds and produce polymer chain degradation or molecule dissociation. An  $h\nu_{\text{Ar}^*}$  species representing the VUV photon is included in the chemistry. The absorbing depth for VUV photons is calculated by

$$\lambda = \lambda_{\text{max}} \times \gamma \quad (2.21)$$

where  $\lambda_{\max} = 100$  nm is the maximum penetration depth for VUV photons into the PR (PMMA) [27],  $\gamma$  is a random number, which is used to get a statistical absorption depth due to collisions. VUV photons do not generate mixing since they do not have a visible volume. Absorption of VUV does, however, change the identity of current cell and it may induce dissociation or cross-linking in  $C_xF_y$  polymer and PR.

### 2.3 nonPDPSIM

nonPDPSIM is a multi-fluid 2-D hydrodynamics model in which transport equations for all charged and neutral species, and Poisson's equation, are integrated as a function of time. nonPDPSIM was developed to simulate relatively high pressure (100s mTorr  $\sim$  several atmosphere) plasma properties [28–31]. The numerical grid uses a boundary-fitting, unstructured mesh with triangular elements (Skymesh2 was used in this study to generate the mesh but any but any mesh generator could be used). The geometry can be Cartesian or cylindrically symmetric. Once the unstructured mesh is created, it is kept static for the complete duration of a simulation. The mesh generation has some simple refinement capabilities whereby certain regions in the geometry may be more refined than others. This enables finer resolution of features where necessary and saves computational time by having coarser resolution in other regions.

Electrostatic and electromagnetic fields, the multi-fluid charged species transport, electron energy transport, and gas phase reaction kinetics are solved in a plasma dynamics module. The fundamental equations for the electric potential computed throughout the computational domain, transport of charged species and neutrals computed in the plasma domain, and surface charge computed only on dielectric materials are:

$$-\nabla \cdot \epsilon \nabla \Phi - \sum_j n_j q_j + \rho_s = 0 \quad (2.22)$$

$$\frac{\partial N_i}{\partial t} - (-\vec{\nabla} \cdot \vec{\phi}_i + S_i) = 0 \quad (2.23)$$

$$\frac{\partial \rho_s}{\partial t} - \left( \sum_i -\nabla \cdot (q_i \vec{\phi}_i (1 + \gamma_i)) - \nabla \cdot (\sigma (-\nabla \Phi)) \right) = 0 \quad (2.24)$$

where  $\epsilon$ ,  $\Phi$ ,  $\rho$ ,  $N$ ,  $D$ ,  $\mu$ ,  $\phi$ ,  $\gamma$ ,  $\sigma$ ,  $S$ , and  $q$  refer to the permittivity, electric potential, charge density, species number density, diffusion coefficient, mobility, species flux, secondary emission coefficient, conductivity of solid materials, source terms, and elementary charge respectively. The subscript denotes the identity of the species. Poisson's equation (Equation 2.22) describes the electric potential, transport equations (Equation 2.23) describes conservation for the charged species, and surface charge balance (Equation 2.24), are solved as a simultaneous set of equations. To numerically discretize these equations, finite volume techniques are used.

Photon transport and photoionization algorithm are described in detail in [32]. Photon transport in the plasma is accounted for using a propagator method. The photoionization source for species  $m$  at location  $\vec{r}_i$  due to the emission of photons at location  $\vec{r}_j$  by species  $k$  is

$$S_m(\vec{r}_i) = \sigma_{km}^I N_m(\vec{r}_i) A_k \int N_k(\vec{r}_j) G_k(\vec{r}_j, \vec{r}_i) d^3 \vec{r}_j \quad (2.25)$$

$$G_k(\vec{r}_j, \vec{r}_i) = \frac{\exp\left(-\int_{\vec{r}_j}^{\vec{r}_i} \sum_l \sigma_{lk} N_l(\vec{r}'_n) d\vec{r}'_n\right)}{4\pi |\vec{r}'_i - \vec{r}_j|^2} \quad (2.26)$$

where  $N_k$  is the density of the radiating species having Einstein coefficient  $A_k$ ,  $\sigma_{km}^l$  is the photoionization cross section for species  $m$  by photons emitted by species  $k$  and  $\sigma_{lk}$  is the total absorption cross section for photon  $k$  by species  $l$ .  $G_k(\vec{r}_j, \vec{r}_i)$  is Green's function for the survival of the photons emitted at the location  $\vec{r}_j$  to reach location  $\vec{r}_i$ , and also accounts for view angles and obscuration.

Emission of electrons from the dielectric surface results from two processes—secondary electron emission by ion bombardment and photoelectron emission. The values of the electric fields are not large enough for field emission to be important. Electron emission by photons striking surfaces was included with probability 0.01. The UV fluxes striking surface location  $\vec{r}_i$  are given by

$$\phi(\vec{r}_i) = A_k \int N_k(\vec{r}'_j) G_k(\vec{r}'_j, \vec{r}_i) d^3 \vec{r}'_j \quad (2.27)$$

## 2.4 Figures

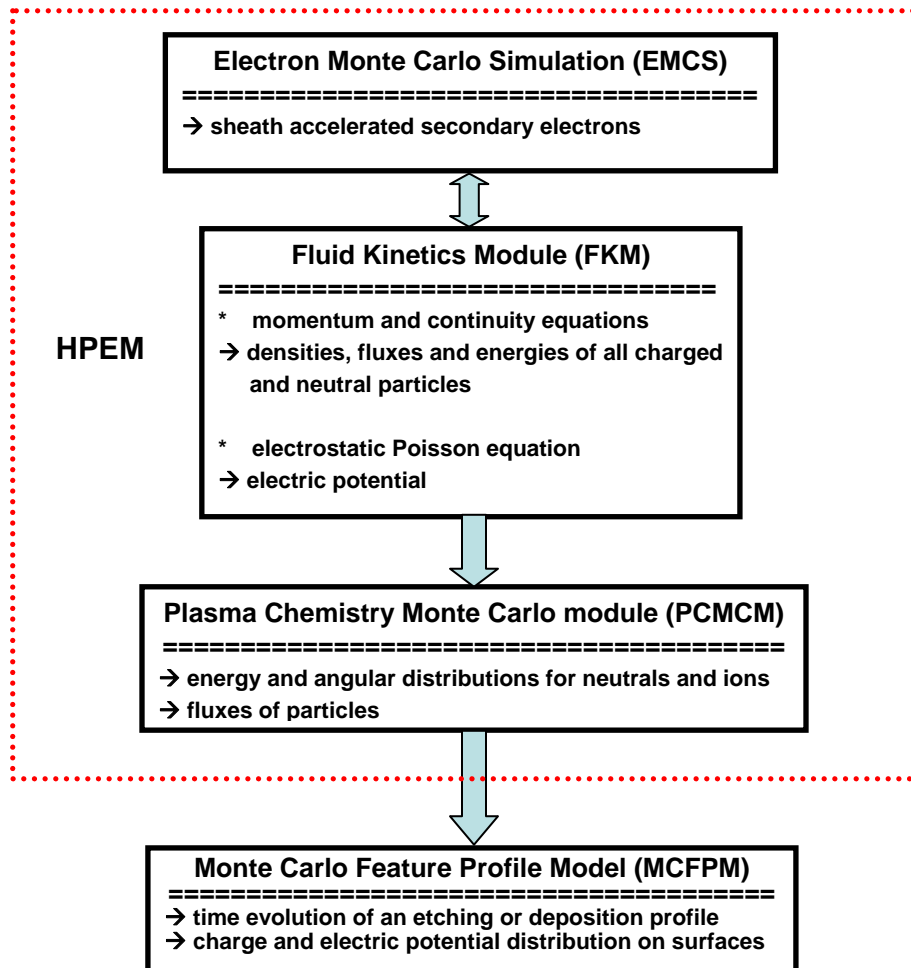


Fig. 2.1 Flow of computational models and their functions.

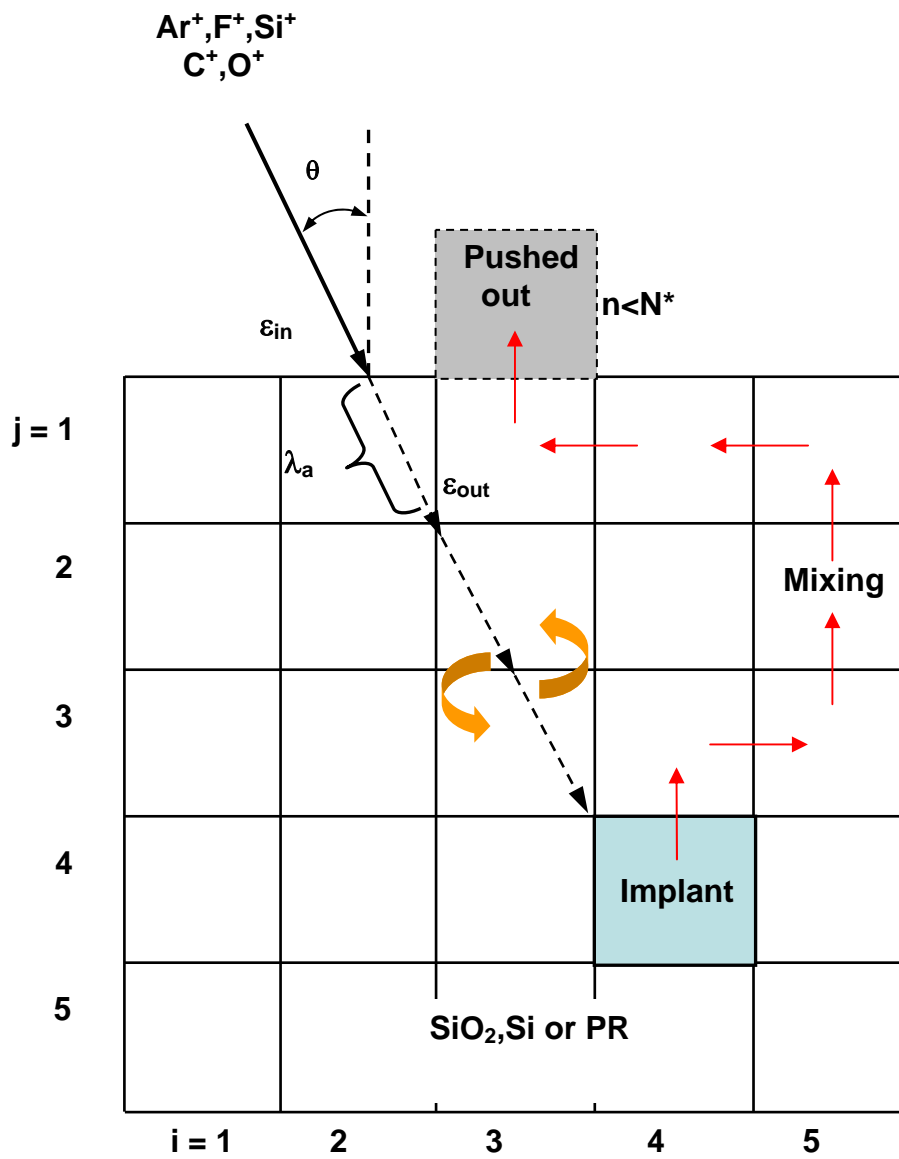


Fig. 2.2 Schematic of implanting and mixing algorithm.

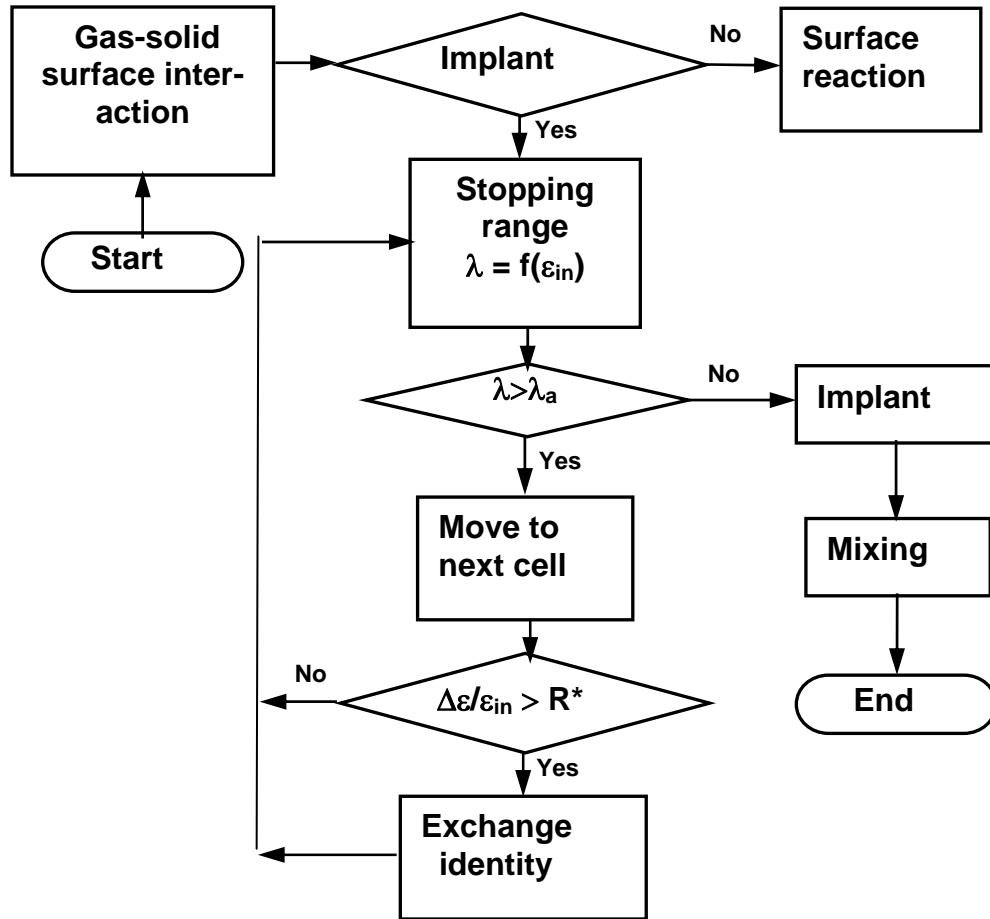


Fig. 2.3 Flow chart of implanting and mixing algorithm.

## 2.5 References

1. D. L. Scharfetter and H. K. Gummel, IEEE T. Electron Dev. **ED-16**, 64 (1969).
2. S. D. Rockwood, Phys. Rev. A, **8**, 2348 (1973).
3. V. E. Skurat and Y. I. Dorofeev, Die Angewandte Makromolekulare Chemie **216**, 205 (1994).
4. NIST Standard Reference Database 17-2Q98 (National Institute of Standards and Technology, Gaithersburg, MD, 1998).
5. J. T. Herron, J. Phys. and Chem. Ref. Data **28**, 1453 (1999).
6. M. R. Wertheimer, A. C. Fozza and A. Hollander, Nucl. Instrum. Meth. B **151**, 65 (1999).
7. R. Wilken, A. Hollander and J. Behnisch, Surf. Coat. Tech. **116-119**, 991 (1999).
8. D. Zhang and M. J. Kushner, J. Vac. Sci. Technol. A **19**, 524 (2001).
9. R. Dorai and M. J. Kushner, J. Phys. D **36**, 666 (2003).
10. B.M. Lay, Richard S Moss, S. Rauf and M. J. Kushner, Plasma Sources Sci. T. **12**, 8 (2003).
11. D. S. Stafford and M. J. Kushner, J. Appl. Phys. **96**, 2451 (2004).
12. F. Truica-Marasescu, P. Jedrzejowski, M. R. Wertheimer, Plasma Proc. Polym. **1**, 153 (2004).

13. E. V. Kuvaldina, V. V. Rybkin, V. A. Titov, T. G. Shikova and D. A. Shutov, High Energ. Chem+ **38**, 411 (2004).
14. M. J. Kushner, J. Phys. D **38**, 1633 (2005).
15. A. Agarwal and M. J. Kushner, J. Vac. Sci. Technol. A **26**, 498 (2008).
16. Y. Yang and M. J. Kushner, Plasma Sources Sci. T. **19**, 055011 (2010).
17. Y. Yang and M. J. Kushner, Plasma Sources Sci. T. **19**, 055012 (2010).
18. R. H. Hansen and H. Schonhorn, J. Poly. Sci., Polymer Letters Edition B, **4**, 203 (1966).
19. M. J. Kushner, J. Appl. Phys. **94**, 1436 (2003).
20. C. K. Purvis, NASA Technical Memorandum 79299, 1979.
21. A. Sankaran and M. J. Kushner, J. Vac. Sci. Technol. A **22**, 1242 (2004).
22. A. Sankaran and M. J. Kushner, J. Vac. Sci. Technol. A **22**, 1260 (2004).
23. A. Agarwal and M. J. Kushner, J. Vac. Sci. Technol. A **27**, 37 (2009).
24. J. F. Ziegler, J. P. Biersack, and U. Littmark, The Stopping and Range of Ions in Solids, (Pergamon, New York, 1985). (Software available from [www.srim.org](http://www.srim.org)).
25. E. H. Lee, G. R. Rao and L. K. Mansur, Radiat. Phys. Chem. **55**, 293 (1999).

26. D. Hegemann, H. Brunner, and C. Oehr, Nucl. Instrum. Meth. Phys. Res. B **208**, 281 (2003).
27. M. J. Titus, D. G. Nest, T-Y Chung and D. B. Graves, J. Phys. D: Appl. Phys. **42**, 245205 (2009).
28. R. Arakoni, D. Shane Stafford, N. Y. Babaeva and M. J. Kushner, J. Appl. Phys. **98**, 073304 (2005).
29. A. N. Bhoj and M. J. Kushner, IEEE T. Plasma Sci. **33**, 250 (2005).
30. N. Yu. Babaeva and M. J. Kushner, J. Phys. D **42**, 132003 (2009).
31. Z. Xiong and M. J. Kushner, J. Phys D **43**, 505204 (2010).
32. Z. Xiong and M. J. Kushner, J. Phys. D **43**, 505204 (2010).

### 3. HIGH ENERGY ELECTRON BEAMS IN DC-AUGMENTED CAPACITIVELY COUPLED PLASMAS I: FUNDAMENTAL CHARACTERISTICS

#### 3.1 Introduction

In this Chapter, the properties of high energy electron (HEE) beams produced in dc-augmented capacitively coupled plasmas (dc-CCPs) sustained in Ar will be discussed with results from a 2-dimensional computational investigation. In Chapter 4, these properties will be used to investigate the means to remedy twisting during HAR etching in SiO<sub>2</sub> using HEE beams produced in dc-CCPs sustained in Ar/C<sub>4</sub>F<sub>8</sub>/O<sub>2</sub> gas mixtures. We found that for a given rf bias power, beams of high energy electrons having narrow angular spread ( $< 1^\circ$ ) can be produced incident on the wafer resulting from secondary electron emission from the dc biased electrode. The maximum energy in the HEE flux scales as  $\mathcal{E}_{max} = -V_{dc} + V_{rf} + V_{rf0}$ , for voltage on the dc electrode of  $V_{dc}$ , rf voltage on the lower electrode of  $V_{rf}$  and dc bias on the rf electrode of  $V_{rf0}$ . Depending on the phase and amplitude the rf voltage, secondary electrons from the dc electrode may be trapped in the plasma. Similarly, HEEs resulting from secondary electrons emitted from the rf biased electrode can reflect from the dc electrode and be incident onto the wafer. The dc current from the biased electrode must return to ground through surfaces other than the rf electrode, presuming a series capacitance with the rf electrode, and so seeks out a ground plane. For our geometry, the ground plane is the side walls of the reactor. If a poorly conducting polymer is deposited on the side wall, the polymer surface will charge to drive the required dc current through the polymer layer.

### 3.2 Capacitively Coupled Plasmas with DC Augmentation

dc-CCPs were investigated using only argon to concentrate on plasma properties. Plasma and HEE properties in a fluorocarbon containing gas mixture will be discussed in Chapter 4. The reactor used for this study is shown in Fig. 3.1. (Note that the vertical scale in Fig. 3.1 is multiplied by 1.5 to provide more vertical resolution.) The substrate, powered at 10 MHz, is 25 cm in diameter and is overlaid with a Si wafer 20 cm in diameter and a Si disk 2.5 cm wide. The substrate is surrounded by a ceramic focus ring ( $\epsilon/\epsilon_0 = 8$ ). The upper electrode to which dc and possibly a second rf bias are applied also serves as a gas shower head. It is 26 cm in diameter and is embedded in a dielectric ( $\epsilon/\epsilon_0 = 8$ ). The dielectric is backed by an electrical ground plane which extends to the side wall. The gap between electrodes is 3.1 cm. An annular pump port surrounds the substrate. Computationally, the pump port passes neutral gas species but is an electrically floating boundary. This was accomplished by having the boundary material for the pump port be a dielectric ( $\epsilon/\epsilon_0 = 10$ ) which passes neutral species.

Powers are separately specified for each applied rf frequency or dc bias. (The rf and dc powers are  $P_{rf}$  and  $P_{dc}$ .) Their voltages are adjusted to deliver those powers. Note that the rf biased substrate generates its own dc bias that is distinct from the applied dc bias on the top electrode. The notation used to describe these voltages are:  $V_{rf}$  is rf voltage applied to the substrate,  $V_{rf0}$  is the self dc bias on the rf electrode and  $V_{dc}$  is the dc bias applied to the upper electrode. In the case of there being two rf frequencies applied,  $V_{LF}$  will refer to the lower of the rf frequencies applied to the substrate and  $V_{HF}$  will refer to the higher frequency applied to the showerhead. All rf voltages are expressed as posi-

tive amplitudes so that  $V_T(t) = V_{rf}\sin(\omega t) + V_{rf0}$  denotes the time dependent voltage on the rf biased substrate. Unless otherwise noted, the secondary electron emission coefficients by ion bombardment,  $\gamma$ , are 0.15 on the top electrode, wafer and Si focus ring; 0.05 on the ceramic focus ring, and 0.025 on the top dielectric and sidewall.  $\gamma$  was independent of ion energy.

The base case is Ar, 40 mTorr with a flow rate of 300 sccm,  $P_{rf} = 300$  W and  $P_{dc} = 200$  W. To deliver these powers,  $V_{rf} = 480$  V,  $V_{rf0} = -286$  V and  $V_{dc} = -523$  V. Plasma characteristics (electron density  $n_e$ , ionization source by bulk electrons,  $S_e$ ; ionization source by beam electrons,  $S_{eb}$ ; and source of charge from the beam electrons,  $S_c$ .) are shown in Fig. 3.2. The electron density has a maximum value of  $3 \times 10^{10} \text{ cm}^{-3}$  and is peaked off-axis due to electric field enhancement at the edge of the electrode. The bulk electrons are excluded from both the rf and dc sheaths, approximately 0.5 cm thick at the top dc electrode and 0.27 cm on the lower rf sheath. The sheaths become thinner at larger radii as the maximum plasma density is approached. Due to there being a fairly uniform electron temperature, 4.2-4.3 eV, the ionization source by bulk electrons mirrors the electron density, and is maximum at  $3.4 \times 10^{15} \text{ cm}^{-3}\text{s}^{-1}$ . The ionization source by HEE resulting from secondary electron emission from all surfaces has a maximum value of roughly half that of the bulk electrons,  $1.8 \times 10^{15} \text{ cm}^{-3}\text{s}^{-1}$ , but provides more than half of the total ionization due to its more uniform distribution. This uniform distribution results from there being secondary electron emission from all surfaces, albeit with varying  $\gamma$ , and there being some pendular motion of secondary electrons trapped between the sheaths.

As discussed by Kawamura *et al.* [1] and Xu *et al.* [2], secondary electrons emitted from the dc electrode can be reflected by the rf sheath and eventually trapped in the plasma. As also discussed below, this will occur if  $V_{rf} - V_{rf0} > V_{dc}$  assuming the secondary electrons first collisionlessly cross the electrode gap. Trapping likely occurs at lower values of  $V_{rf} - V_{rf0}$  given some, on the average, collisional energy loss. In our simulation, trapping occurs when the electron falls below  $\varepsilon_T$  but outside the sheath to allow for electrons to "turn around" in the sheath. The trapping occurs dominantly near the base of the sheaths, as shown in Fig. 3.2d. The charge shown on the surface of the wafer represents those HEEs that are collected by the wafer.

#### A. High Energy Electron Distributions

Electrons produced by secondary emission resulting from ion bombardment of the top electrode are accelerated in the adjoining dc sheath. The disposition of those electrons (that is, do they reach the substrate and with what energy) depends on the relative values of the rf and self-dc bias on the substrate and the dc voltage. Ignoring the floating potential and collisions, and assuming sheath thicknesses are small compared to the gap, electrons emitted from the dc electrode will be accelerated into the plasma with an energy,  $\varepsilon_s$ , equal to the dc voltage. These electrons are then incident on the opposite rf sheath. If the rf sheath is in its cathodic cycle (that is,  $V_T(t) < 0$ ), the HEEs will be decelerated by the rf sheath. If  $V_T(t) < V_{dc}$ , the HEE will be reflected by the rf sheath back into the plasma. Depending on the phase of the rf voltage, the reflected electron may oscillate between the rf and dc sheaths. The electron will be either eventually collected by the rf electrode or thermalized by collisions and be trapped by the positive plasma potential. In

our model, those trapped electrons represent a source of negative charge for the bulk electron distribution or charging of surfaces, as shown in Fig. 3.2b.

If a HEE is incident on the rf electrode when  $V_T(t) > 0$ , the rf sheath will accelerate the electron and increase its energy above  $V_{dc}$ . The maximum value of the secondary electron energy  $\varepsilon_s$  is then  $\varepsilon_{max} = -V_{dc} + V_{rf} + V_{rf0}$  (where  $V_{rf0}$  is typically negative with  $|V_{rf0}| < V_{rf}$ ). The minimum value of  $\varepsilon_s$  is then  $\varepsilon_{min} = \max(0, -V_{dc} - V_{rf} + V_{rf0})$ . For example, the plasma potentials for  $P_{rf} = 300$  W ( $V_{rf} = 460$  V,  $V_{rf0} = -269$  V) and  $P_{dc} = 300$  W ( $V_{dc} = -693$  V) during the rf cycle are shown in Fig. 3.3a. The electron energy distributions (EEDs) incident on the wafer originating from secondary electron emission from all surfaces for this case are shown in Fig. 3.3b. In the absence of collisions (and assuming that the crossing time of electrons is short compared to the rf cycle), the maximum energy of the EED should be 884 eV and the minimum should extend to zero energy. The values obtained from the computed EED agree well with these expectations. Note that the mean free path for inelastic collisions by ionization at the peak energy of the EED, about 900 eV, is nearly 6 cm which is in excess of the gap width. As a result, HEEs nearly ballistically cross the gap on their first crossing.

Note that the plasma potential does not replicate itself on the zero crossings of the rf voltage (lowered by  $V_{rf0}$ ). The plasma potential is higher during the transition from the anodic to cathodic cycle following the escape of bulk electrons to the substrate. This loss of bulk electrons to the substrate leaves the plasma momentarily more electropositive.

EEDs originating from secondary electron emission incident onto the wafer for  $0 \leq P_{dc} \leq 300$  W with  $P_{rf} = 300$  W are shown in Fig. 3.3b. The biases ( $V_{rf}$ ,  $V_{rf0}$  and  $V_{dc}$ ) producing these powers, the maximum electron beam energy, ion fluxes and the ion flux efficiency are shown in Fig. 3.4. (The ion flux efficiency is the total ion flux per Watt of total power deposition scaled to  $P_{dc} = 0$ .) The EEDs generally have a peak at  $\varepsilon_{max}$  corresponding to the collisionless traversal of secondary electrons through the dc sheath and intersecting the substrate at the peak of the anodic rf cycle. The agreement between the computed values of  $\varepsilon_{max}$  and those given by our simple scaling law, shown in Fig. 3.4b, is within the few eV bin size used to compute the EEDs. Since the secondary electrons are emitted essentially randomly through the rf cycle and their crossing times are short compared to the rf cycle, more electrons are collected at the maximum and minimum voltages of the rf cycle. This produces the shoulders to the EEDs at the maximum and minimum energies.

The values of  $V_{dc}$  required to deliver  $P_{dc}$  decrease sub-linearly with  $P_{dc}$ . Had the ion flux remained constant while changing  $P_{dc}$ ,  $V_{dc}$  would have scaled directly with  $P_{dc}$ . However there is an increase in ion flux to the dc electrode when increasing  $P_{dc}$  due to the increase in ionization produced by the HEE. Since  $P_{rf}$  is being held constant,  $V_{rf}$  decreases with increasing  $P_{dc}$  as the ion flux to the substrate also increases. This is accompanied by a decrease (less negative) in the self dc-bias,  $V_{rf0}$ . As  $P_{dc}$  and  $\varepsilon_{max}$  increase, the cross section for ionization decreases for energies above the maximum in the cross section at 120 eV. As a result, the efficiency of ionization decreases with  $P_{dc}$ . As a result of the reduction in their collision cross section, with increasing  $P_{dc}$  a larger fraction of the

secondary electrons emitted by the dc electrode are collected by the substrate without having produced significant ionization.

Note that even with  $P_{dc} = 0$  there is an energetic electron beam component resulting from secondary electrons. Secondary electrons emitted from the grounded upper electrode will gain an energy up to  $V_{rf} + V_{rf0}$  at the anodic part of the rf cycle. As shown by the plasma potentials in Fig. 3.5a, for  $V_{rf} + V_{rf0} = 215$  V and  $V_{dc} = 0$ , there is net acceleration of secondary electrons from the top electrode into the rf substrate near the maximum of the anodic portion of the rf cycle. So it is true that HEE beams onto the wafer exist to some degree in all rf discharges that have secondary electron emission from the surface opposite the wafer. For a given  $V_{rf}$  the energy and magnitude of the flux of the HEEs depends on the self dc bias  $V_{rf0}$ .

To investigate the dependence of the HEE on  $V_{rf} + V_{rf0}$  with  $P_{dc} = 0$ ,  $V_{rf}$  was held constant and  $V_{rf0}$  was independently varied. (Note that this does not constitute a self consistent solution but is indicative of the trends.) The resulting EEDs incident onto the wafer resulting from secondary electron emission and the maximum HEE energies are shown in Figs. 5b and 5c for  $V_{rf} = 510$  V,  $V_{dc} = 0$  and  $-450 \leq V_{rf0} \leq 0$ . The computed maximum energies of the EEDs closely track the theoretical values of  $\epsilon_{max} = V_{rf} + V_{rf0}$ . The distribution of electron energies extends to zero energy, which corresponds to the zero crossing in the rf voltage.

To some degree, dc-CCPs operate as hollow cathodes. Electrons emitted from one electrode are accelerated by the adjacent sheath and, if not degraded by collisions, are

incident on the opposite sheath [1,2]. Depending on the magnitude and phase of the opposite sheath, the incident HEE is either collected or reflected. Assuming that electrons are randomly emitted from the lower electrode during the rf cycle (and ignoring collisions), those electrons emitted when  $-(V_{rf}(t)-V_{rf0}) < -V_{dc}$  will be reflected by the dc sheath. Then depending on the phase of the rf sheath when they arrive at the lower electrode, they will again be either reflected by the rf sheath or collected on the substrate. HEE may undergo many crossings across the gap and reflections from sheaths.

To investigate the proportion and distribution of HEE incident onto the wafer that originate from the rf electrode and have been reflected at least once, the voltages and dc biases were fixed with  $V_{rf} = 510$  V,  $V_{rf0} = -285$  V and  $V_{dc} = -520$  V (conditions similar to the base case). The secondary emission coefficients for the wafer,  $\gamma_{rf}$ , and top electrode,  $\gamma_{dc}$ , were then varied. The results for the normalized energy distribution for HEE flux to the wafer are shown in Fig. 3.6a. The base case (denoted by  $\gamma_0$ ) has  $\gamma_{rf} = \gamma_{dc} = 0.15$ , and is compared to cases having  $\gamma_{rf} = 0$  and  $\gamma_{dc} = 0$ . The high energy portion of the electron flux to the substrate is nearly indistinguishable for  $\gamma_{rf} = 0.15$  and  $\gamma_{rf} = 0$ . This indicates that the vast majority of the high energy electron flux for these conditions originates from the dc electrode.

When  $\gamma_{dc} = 0$ , the flux dominantly consists of a low energy peak contained below 100 eV. This represents electrons emitted from the substrate during that portion of the rf cycle when the voltage is increasing (becoming more positive). Electrons accelerated by the rf sheath are reflected by the dc sheath and return to the rf electrode when the sheath voltage is less negative. These electrons can climb the sheath potential to reach the wafer.

The energy of the collected HEE is approximately equal to the difference in the rf sheath potential over the time required for the HEE to make two gap crossings. Electrons emitted from the substrate during the portion of the rf cycle when the rf voltage is decreasing will be trapped since the sheath potential is more negative after two crossing times than when the electron was originally emitted. There are sporadically collected electrons with energies as high as 700 eV. This likely results from ionizations produced by the secondary electrons in the dc sheath. The fluxes with  $\gamma_{rf} = 0$  are diminished by about 1/3 for energies  $< 50$  eV compared to  $\gamma_{rf} = 0.15$ . This reduction in flux is due to the absence of electrons emitted from the rf electrode which are reflected by the dc sheath and collected by the wafer.

Since the ion fluxes to the electrodes change when  $\gamma$  is varied due to the change in the contribution of ionization by HEE, the magnitudes of the HEE fluxes produced by the ion fluxes also change. By normalizing the HEE fluxes by the magnitudes of the ion fluxes, the relative contributions of electrons from the rf and dc electrodes to the HEE flux to the wafer can be determined. Approximately 1/3 of the total HEE flux to the wafer (albeit, dominantly below 100 eV) originates from secondary emission from the rf electrode. The remainder (and the vast majority at energies  $>100$  eV) originates from secondary emission from the dc electrode.

The angular distributions of HEEs incident on the wafer are shown in Fig. 3.6b. With  $\gamma_0$  and  $\gamma_{rf} = 0$ , the HEE flux is nearly fully contained within  $0.5^\circ$  of the vertical. Small asymmetries in angle result from two causes. The first is curvature of the dc sheath due to the non-uniform plasma density across the upper electrode. This curvature

generates a small off-normal component to the electric field in the sheath which produces a non-normal trajectory. The second cause is electric field enhancement at the edge of the rf electrode that also produces lateral components of the electric field in the sheath. For  $\gamma_{dc} = 0$ , the majority of the HEE flux is also contained within  $0.5^\circ$  of the vertical, however there is a broad base to the angular distribution due to electrons collected below 30 eV.

## B. Collection of dc Current

The dc augmentation on the upper electrode produces a time averaged dc current that must be returned to ground. Since the substrate is capacitively coupled it cannot pass a time averaged dc current, and so the current must seek another path to ground. In this particular geometry, the only non-dielectric covered surface (or only surface not capacitively coupled) is the metal side wall. (Recall that we prevented dc current from passing through the pump port by covering it with a dielectric). As a result, the dc current must return to ground through the side wall.

For example, the rf cycle averaged magnitude of the current density and current density vectors (showing direction but not magnitude) are shown in Fig. 3.7 for  $P_{dc} = 100$  W and 300 W. This current density results from the ions and the bulk electrons, but does not show the contribution of beam electrons which at most would provide approximately  $\gamma$  of the total at the electrode. The dc current density comes out of the side wall, converges through the gap at the edge of the dc electrode as the radius decreases and is dispersed along the surface of the showerhead. The maximum current density of 2.8 mA/cm<sup>2</sup> for 100 W occurs mid-gap a few cm from the edge of the dc electrode. In order

to drive this current, there is a small time averaged electric field from the electrode to the side walls. The dc current density at 300 W closely resembles that of the 100 W case. The peak current density of  $4.2 \text{ mA/cm}^2$  is less than twice that of the lower power. The increase in dc power is accomplished by increasing voltage ( $-325 \text{ V}$  for 100 W and  $-690 \text{ V}$  at 300 W) as well as by increasing current density.

Although the capacitively coupled substrate must, on a cycle averaged basis, pass no dc current, that requirement applies only to the areal integral of the current density. It does not apply locally if there is any significant surface conductivity. In our model, we allowed the wafer to have a finite conductivity ( $0.01/\text{Ohm-cm}$ ) and so it may pass a dc current in the radial direction. The end result is that there is a small dc current that is collected at inner radii on the wafer and returned to the plasma at the outer radii with the areal integral being zero. (Had the substrate been a non-conducting dielectric, the zero-current condition would have been enforced locally as well as globally.) These dc current densities are small (peak values  $< 0.1 \text{ mA/cm}^2$ ) and are produced by the plasma being non-uniform. In this case the plasma has a maximum near the edge of the electrode which produces a higher electron beam current by secondary electron emission from the dc electrode. This current is collected on the edge of the wafer and so produces a positive current into the plasma. In this particular case, the recirculating current is largely attributable to the contributions of the HEEs to the wafer. The recirculating current does not occur with  $P_{dc} = 0$ .

Plasma etching is often conducted in polymerizing gas mixtures which deposit polymer films on all surfaces in contact with the plasma. For example,  $\text{Ar/C}_4\text{F}_8/\text{O}_2$  gas

mixtures are used to etch dielectric materials such as  $\text{SiO}_2$  [3]. During a few minute process, many to tens of microns of nominally poorly conducting polymer may be deposited on the inner sidewalls of the reactor. In conventional CCPs, the polymer deposition is not particularly important from the vantage point of the circuit. The polymer layer is thin enough, and its capacitance high enough, that rf current is not significantly impeded by the polymer. (Note that this polymer deposition can change reactive sticking coefficients for radicals and so contribute to the seasoning or drift of reactors. See, for example, Ref. [4]) The deposition of polymer on the sidewalls is problematic in dc-CCPs as the sidewall is the location where the dc-current returns to ground. The low-conducting nature of the polymer may impede or block the dc current.

To investigate the consequences of polymer deposition on sidewalls in dc-CCPs, we added a layer of dielectric to the sidewall with a thickness of 3 mm and conductivity of either  $0.1 \text{ /Ohm-cm}$  (high conductivity) or  $10^{-5} \text{ /Ohm-cm}$  (low conductivity). The dielectric constant of the polymer was adjusted so that its capacitance would be similar to that of a polymer layer of a few hundred microns thickness. This capacitance is high enough to pass the rf current unimpeded. The conditions are otherwise the same as the base case (Ar, 40 mTorr,  $P_{rf} = 300 \text{ W}$ ,  $P_{dc} = 200 \text{ W}$ ). The cycle averaged plasma potential as a function of radius at the middle of the gap is shown for the low and high conductivity cases in Fig. 3.8a. The high conductivity polymer is able to pass the dc current with a negligible voltage drop. In the low conductivity case, the polymer charges to a negative potential, approximately -20 V, to create a large enough electric field in the polymer to drive the electron current through the polymer into the sidewall. Since the

metal sidewall is the reference electrode for the plasma potential, the time averaged plasma potential is decreased by the amount of the voltage drop across the polymer.

The resulting IEADs and EEDs incident onto the wafer are shown in Fig. 3.8b for the high and low conductivity cases. The IEADs are nearly unchanged between the two cases. This is in part because the characteristics of the IEADs are determined by  $V_{rf}$ ,  $V_{rf0}$ , and the rf current, all of which are largely unaffected by the polymer on the sidewall since its capacitance is large enough to pass the rf current.  $V_{rf} - V_{rf0}$  increases from 810 V to 820 V from the low to high conductivity cases. The maximum energy of the HEE decreases by approximately 20 eV from the low to high conductivity case. There is a small 5 V increase (more negative) in  $V_{dc}$  to deliver  $P_{dc} = 200$  W which might increase  $\epsilon_{max}$ . However  $V_{rf0}$  becomes more negative which then reduces  $\epsilon_{max}$ .

To independently investigate the dependence of the HEEs and IEADs on the polymer sidewall coverage,  $V_{rf}$  (480 V)  $V_{rf0}$ , (-285 V) and  $V_{dc}$  (-520 V) were held constant as opposed to adjusting them to deliver specified powers. These resulting distributions are shown in Fig. 3.8c for polymer conductivities of 0.1,  $10^{-5}$  and  $10^{-6}$  Ohm<sup>-1</sup>-cm<sup>-1</sup>. Since  $V_{rf}$ ,  $V_{rf0}$ , and  $V_{dc}$  are constant the HEEs are largely collisionless and the HEEs traverse the gap in a small fraction of the rf period, the EEDs do not significantly change as the polymer conductivity changes. The IEADs incident on the substrate are, however, sensitive to the polymer conductivity. Although the average ion energy is independent of the polymer conductivity since  $V_{rf}$  and  $V_{rf0}$  are the same, the shape of the IEAD reflects differences in the time dependence of the plasma potential. With the lower conductivity polymer the plasma potential remains at its maximum value during the cathodic part of

the rf cycle for a larger fraction of the cycle, and so the high energy peak of the IEAD is more prominent.

### C. Two Frequency CCP

One implementation of the dc-CCP uses two rf frequencies – a low frequency (LF  $\leq 10$  MHz) on the substrate and a high frequency (HF  $\geq 40$ -100 MHz) on the opposite dc biased electrode. The goal of the two frequency excitation scheme is to separate ion acceleration, more efficiently produced by the LF, from plasma generation, more efficiently produced by the HF. So given that in practice the amplitude of the HF voltage,  $V_{HF}$ , is less than the magnitude of  $V_{dc}$ , the top electrode becomes biased with an rf-modulated-dc potential.

To isolate the effects of adding a HF to the dc biased electrode,  $V_{LF}$  (480 V) and  $V_{rf0}$ , (-285 V) on the lower electrode, and  $V_{dc}$  (-520 V) on the top electrode were held constant while varying  $V_{HF}$ . The LF is 5 MHz and the HF is 40 MHz for 40 mTorr of argon. The EEDs incident onto the wafer resulting from secondary electron emission for  $V_{HF} = 0, 150$  V and 300 V are shown in Fig. 3.9. With  $V_{HF} = 0$ , the EED has a maximum energy of 715 eV, which corresponds to  $\epsilon_{max} = -V_{dc} + V_{LF} + V_{rf0}$ . The peak of the EED at  $\epsilon_{max}$  results from the longer dwell time of the substrate bias at the maximum of the anodic cycle. With  $V_{HF} = 150$  V and 300 V, the dc bias is modulated on the top electrode with a sinusoidal  $V_{HF}$ . The discrete peaks in the EED correspond to a full cycle of modulation of the dc voltage at the HF as the phase of the LF more slowly changes. The maximum energy of the EED is  $\epsilon_{max} = -V_{dc} + V_{LF} + V_{rf0} + V_{HF}$  or 865 eV for  $V_{HF} = 150$  V and

1,015 eV for  $V_{HF} = 300$  V. The computed values are 853 eV and 993 eV. The lower computed values result from the finite crossing time across the gap of secondary electrons emitted from the dc electrode. In order to gain an energy  $\epsilon_{max}$ , a secondary electron must be emitted at the maximum of the cathodic part of the HF cycle and strike the LF electrode at the maximum of its anodic cycle. In this example, the LF and HF have the same phase and the crossing time across the gap of a 1 keV electron is approximately 2 ns. So during the time between emission of the electron at the HF electrode and it being collected at the LF electrode, the substrate voltage will have decreased by about 24 V, which accounts for the difference between the theoretical and computed values. The HEE distribution onto the substrate can therefore be tuned to some degree by the phase differences and frequencies of the LF and HF potentials.

#### D. Low Frequency

In many applications of HAR etching, particularly in dual frequency CCPs, the substrate bias is at frequencies as low as 1–2 MHz. To investigate the consequences of the frequency of the substrate bias on the EEDs incident on the wafer resulting from secondary electron emission, the substrate bias was varied between 2 and 16 MHz. Again, to isolate the effects of changing only the frequency of the substrate bias,  $V_{rf}$  (480 V) and  $V_{rf0}$  (–285 V) on the lower electrode and  $V_{dc}$  (–520 V) on the top electrode were held constant. The resulting EEDs are shown in Fig. 3.10. On the scale of the entire range of energies, the EEDs for frequencies of 2–16 MHz are nearly indistinguishable. The high energy peak of the EED and the maximum electron energy do, however, systematically vary. The peak

and maximum energy decrease with increasing frequency. For a bias of 2 MHz, the maximum energy is 712 eV, which is nearly the same as the maximum theoretical energy of  $\epsilon_{max} = -V_{dc} + V_{rf} + V_{rf0}$  or 715 eV. The maximum energy decreases to 702 eV at 16 MHz. This is in large part a transit time effect. In order for a secondary electron to gain the maximum energy, it must be emitted from the dc biased electrode at the peak of the anodic cycle and cross the electrode gap before the substrate bias appreciably changes. The time required for a 700 eV electron to cross the electrode gap is about 1.8 ns. During this time, the voltage on the substrate near the peak of the anodic cycle at 16 MHz will have changed by 10 eV. Electrons emitted from the dc electrode on the ascending portion of the anodic cycle (bias becoming more positive) will gain energy larger than that corresponding to the phase of their emission because the substrate sheath potential is increasing during its transit time. Electrons emitted at the peak and descending portion of the rf cycle (bias becoming more negative) will gain less energy, in this case about 10 eV at 16 MHz.

### 3.3 Concluding Remarks

HEE characteristics and scaling laws were computationally investigated in single and dual frequency dc-CCPs. Electrons emitted from either the rf or dc electrodes are accelerated by the adjacent sheath and, if not degraded by collisions, are incident on the opposite sheath. Depending on the magnitude and phase of the rf sheath, the incident HEE from the dc electrode is either collected or reflected. HEEs from the dc electrode are collected with energies  $\max(0, -V_{dc} - V_{rf} + V_{rf0}) < \epsilon_s < -V_{dc} + V_{rf} + V_{rf0}$ . Even with  $V_{dc} = 0$ , HEE fluxes as large as  $V_{rf} + V_{rf0}$  can be collected by the wafer. Approximately

30% of the HEE flux collected by the wafer, mostly at energies  $< 100$  eV, can be attributed to secondary electrons emitted by the substrate and reflected by the dc sheath. The current emitted by the dc electrode must return to ground through a non-capacitively coupled surface. In our model, that surface is the grounded sidewall. When the sidewall is coated with poorly-conducting polymer, charge will build up to push the dc current through the coating. This could result in sparking under extreme conditions. When applying a HF bias to the dc electrode, the HEE flux is modulated by the HF voltage. The precise energy spectrum of the HEE flux collected by the substrate then depends on the relative phases of the LF and HF biases. The HEE distribution onto the substrate can therefore be tuned to some degree by the phase differences and frequencies of the LF and HF potentials. The consequences of HEE fluxes on etching of high-aspect-ratio  $\text{SiO}_2$  features using fluorocarbon plasmas are discussed in Chapter 4.



## 3.4 Figures

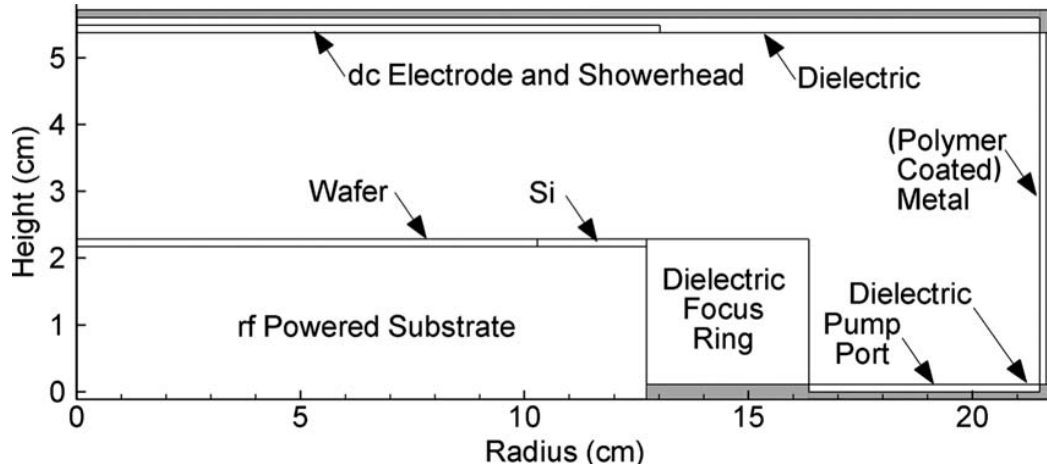


**Fig. 3.1** Schematic of the dc-CCP reactor. The vertical scale is multiplied by 1.5 for clarity.

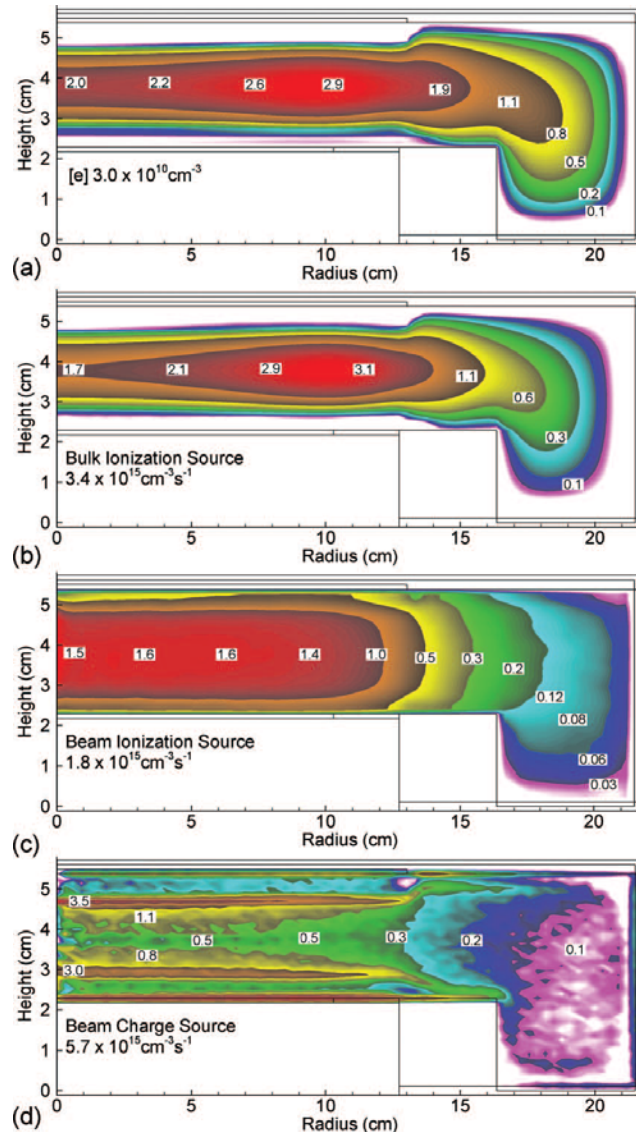


**Fig. 3.2** Plasma characteristics for the base case (Ar, 40 mTorr, 300 sccm,  $P_{rf} = 300$  W and  $P_{dc} = 200$  W]. (a) Electron density; (b) ionization source by bulk electrons  $S_e$ , (c) ionization source by beam electrons,  $S_{eb}$ ; and (d) source of charge from the beam electrons. Contours span 2-decades on a log-scale with maximum values shown in each frame. Note the exclusion of electrons from the dc sheath.

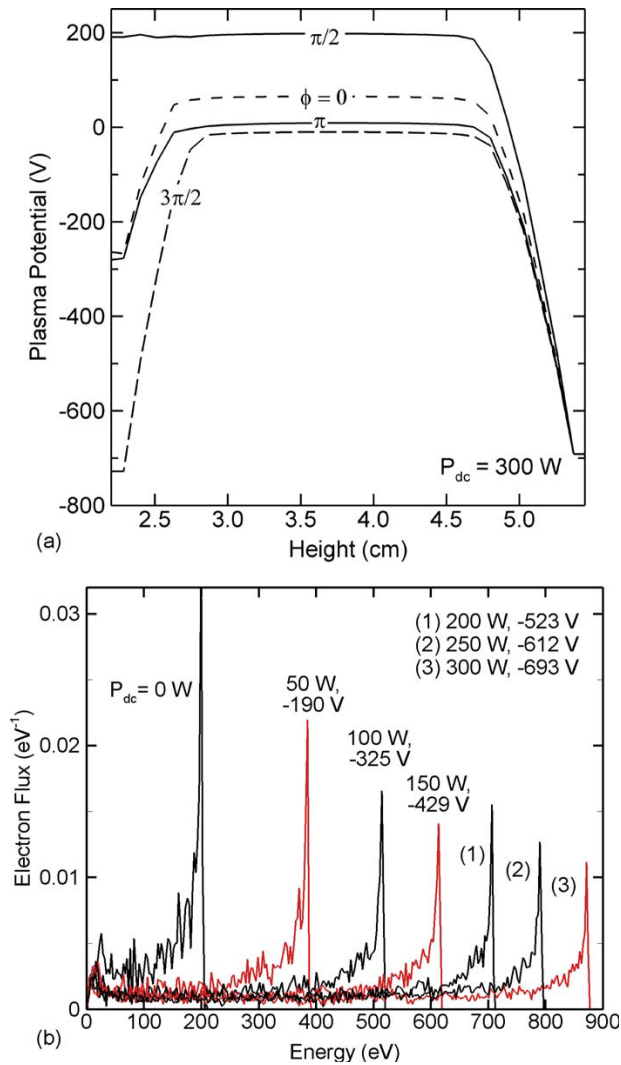


**Fig. 3.3** Plasma properties as a function of  $P_{dc}$  (Ar, 40 mTorr, 300 sccm,  $P_{rf} = 300$  W). (a) Plasma potential for  $P_{dc} = 300$  W at different phases during the rf cycle as a function of height at a radius of 5 cm. The rf electrode is at the left and the dc electrode is at the right. (b) EEDs incident on the wafer originating from secondary electron emission from all surfaces for different  $P_{rf}$  (with the value of  $V_{dc}$  noted). Even in the absence of  $P_{dc}$ , HEE fluxes are collected on the wafer.

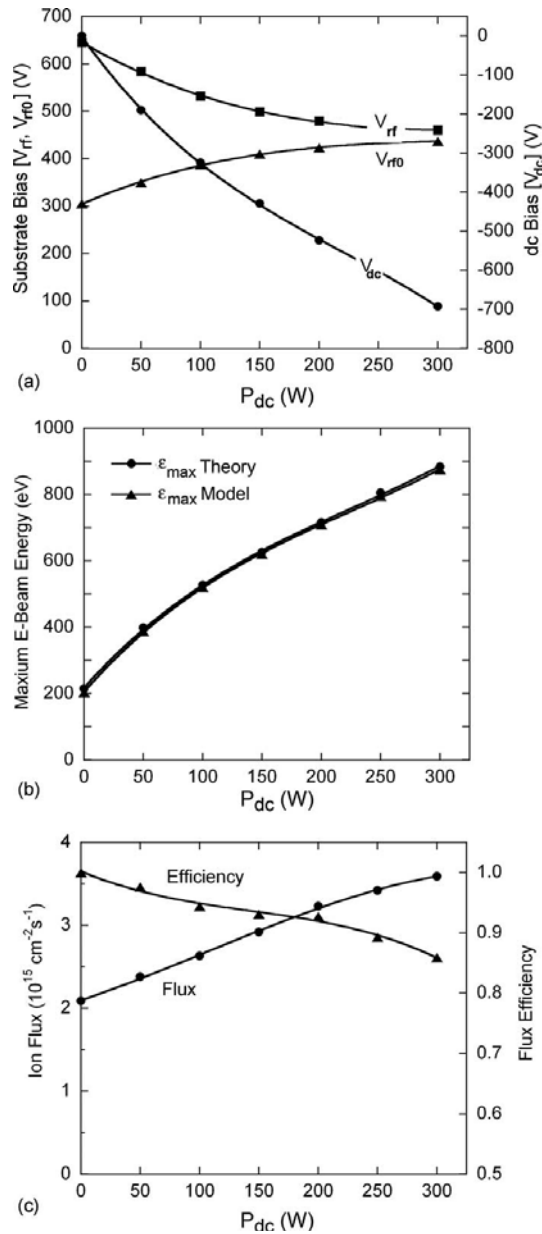


**Fig. 3.4 HEE properties as a function of  $P_{dc}$  (Ar, 40 mTorr, 300 sccm,  $P_{rf}=300$  W). (a)  $V_{rf}$ ,  $V_{rf0}$  and  $V_{dc}$  as a function of  $P_{dc}$ ; (b) Maximum e-beam energy as a function of  $P_{dc}$  (computed and theory) and (c) Ion flux and flux efficiency as a function of  $P_{dc}$ . The flux efficiency is a measure of the ability of the HEEs to increase the ion flux to the wafer.**

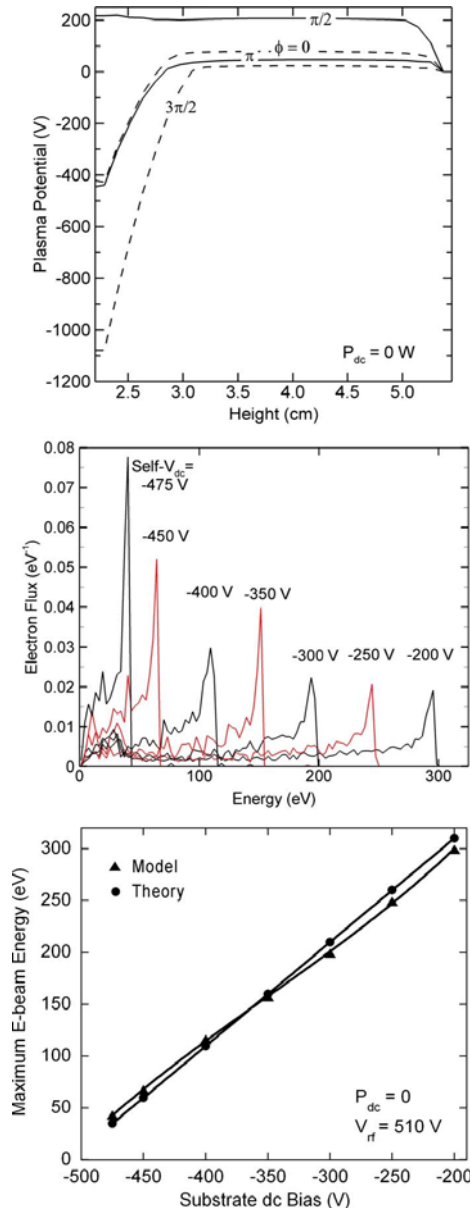


**Fig. 3.5** Plasma properties for  $P_{dc} = 0$  while varying the dc bias on the blocking capacitor on the rf electrode,  $V_{rf0}$ .  $V_{rf}$  is held constant at 510 V. (a) Plasma potential at different phases during the rf cycle for  $V_{rf0} = -450$  V. (b) EEDs for the HEE flux onto the wafer as a function of  $V_{rf0}$ . (c) Simulated results and theory for the maximum HEE energy as a function of  $V_{rf0}$ .

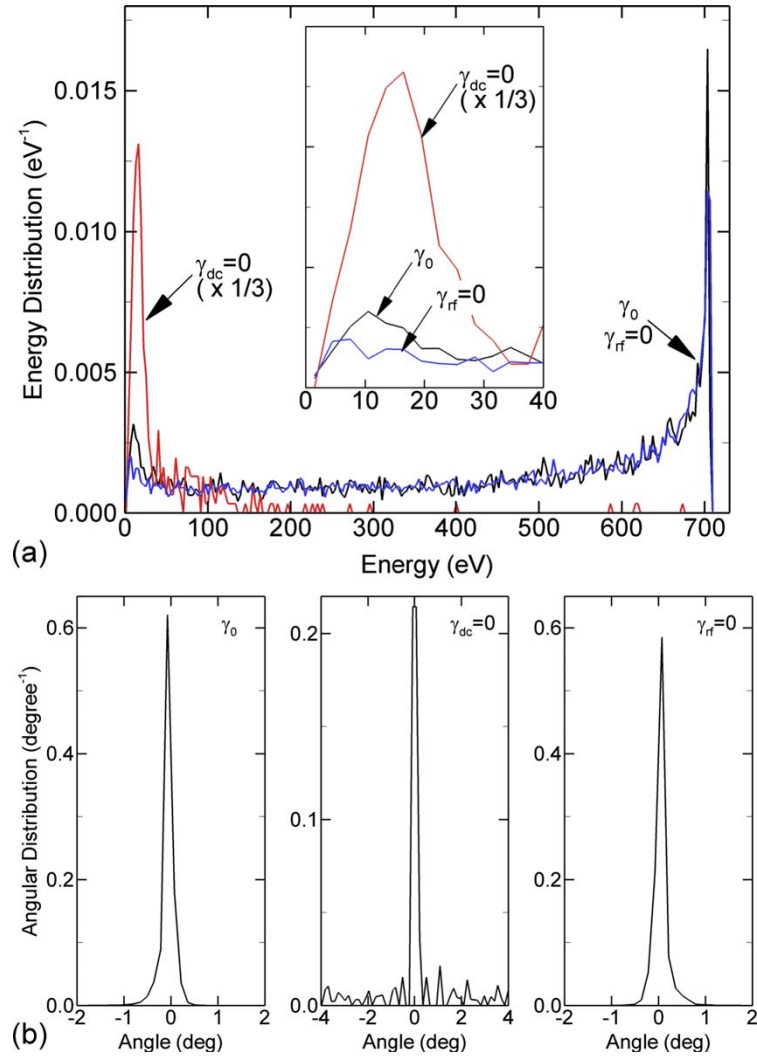


**Fig. 3.6** Energy and angular distributions for HEEs incident on the electrode. (a) EEDs at different secondary emission coefficients [ $\gamma_0$ , ( $\gamma_{dc}=\gamma_{rf}=0.15$ );  $\gamma_{dc}=0.15$ ,  $\gamma_{rf}=0$ ; and  $\gamma_{dc}=0$ ,  $\gamma_{rf}=0.15$ ]; (b) Angular distributions for different  $\gamma$ . The vast majority of the electron flux about 100 eV results from secondary emission from the dc electrode.

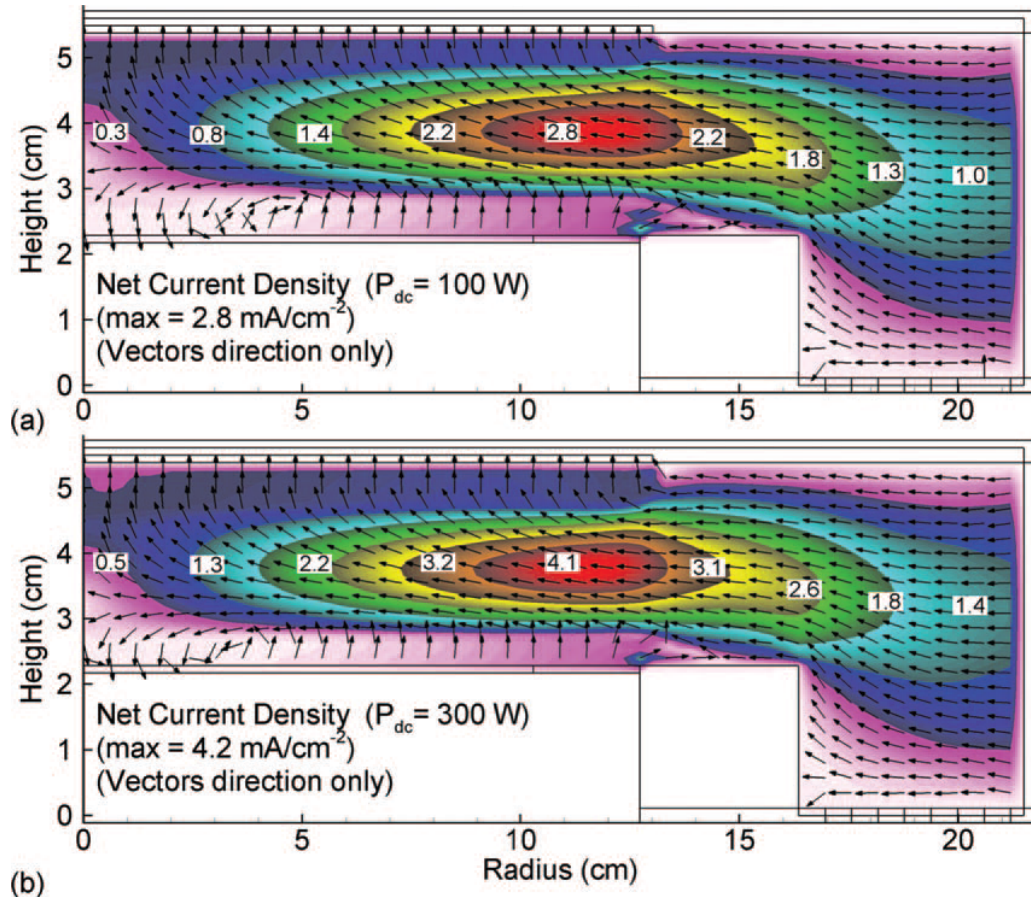


**Fig. 3.7** The rf cycle averaged magnitude of the current density and current density vectors for (a)  $P_{dc} = 100 \text{ W}$  and  $P_{dc} = 300 \text{ W}$ . The maximum value for each case is noted. The vectors show direction only (not magnitude). A net current flows from the dc electrode to the sidewalls.

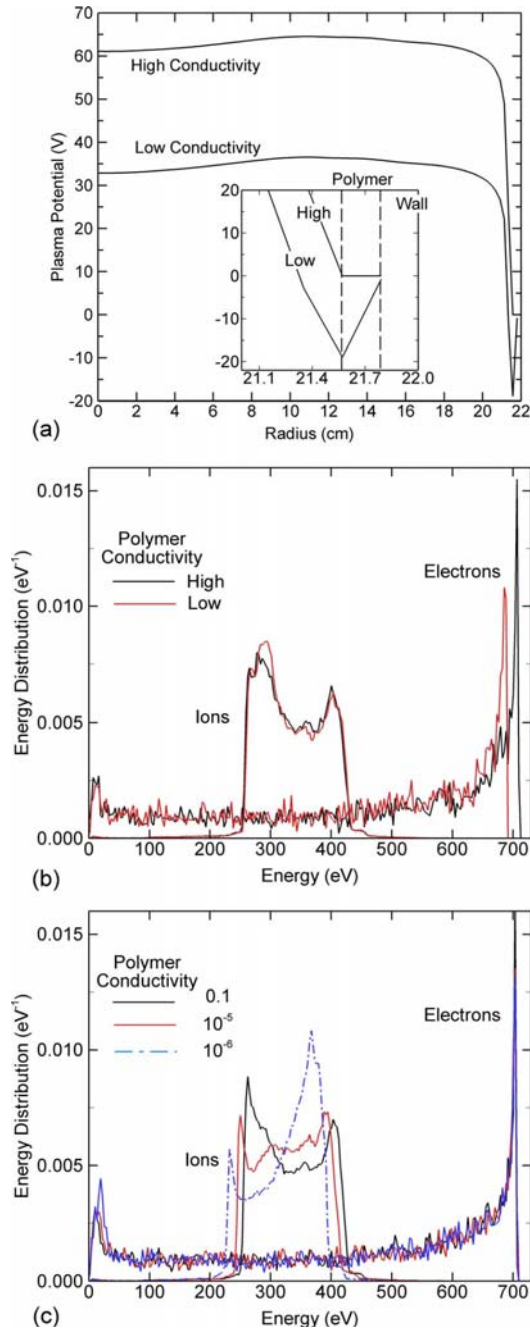


**Fig. 3.8** Consequences of polymer deposition on the sidewalls. (a) Cycle averaged plasma potential at the middle of the gap as a function of radius. The polymer on the sidewall has conductivities of  $0.1$  and  $10^{-5} \Omega^{-1}\text{-cm}^{-1}$ . (b) Energy distributions of ions and HEE for low ( $10^{-5} \Omega^{-1}\text{-cm}^{-1}$ ) and high ( $0.1 \text{ Ohm}^{-1}\text{-cm}^{-1}$ ) conductivity polymer. (c) Energy distributions of ions and HEE for polymer conductivities of  $0.1$ ,  $10^{-5}$  and  $10^{-6} \text{ ohm}^{-1}\text{-cm}^{-1}$  at fixed bias voltages of  $V_{rf} = 480 \text{ V}$ ,  $V_{rf0} = -285 \text{ V}$  and  $V_{dc} = -520 \text{ V}$ .

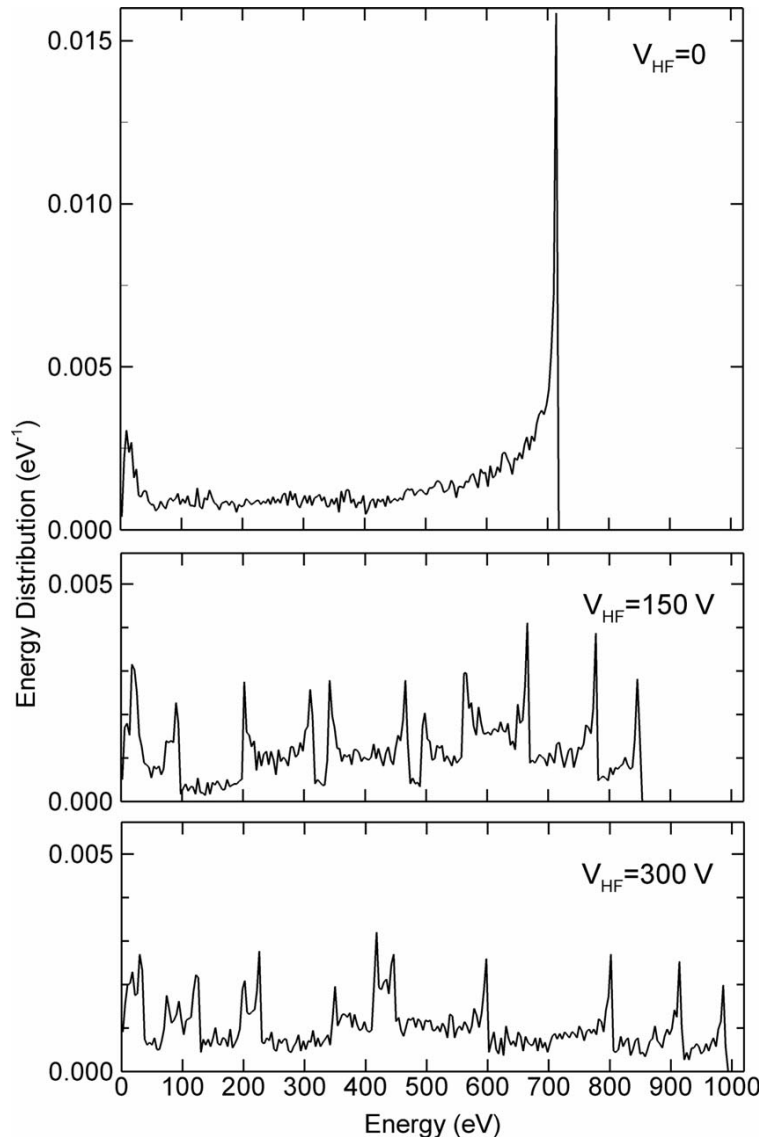


**Fig. 3.9** EEDs incident onto the wafer resulting from secondary electron emission for a dual frequency dc-CCP for  $V_{HF}$  = (top) 0, (middle) 150 and (bottom) 300 V. The other voltages ( $V_{LF}=480\text{ V}$ ,  $V_{rf0}=-285\text{ V}$ ,  $V_{dc}=-520\text{ V}$ ) were held constant. The HEE flux onto the wafer is modulated by  $V_{HF}$  displaced by the change in LF voltage during the time the electron crosses the gap.

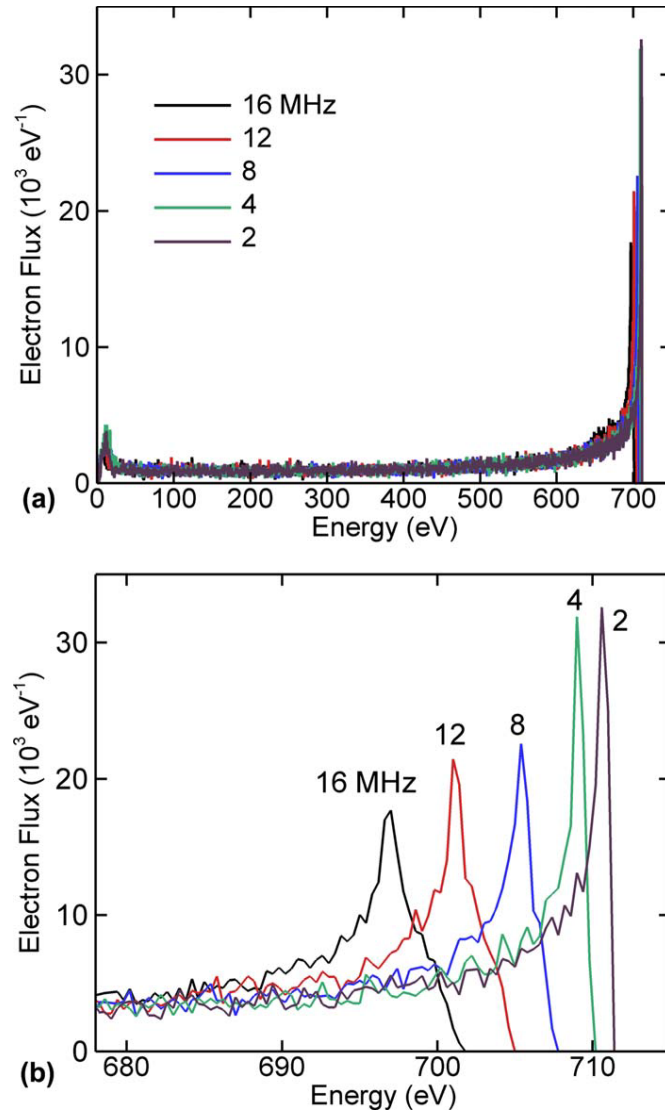


**Fig. 3.10** EEDs for HEE fluxes incident onto the wafer resulting from secondary electron emission while varying the frequency of the bias on the lower electrode. (a) Full energy range and (b) expansion of scale at high energy. The voltages ( $V_{rf}=480 \text{ V}$ ,  $V_{rf0}=-285 \text{ V}$ , and  $V_{dc}=-520 \text{ V}$ ) were held constant. The HEE flux onto the wafer is not significantly changed by the bias frequency though the maximum energy decreases by a few electron volts at high energy due to the finite cross time of secondary electrons.

### 3.5 References

1. E. Kawamura, A.J. Lichtenberg and M.A. Lieberman, Plasma Sources Sci. Technol. **17**, 045002 (2008).
2. L. Xu, et al. Appl. Phys. Lett. **93**, 261502 (2008).
3. X. Li et al., J. Vac. Sci. Technol. A **21**, 284 (2003).
4. B. Zhou, E. A. Joseph, S. P. Sant, Y. Liu, A. Radhakrishnan, L. J. Overzet, and M. J. Goeckner, J. Vac. Sci. Technol. A **23**, 1657 (2005).

## **4. HIGH ENERGY ELECTRON FLUXES IN DC-AUGMENTED CAPACITIVELY COUPLED PLASMAS II: EFFECTS ON TWISTING IN HIGH ASPECT RATIO ETCHING OF DIELECTRICS**

### **4.1 Introduction**

In high aspect ratio (HAR) plasma etching of holes and trenches in dielectrics, sporadic twisting is often observed. Twisting is the randomly occurring divergence of a hole or trench from the vertical. Many explanations have been proposed for twisting, the majority of which attribute twisting to non-uniform macro-scale parameters, such as ion and neutral energy-angular distributions and fluxes. These could, in principle, be controlled by adjusting reactor parameters (e.g., pressure [4], bias power [5] and frequency [6]). For example, methods have been proposed in the patent literature to control twisting by judicious choice of frequencies and powers in multi-frequency excited capacitively coupled plasmas [7]. Optimizing these quantities have been demonstrated to reduce the incidence of twisting. Twisting can, however, occur errantly and randomly within a field of features having a pitch of only a few microns whereas the scaling length for significant changes in the magnitude of fluxes and energy distributions of ions and neutrals is at least many mm in low pressure (< tens of mTorr) plasmas. Therefore, it is likely that sporadic twisting with feature-to-feature variations having many micron scale-lengths may have causes in addition to variations in these macroscopic quantities (e.g., radial uniformity of fluxes) having scale lengths of many mm to cm.

A contributing explanation for feature-to-feature variations in profiles and twisting may originate from the small size of the feature open to the plasma. For example, for a hole 50 nm in diameter, the area of the opening to the plasma is 2000 nm<sup>2</sup>. With this

small opening, the rate of entry of radicals and ions into the feature begins to become statistical. The time between the arrival of two ions into a feature 50 nm in diameter for a flux of  $10^{16} \text{ cm}^{-2}\text{-s}^{-1}$  is 5  $\mu\text{s}$ . This small rate of particle arrival can lead to feature-to-feature statistical variations in both the identity and number of particles entering the feature. These statistical variations are particularly important in polymerizing gas mixtures for which the rate of etching depends not only on the ion energy but also the previous history of arrival of radicals which determines the polymer thickness and composition. Variations in fluxes that result in thicker polymer on one side of the feature compared to the other which slows its etch rate could produce asymmetric etch profiles.

The statistical variation of charged species into the feature (both ions and electrons) could also play an important role in twisting. Charging of the surfaces inside the feature will occur in dielectric etching or in conductor etching using polymerizing gas mixtures which deposit an insulating layer that charges or traps charge. The statistical variation in charged particle fluxes into the feature could charge one side of the feature more than the other. This charging could then produce asymmetrical electric fields that deflect subsequent ions from the vertical and so produce twisting.

The charging of high aspect ratio (HAR) features in plasma etching has been investigated by many researchers [8-10]. The general view of this process is that isotropic fluxes of low energy electrons negatively charge the top of the features. High energy positive ions which have a narrow angular distribution after being accelerated through the sheath penetrate deeper into features and positively charge the bottom of the feature. Depending on thickness of the mask, which is typically charged up negatively by thermal electrons, twisting, bowing, or micro-trenching may occur [11,12]. In HAR etching, ions

are usually energetic enough not to be significantly affected by the negative charge at the top of the feature and respond dominantly to the positive charge deeper in the feature. This process is dynamic. If the only effect was ions charging the bottom of the trench, the electric potential at the bottom of the trench would increase positively to the point of preventing further ion bombardment. At that point, only energetic neutrals originating from ions neutralized by grazing collisions with the side walls at the top of the feature would reach the bottom of the feature with sufficient energy to activate the etch. An alternate scenario is that electrons are attracted deep into the feature by the positive potential and neutralize positive charge which reduces the positive potential. This then allows further positive ion bombardment.

Many technologies have been developed to control or prevent intra-feature charging, one method being neutral beam etching [13]. One neutral beam technique is to extract ions from a plasma while neutralizing the ions by passing them through a grid [14,15]. Although very promising, this technique typically produces ions having lower incident energies with broader angular spreads than produced by high voltage rf biases. These fluxes may not be optimum for HAR application. A second method of controlling charging of features involves depositing a fluorocarbon or carbon film into the features which becomes mildly conductive after bombardment by high energy ions. The conductive film dissipates charge more quickly than the underlying  $\text{SiO}_2$  [16]. This technique has been specifically applied to the control of twisting by reducing intra-feature charging [17]. A third method is injecting negative charge into the feature to neutralize accumulated positive charge. There are two approaches to reach this goal. One approach utilizes pulsed ion-ion plasmas to inject negative ions into the feature [18,19]. The second ap-

proach, investigated here, produces and injects a narrow angle, high energy electron (HEE) flux into the feature.

HEE fluxes onto wafers can be produced in dc augmented capacitively coupled plasmas (dc-CCPs). In these reactors, a dc voltage is applied to the electrode opposite the rf biased substrate. Secondary electron emission from the dc biased substrate produces HEE fluxes having energies up to a few keV with angular spreads of  $< 0.5^\circ$ . The characteristics of HEE fluxes produced in dc-CCP reactors are discussed in Chapter 3 including a review of prior works [20-22].

In this Chapter, results are discussed from a computational study of a dc-CCP for etching of HAR features in  $\text{SiO}_2$  over Si. The model system is a parallel plate CCP with a 10 MHz bias on the lower electrode; and a dc bias on the upper electrode. Characteristics of dc-CCP's sustained in  $\text{Ar}/\text{C}_4\text{F}_8/\text{O}_2$  and properties of HAR etch profiles with and without HEE fluxes are discussed. We found that the occurrence of twisting generally decreases with increasing HEE fluxes and increasing maximum energy of that flux. This effect is attributed to the penetration of electrons into the features which neutralize positive charge.

## 4.2 Bulk Plasma Properties

A schematic of the cylindrically symmetric dc-CCP reactor used in this study is shown in Fig. 4.1. The chamber is 43 cm in diameter. The powered substrate is 26 cm in diameter, and holds a 20 cm diameter Si wafer which is surrounded by a 3 cm wide Si disk. A focus ring ( $\epsilon/\epsilon_0=8$ ) extends beyond the Si disk to a diameter of 32 cm. The substrate is powered at 10 MHz through a blocking capacitor. The rf voltage was adjusted to

deliver a specified power unless noted otherwise. The metal showerhead, having a diameter of 26 cm, is embedded in a dielectric ( $\epsilon/\epsilon_0=8$ ) and is dc biased. The dc voltage was also adjusted to deliver a specified power. The wafer to showerhead gap is 2 cm. The annular pump port extends from the focus ring to the outer metal wall. The secondary emission coefficient by ion bombardment on all surfaces is  $\gamma = 0.15$ . The notation used to describe these voltages are:  $V_{rf}$  is rf voltage applied to the substrate,  $V_{rf0}$  is the self dc bias on the rf electrode and  $V_{dc}$  is the dc bias applied to the upper electrode.

The base case operating conditions are Ar/C<sub>4</sub>F<sub>8</sub>/O<sub>2</sub>=80/15/5 at 40 mTorr with a flow rate of 300 sccm. The substrate is powered at 1 kW ( $V_{rf} = 650$  V,  $V_{rf0} = -115$  V) and the dc electrode delivers 200 W ( $V_{dc} = -370$  V). The rf cycle averaged electron density, total positive ion density and power deposition density are shown in Fig. 4.2. Both the electron density and total ion density have edge-peaked distributions, partly a result of the low frequency being largely electrostatically coupled with electric field enhancement at the edge of the Si ring. The low aspect ratio of the reactor could also lead to this edged peak in ion density. The electron density has a maximum value of  $1.5 \times 10^{10}$  cm<sup>-3</sup> and the positive ion density has a maximum value of  $4.2 \times 10^{11}$  cm<sup>-3</sup> producing an electronegativity of about 30. The power deposition along the surface of both electrodes is also edge peaked with a maximum value of 5.2 W-cm<sup>-3</sup>. In this narrow gap CCP the sheaths occupy near 20% of the gap width, a condition exacerbated by the additional sheath thickness attributable to the dc bias.

The energy and angular distributions (EADs) of all ions and HEEs incident onto the wafer are shown in Fig. 4.3. Note that the energy distributions for HEEs are only for those electrons that originate from secondary emission from any surface, as described in

Chapter 3. The plasma potential at different times during the rf cycle is shown in Fig. 4.4. As discussed in Part I, ion fluxes incident onto the dc and rf electrodes produce secondary electrons which are accelerated, nearly collisionlessly, into the plasma by the dc and rf sheaths. The majority of HEE incident onto the wafer originate by secondary emission from the dc electrode. Since the time to cross the gap for the HEEs from the dc electrode is short compared to the rf period, the range of the energies of the HEEs reflects the instantaneous difference between the sheath potential on the dc and rf sides of the reactor during the rf cycle. As shown in Fig. 4.4, electrons emitted at the peak of the anodic part rf cycle gain the full dc and rf potentials (diminished by the dc bias on the substrate) as the plasma potential is raised to its theoretical maximum value,  $\varepsilon_{max} = -V_{dc} + V_{rf} + V_{rf0} = 905$  eV. The calculated HEE flux has a maximum energy of  $\varepsilon_{max} = 882$  eV. Secondary electrons emitted from the dc electrode during the cathodic part of the rf cycle could be trapped in the plasma. These electrons do not gain enough energy in the dc sheath to climb the negative potential of the rf sheath. About 30% of the HEEs striking the wafer originate from secondary emission from the wafer, though these electrons tend to be at energies <100-150 eV, as discussed in Part I.

With 1 kW of bias power, the majority of ions are incident on the wafer with energies of 200 and 450 eV, with an angular spread of  $\pm 8^\circ$  as shown in Fig. 4.3b. In comparison, the HEE flux has an angular spread of  $\pm 0.5^\circ$  (also shown in Fig. 4.3b). The total positive ion flux (at  $r = 5$  cm) is  $5 \times 10^{15} \text{ cm}^{-2}\text{s}^{-1}$  and the HEE flux is  $1 \times 10^{15} \text{ cm}^{-2}\text{s}^{-1}$ , yielding a thermal electron flux of  $4 \times 10^{15} \text{ cm}^{-2}\text{s}^{-1}$ .

Compare to rf 2 MHz applied in most commercial etch tools, especially at high

bias power (e.g. 4 kW), 10 MHz bias generates narrower sheaths with lower voltages and higher plasma surface densities. When the bias power is low (e.g. 1 kW), plasma properties at these two rf frequencies do not differ much. In the following discussions we applied rf 10 MHz at 4 kW to investigate dc voltage effects on generation of HEEs and elimination of twisting. These tests could also be conducted at lower rf frequency and lower bias power. Both conditions will, we believe, lead to similar trends as long as the ratio of HEE flux over total ion flux remains unchanged.

### **4.3 Effect of Charging and HEE fluxes on Profiles of HAR Features**

To investigate the effects of charging on twisting of SiO<sub>2</sub> features, 41 identical trenches were simulated with different random seeds for each process starting condition. Here we used dome-shaped photoresist to imitate the ones in experiments. More detailed investigation on the consequences of photoresist shape, type, and thickness etc. during HARC etching will be discussed in the future. The use of different random number seeds in the calculation provides a different sequence of particles (i.e., identity, energy and angle) randomly selected from the same EADs provided by the HPEM. This also produces a different sequence of randomly chosen reactions of gas phase particles with the surface. This procedure emulates a set of adjacent side-to-side features which randomly receive different fluxes. We confirmed this by simulating a number of cases having 6 side-by-side features in the same mesh. There were few, though discernable, feature-on-feature effects. (Computationally, it is faster to simulate six cases each having a single trench in the mesh than six trenches in a single mesh.) The mask opening is 75 nm wide with a depth of 1500 nm to a Si stop layer, yielding an aspect ratio of  $AR = 20$ . The photoresist (PR) is initially dome-shaped with a maximum thickness of 450 nm. For incident ion en-

ergies  $< 1.3$  keV, polymer deposition effectively stops etching at the Si layer.

A selection of trenches for a substrate power of 4 kW is shown in Fig. 4.5. These profiles are a subset of all cases that were run. They were chosen to provide representative, and in some cases extreme, samples of features and do not necessarily represent the average. Profiles are shown in Fig. 4.5a without considering charge deposition and so ignore the consequences of electric field deflections on ion trajectories. The majority of profiles are straight – only 5 trenches of 41 displayed twisting, or about 12%. Note that the straight features have different etch rates. Even for a uniform flux of reactants on the wafer scale, due to the small opening to the feature, there are statistical variations in the order, identity, and energy of particles entering adjacent trenches. For ion fluxes of  $10^{16}$   $\text{cm}^{-2}\text{s}^{-1}$ , the interval between ions entering a circular via is about 1  $\mu\text{s}$ . The statistical nature of the incident fluxes is even more pronounced for ions in the high energy tail of the IEAD which already has a small population. These are the ions which are most responsible for activating etch processes. The end result is a feature-to-feature difference in etch rate.

The cause for the occasional twisting and the variation in etch rate for this process may have two components - the statistical variation in the sequence of particles and the statistical variation in ion energies. The more rapid buildup of polymer or more etching on one side of the trench due to statistical variation in fluxes and reaction rates can slow the etch rate on that side of the trench and produce an asymmetric profile. Since few ions reach the bottom of the trench without neutralizing grazing collisions off the sidewalls, once a feature begins to twist, it tends to be self-perpetuating. This randomness of the polymer deposition can also contribute to variations in etch rates.

To provide insights to how much of the twisting and variation etch rates is due to randomness in polymer deposition and how much is due to randomness in ion energies, the etching of Si trenches in Ar/Cl<sub>2</sub> gas mixtures was simulated. The same initial profile and aspect ratio as those of the SiO<sub>2</sub> features were used and, again, charging was not considered. The mechanism for etching of Si using Ar/Cl<sub>2</sub> plasmas is by passivation of Si by Cl atoms forming SiCl<sub>x</sub> ( $x \leq 3$ ) surface species, followed by ion activated etching to evolve gas phase SiCl<sub>x</sub> [23,24]. There is typically no significant polymer deposition. These processes have been included in a reaction mechanism in our feature profile model, as discussed in Ref. [25].

Examples of Si profiles etched in Ar/Cl<sub>2</sub> plasmas are shown in Fig. 4.5b. The flux of Cl atoms ( $1.4 \times 10^{18} \text{ cm}^{-2}\text{s}^{-1}$ ) greatly exceeds that of ions ( $3.5 \times 10^{16} \text{ cm}^{-2}\text{s}^{-1}$ ) and so statistical variations in fluxes (and their energies and angles) can be attributed dominantly to the ions. No significant twisting is predicted but there are feature-to-feature variations in etch rates. We attribute these differences to the statistical variation in the flux and energy of ions incident into adjacent features. We can therefore conclude that even in the absence of charging, the statistical nature of incident species in highly polymerizing processes can produce some small amount of twisting. Feature-to-feature variations in etch rates, even for non-polymerizing chemistries, can occur due to the randomness in the magnitudes, energies and angles of the ion fluxes.

When including charging in the SiO<sub>2</sub> etch process, the incidence and severity of twisting are both increased, as shown in Fig. 4.5c. In these cases, the HEE flux was not included and so the only electron flux incident onto the features is that from the thermal electrons having a temperature of about 2 eV. The incidence of twisting increased from

5/41 (or 12%) without charging to 20/41 (or about 49%) with charging. The increase in twisting largely results from there being immobile charge deposited on the sidewalls which creates lateral electric fields which deflect the ions. (See discussion below.) The effect is exacerbated by the trapping of charge in the polymer layers where charge is deposited over. Given a non-conducting polymer (as is the case here) there is no way to dissipate the charge in the absence of sputtering away the overlying polymer. Since the removal rate of polymer on the side wall is slow as ion trajectories are grazing (with low sputtering rates), the trapped charge persists. In a sense, the trapped charges act as sentinels which produce persistent electric fields which perpetuate the twisting. For a conductive polymer, most of the charges can still accumulate at the interface between the polymer and SiO<sub>2</sub> since the conductivity of SiO<sub>2</sub> is pretty low. We simulated etching of the same trenches as above with highly conductive polymer layers ( $\sigma \sim 0.01 \text{ S/cm}$ ), in which we still found a twisting frequency of  $\sim 38\%$ . If the polymer is non-conductive while SiO<sub>2</sub> is highly conductive (similar to Si,  $\sigma \sim 0.01 \text{ S/cm}$ ), twisting frequency is reduced to  $\sim 25\%$ . Since the polymer layer is very thin due to highly energetic ion bombardment, large amount of charges trapped in the polymer layer may dissipate through the conductive bulk SiO<sub>2</sub>. If both polymer and SiO<sub>2</sub> are conductive ( $\sigma \sim 0.01 \text{ S/cm}$ ), charges only have very small effects on incident ion trajectories due to their fast drift velocities in the solid. In this case the twisting frequency is comparable to that of non-charge trench etching.

One of the intents of the dc-augmentation of the CCP reactor is to produce HEE fluxes with a narrow angular spread that are able to penetrate into features to neutralize positive charge. For example, EADs for all ions and HEE fluxes for dc voltages of  $V_{dc} =$

0 to -1000 V are shown in Fig. 4.6. Instead of adjusting the rf voltage to maintain a constant power, the rf voltage was kept constant to minimize the change in the IEADs and so minimize its influence on the evolution of feature profiles. We did, however, allow  $V_{rf0}$  to vary so that the charging of surfaces would be self-consistently accounted for. So in spite of holding  $V_{rf}$  constant, the IEADs vary slightly in energy as  $V_{dc}$  increases due to the variation in  $V_{rf0}$ , though these small changes are not particularly significant. The narrowing in angle of the IEADs with increasing (more negative)  $V_{dc}$  results from an increase in plasma density and narrowing of the sheath produced by the ionization from secondary electrons accelerated by the dc bias.

The range of the EADs of the HEE generally reflects the instantaneous difference between the sheath potential on the dc and rf sides of the reactor during the rf cycle. (Recall that that these distributions are only for electrons and their progeny that result from secondary electron emission.) The maximum energies for electrons emitted from the dc electrode generally obey the scaling law  $\varepsilon_{max} = -V_{dc} + V_{rf} + V_{rf0}$  with values of 1270 to 2200 eV for  $V_{dc} = 0$  to -1000 V. Note the HEE beams that are naturally produced due to the oscillation of the plasma potential even with  $V_{dc} = 0$  V. The additional use of dc augmentation is meant to control the extent of the energy and the magnitude of the flux of these secondary electrons.

The magnitude of the fluxes of HEEs and the fraction of the HEE flux compared to the ion flux are also shown in Fig. 4.6 as a function of  $V_{dc}$ . The magnitude of the HEE flux increases from  $1.2 \times 10^{15} \text{ cm}^{-2}\text{s}^{-1}$  to  $5.5 \times 10^{15} \text{ cm}^{-2}\text{s}^{-1}$  for  $V_{dc} = 0$  to -1000 V. This represents 9.5% to 58% of the total ion flux. There is a commensurate decrease in the thermal electron flux which charges the top of the feature, and an increase in the dc cur-

rent which flows to the side walls. (See Chapter 3 for a discussion of the disposition of dc current.)

Profiles obtained when including HEE fluxes when including charging in the feature for  $V_{dc} = 0$  and  $-750$  V are shown in Fig. 4.7. Different random number seeds were used for 41 cases each and representative profiles are shown. The occurrence of twisting for  $V_{dc} = 0$  is 18/41 or 44%, only marginally better than in the absence of HEE fluxes. For  $V_{dc} = -750$  V, the occurrence of twisting is 7/41 or 17%, only slightly higher than in the absence of charging. The HEEs apparently successfully penetrate into the trench and neutralize sufficient positive charge to reduce the production of lateral electric fields by positive ions. In particular, positive charge is neutralized before it is trapped in the polymer by further deposition. The decrease in the incidence of twisting between  $V_{dc} = 0$  and  $-750$  V is attributable to at least two factors – an increase in the electron energy which produces more forward scattering and an increase in the magnitude of the HEE flux (Fig. 4.6c). Between  $V_{dc} = 0$  and  $-750$  V, the electron flux increases from 9.5% to 39% as a fraction of the total ion flux.

Profiles obtained with HEE fluxes and charging for  $V_{dc} = 0, -400, -500,$  and  $-750$  V on are shown in Fig. 4.8 for constant etching times. These are representative features from 41 simulations with different random seeds. Although there is some variation in etch rate, more negative  $V_{dc}$  tends to increase the etch rate. In our reaction mechanism the HEE fluxes do not directly affect surface chemistry by initiating reactions. The higher etch rates likely result from a larger ion flux resulting from the ionization produced by the HEE and the higher energy ions in the feature due to the reduction in the positive potential in the trench by neutralization by the HEE flux. With a smaller intra-

feature electric field, incident ions are in general less impeded in both vertical and lateral directions. The twisting frequency as a function of  $V_{dc}$ , shown in Fig. 4.8c, decreases with increasing (more negative)  $V_{dc}$ , from 44% at  $V_{dc} = 0$  to 10% at  $V_{dc} = -1000$  V.

Time sequences of electric potential distributions as etching proceeds are shown in Fig. 4.9 for otherwise identical cases with different random seeds. One random number seed produced a straight feature while the other random number seed produced twisting. The conditions are  $P_{rf} = 4$  kW and  $V_{dc} = -750$  V. The maximum potential is 100-150 V and occurs roughly half-way down the trench or at an AR = 10. This is approximately the location that the average ion would strike the side wall and deposit charge. Features with smaller aspect ratios where ions strike the bottom of the trench before reflecting off the side walls will have the maximum in potential on the bottom of the feature. The top of the mask charges to only a few volts negative. The maximum positive potential increases with increasing depth as the likelihood for electron penetration into the feature decreases.

When the statistical distribution of charged particles produces a potential that is basically symmetric across the trench, the lateral electric fields are small and there is little off-axis deflection of ions. The end result is a nearly straight feature, as shown in Fig. 4.9a. If the statistical distribution of ions and electrons produces more positive charge and a larger potential on one side of the feature, as shown in Fig. 4.9b, the lateral electric fields are more intense. These fields produce a deflection in the ion trajectory which contributes to twisting. The twisted feature has a larger positive potential, likely a result of positive charge being trapped in the polymer and so is shielded from directly being neutralized by the HEE flux.

Holding the dc bias power constant at 200 W, we investigated the effects of rf bias power on EADs and HEE fluxes. For example, the EADs for HEEs and ions, and HEE fluxes for rf powers of 1 to 4 kW are shown in Fig. 4.10. With increasing rf bias power, the extent in energy and flux increases for both ions and electrons. These increases in energy result from the increase in  $V_{rf}$  (650 V at 1 kW to 1450 V at 4 kW) and  $V_{rf0}$  (-120 V at 1 kW to -220 V at 4 kW). However since the dc current and HEE flux also increase with rf power,  $V_{dc}$  decreases (becomes less negative) to deliver a constant dc power (-370 V at 1 kW to -250 V at 4 kW). The end result is that the increase in  $\varepsilon_{max}$  (470 eV at 1 kW to 1200 eV at 4 kW) scales less than linearly with  $V_{rf}$ . The extent of the EADs is also less than linear with power. The HEE flux as fraction of the ion flux, shown in Fig. 4.10c, does not significantly change as a function of  $V_{rf}$ .

The twisting frequency as a function of rf power is shown in Fig. 4.11 with and without HEE fluxes. The narrowing in angle of the ion flux with rf power increases the penetration of positive charge deeper into the feature prior to the ion fluxes being neutralized by colliding with the side walls. The increase in ion energy offsets the beneficial effects of the neutralizing HEE flux. Although there is a decrease in the twisting frequency with increasing HEE fluxes, the end result is that the twisting frequency increases with increasing rf power.

#### 4.4 Concluding Remarks

Charging effects on profile evolution have been computationally investigated for HAR SiO<sub>2</sub> features etched in a dc-CCP reactor capable of producing HEE fluxes onto the wafer. Twisting and variations in etch rates were predicted, effects attributed to the stochastic fluxes of reactants into the small features. In the absence of charging, a small in-

cidence of twisting was observed in polymerizing processes due to the random deposition of polymer or random etching on the side walls. Twisting was not observed in non-polymerizing chemistries although there was a variation in etch rate due to the stochastic arrival of high energy ions. When including charging but without HEE fluxes, the incidence of twisting increased due to the stochastic production of lateral electric fields inside the feature which deflects ions. The effect is amplified by charge that is trapped in the polymer on the side walls. Highly conductive polymer layer may reduce twisting frequency during etching. Consequences of ion bombardment and UV exposure on inducing polymer conductivity and elimination of twisting will be investigated in the future. When including HEE fluxes, the incidence of twisting was reduced to nearly that in the absence of charging, an affect attributed to the HEE beams neutralizing positive charge deep in the trench. Increasing  $V_{dc}$  while the IEADs remain nearly constant increases the HEE flux and the maximum electron energy, both of which reduce the incidence of twisting. Increasing rf bias power generally increases the incidence of twisting by narrowing the angular spread and increasing the energy of the ion flux. Both enable deeper penetration of ions into the feature before undergoing neutralizing collisions.

## 4.5 Figures

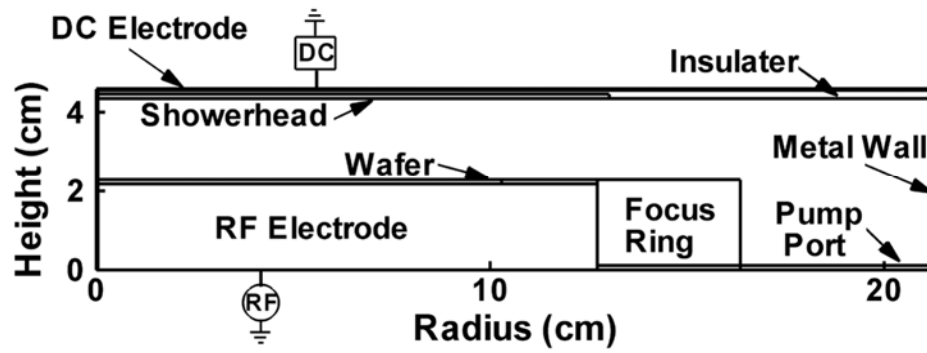
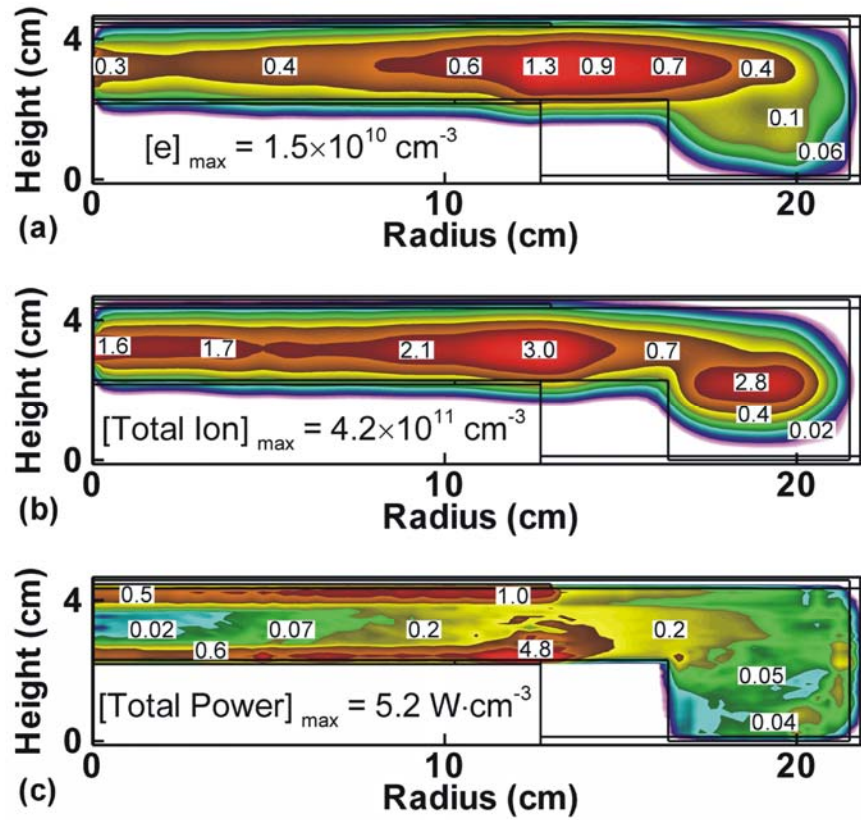
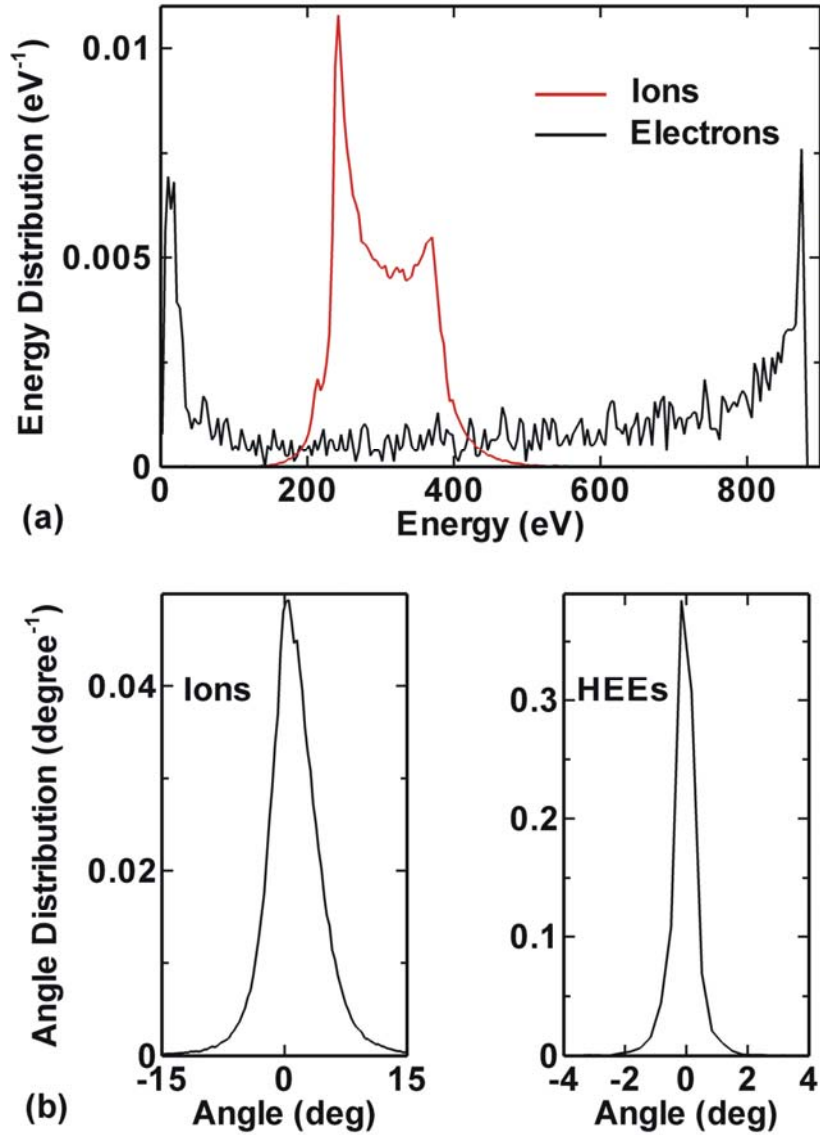


Fig. 4.1 Schematic of a dc augmented, cylindrically symmetric single frequency CCP reactor.



**Fig. 4.2** Bulk plasma properties for the base case ( $\text{Ar}/\text{C}_4\text{F}_8/\text{O}_2 = 80/15/5$ , 40 mTorr, 300 sccm,  $P_{rf} = 1$  kW at 10 MHz,  $P_{dc} = 200$  W). (a) Electron density, (b) total ion density and (c) power deposition.



**Fig. 4.3** Energy and angular distributions summed for all ions and HEEs incident onto the wafer for the base case (a) Energy distributions and (b) angular distributions.

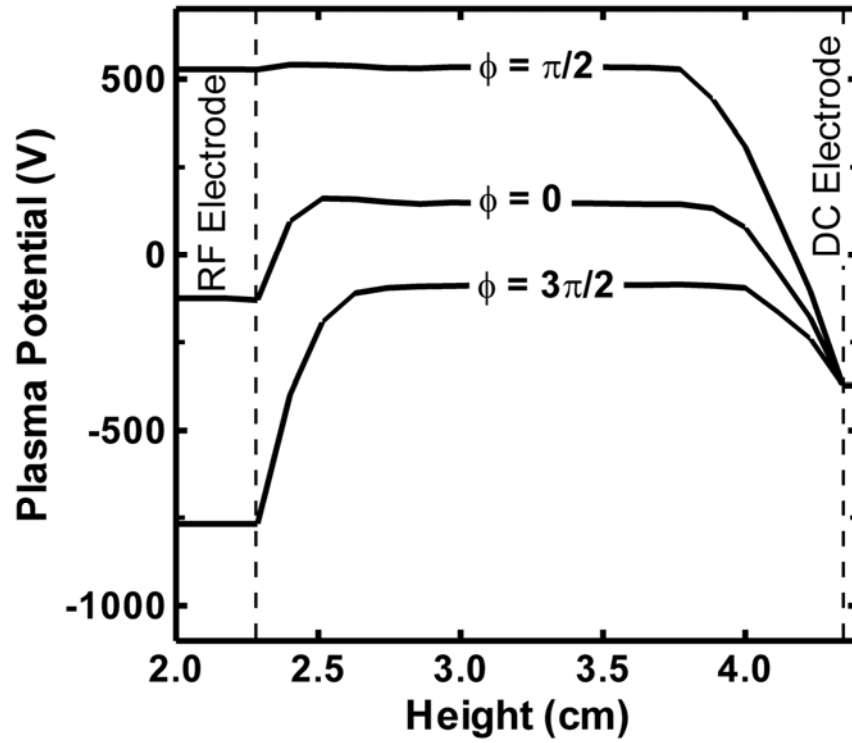
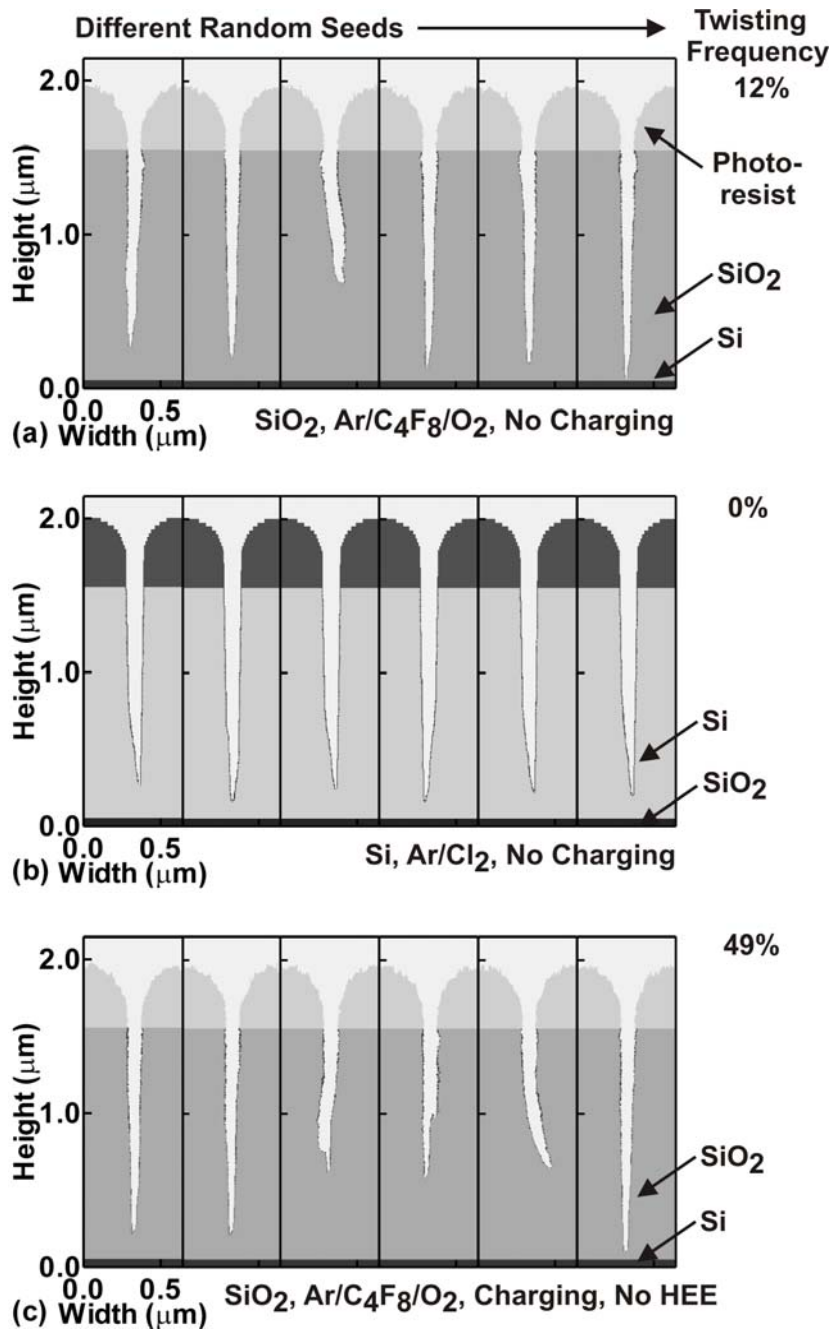
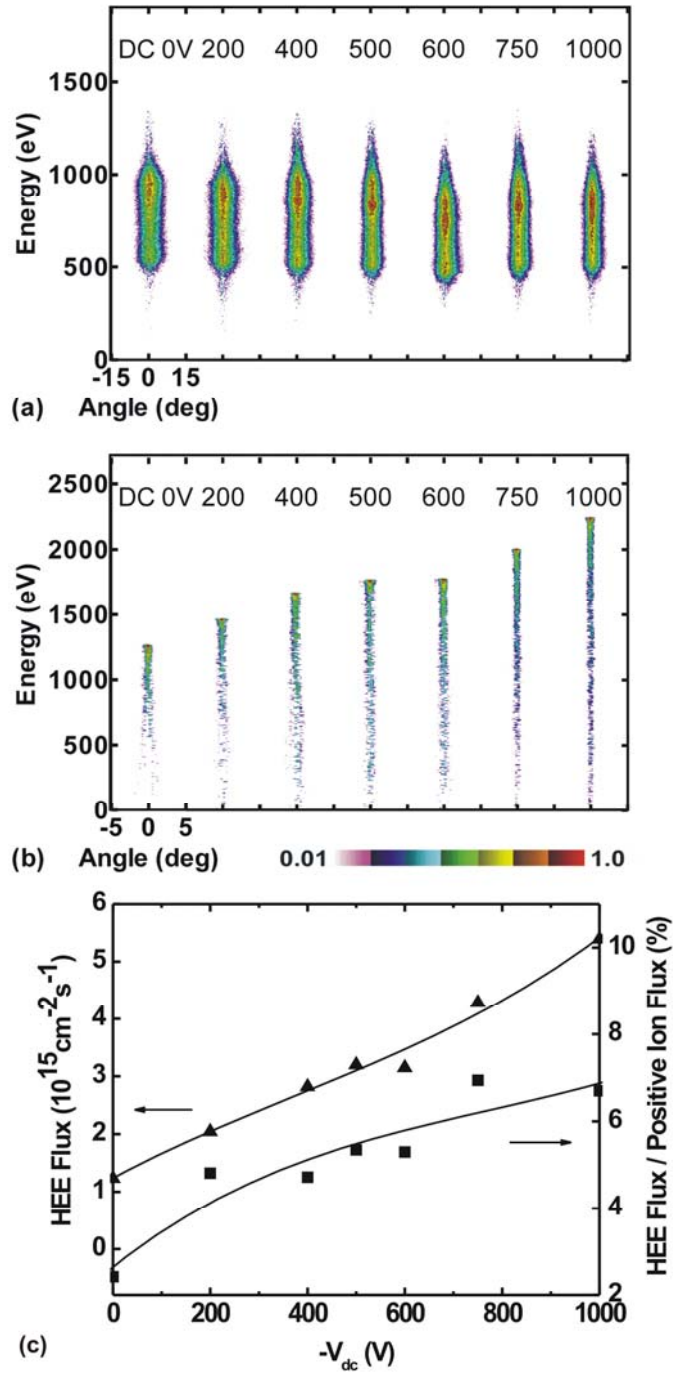


Fig. 4.4 Plasma potential as a function of chamber height and phase for the base case.



**Fig. 4.5** Profiles selected from 41 otherwise identical simulations except for using different random number seeds. The reactor conditions are the base case except for the rf power being 4 kW. (a) Fluorocarbon plasma etching of  $\text{SiO}_2$  without including charging. (b) Ar/ $\text{Cl}_2$  plasma etching of Si without including charging. (c) Fluorocarbon plasma etching of  $\text{SiO}_2$  including charging but no HEE fluxes.



**Fig. 4.6** HEE and ion characteristics as a function of  $V_{dc}$ .  $V_{rf}$  was held constant at 1500 V while  $V_{rf0}$  was allowed to seek its self consistent value. (a) IEADs, (b) EADs of the HEE fluxes and (c) HEE flux and fraction of HEE flux with respect to the positive ion flux.

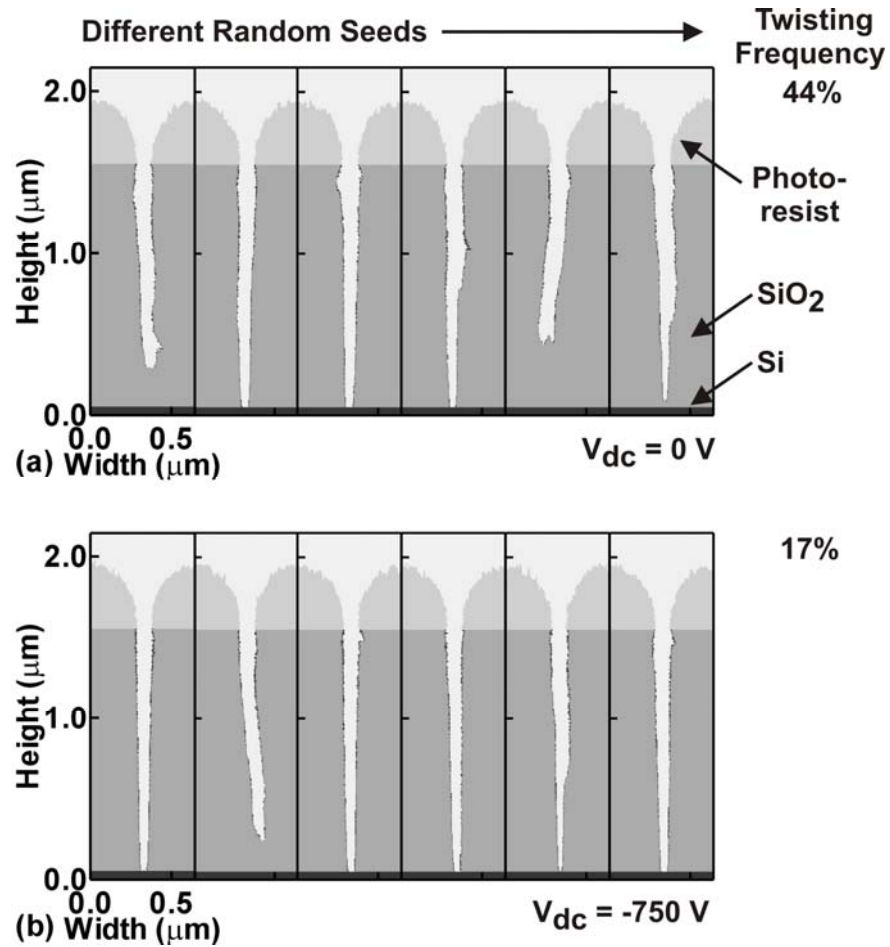


**Fig. 4.7** Profiles of otherwise identical trenches for fluorocarbon plasma etching of SiO<sub>2</sub> over Si chosen from 41 trials with different random number seeds when including charging and HEE fluxes. (a)  $V_{dc} = 0$  and (b)  $V_{dc} = -750$  V.

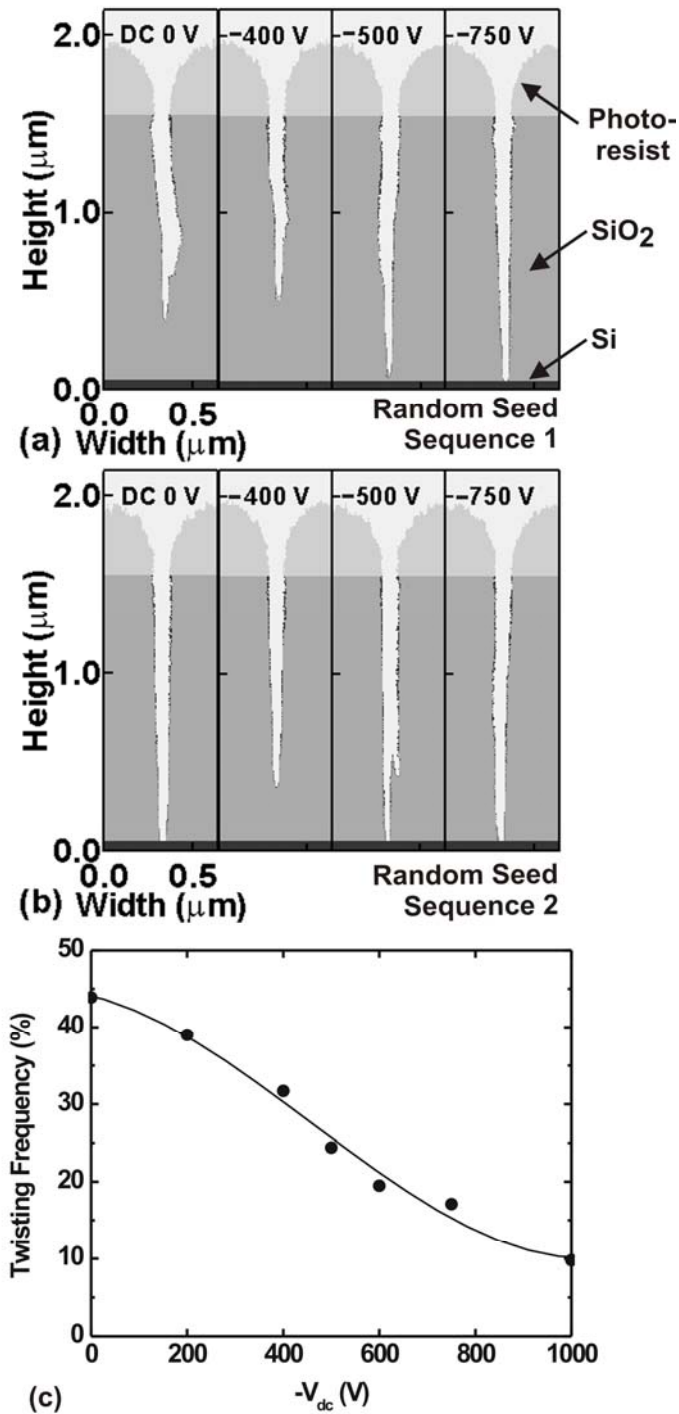
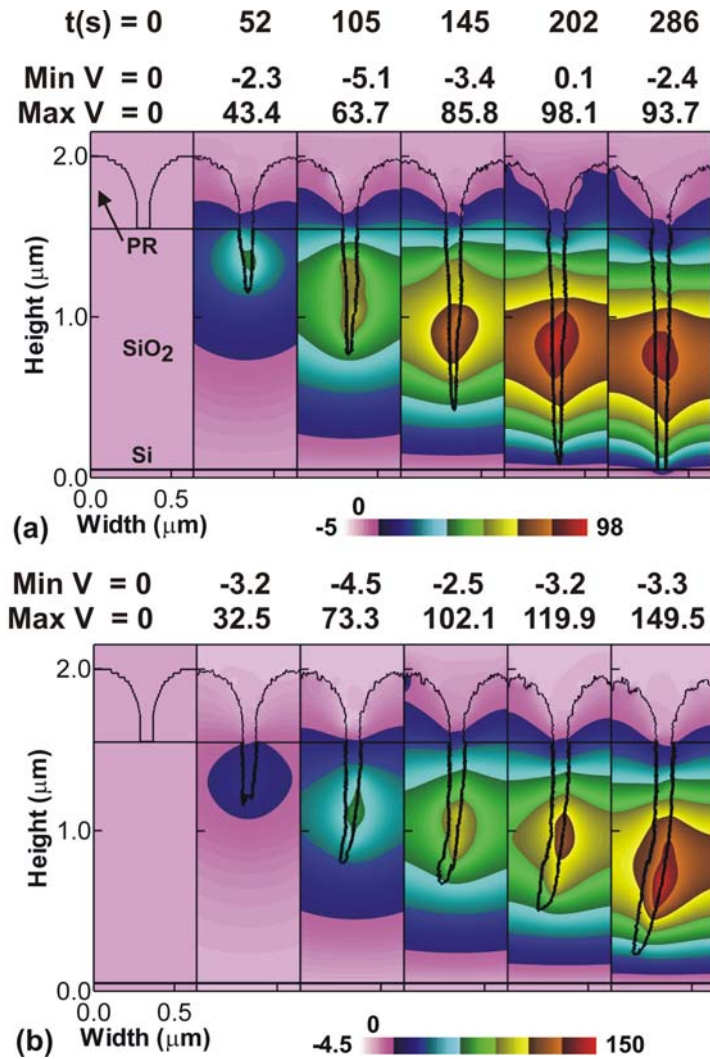
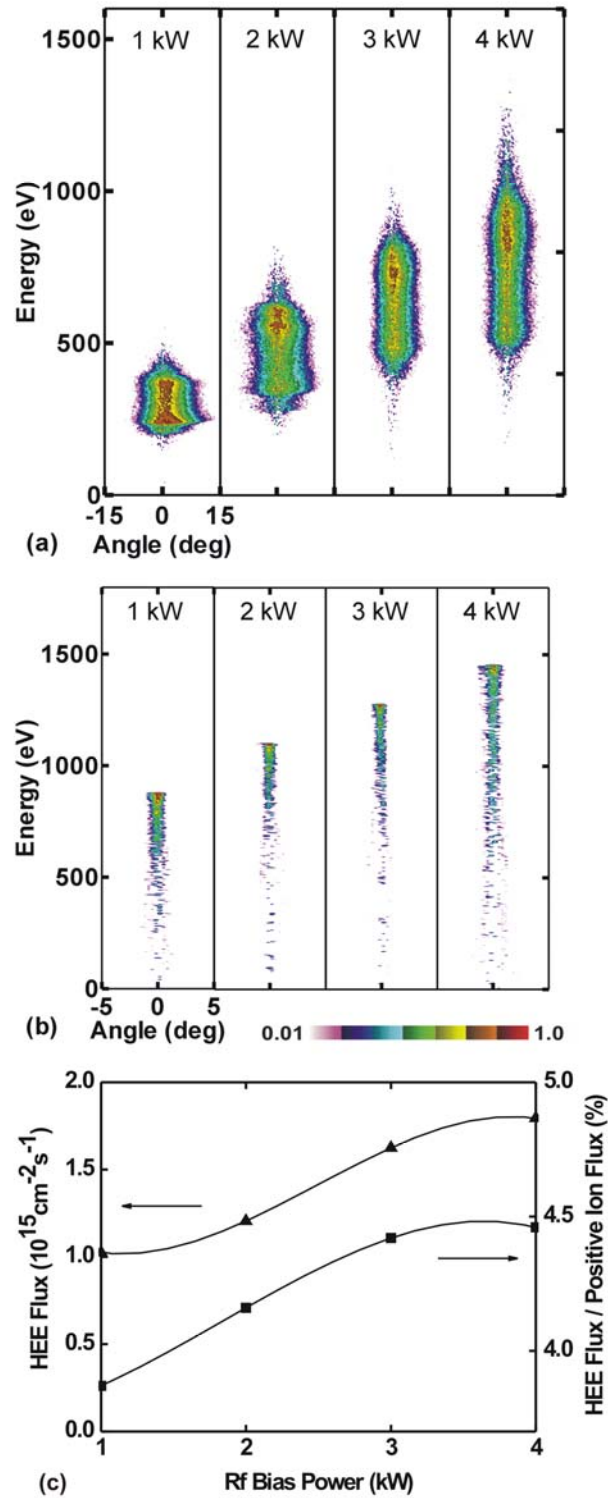


Fig. 4.8 Profiles and twisting frequency as a function of  $V_{dc}$ . (a) Profiles for different values of  $V_{dc}$  of otherwise identical trenches for fluorocarbon plasma etching of  $\text{SiO}_2$  over Si chosen from 41 trials. (b) Same as in (a) except for different random number seeds. (c) Twisting frequency as a function of  $V_{dc}$ .



**Fig. 4.9** Time sequence of potential distributions in features as etching proceeds differing only in the choice of random number seeds. (a) Straight trench and (b) twisted trench.



**Fig. 4.10** Consequences of rf bias power while keeping the dc power constant. (a) IEADs for  $P_{rf} = 1 - 4$  kW, (b) EADs for the HEE flux and (c) HEE flux and fraction of HEE flux with respect to the positive ion flux as a function of  $P_{rf}$ .

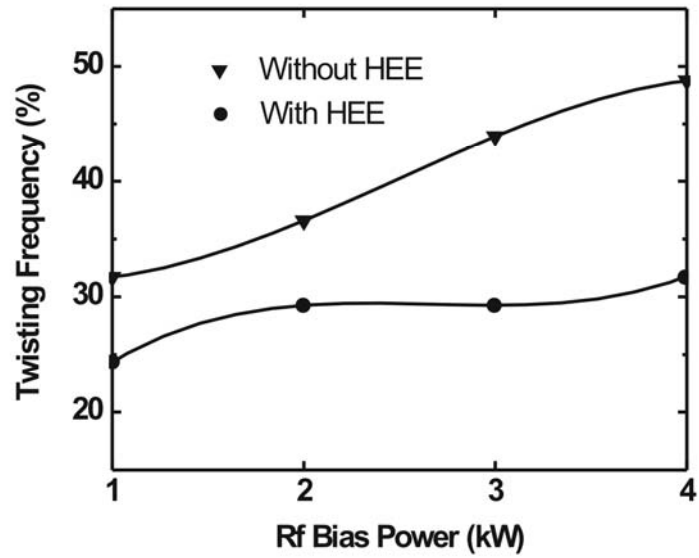


**Fig. 4.11** Twisting probability as a function of rf bias power with and without HEE fluxes for  $P_{dc} = 200$  W.

#### 4.6 References

1. S. Welch, K. Keswick, P. Stout, J. Kim, W. Lee, C. Ying, K. Doan, H.S. Kim and B. Pu, *Semiconductor Int.* **32**, 18 (2009).
2. N. Ikegami, A. Yabata, T. Matsui, J. Kanamori and Y. Horiike. *Japn. J. Appl. Phys.* **36**, 2470 (1997).
3. D. Kim E. A. Hudson, D. Cooperberg, E. Edelberg, and Mukund Srinivasan, *Thin Solid Films* **515**, 4874 (2007).
4. H. S. Park, S. J. Kim, Y. Q. Wu, and J. K. Lee., *IEEE T. Plasma Sci.* **31**, 703 (2003).
5. A. C. Westerheim, A. H. Labun, J. H. Dubash, J. C. Arnold, H. H. Sawin, and V. Yu-Wang, *J. Vac. Sci. Technol. A* **13**, 853 (1995).
6. M. Schaepkens, G. S. Oehrlein and J. M. Cook, *J. Vac. Sci. Technol. B* **18**, 856 (2000).
7. J. Bing, E. A. Edelberg and T. Yanagawa, US Patent Application 2008/0119055, 2008.
8. J. C. Arnold and H. H. Sawin, *J. Appl. Phys.* **70**, 5314 (1991).
9. S. Samukawa, *Appl. Phys. Lett.* **64**, 3398 (1994).
10. G. S. Hwang and K. P. Giapis, *Appl. Phys. Lett.* **71**, 2928 (1997).
11. K. P. Giapis, G. S. Huang, and O. Joubert, *Microelectronic Eng.* **61-62**, 835 (2002).
12. T. G. Madziwa-Nussinov, D. Arnush, and F. F.Chen, *Phys. Plasmas*, **15**, 013503 (2008).
13. D. J. Economou, *J. Phys. D.* **41**, 024001 (2008).
14. A. Ranjan, V. M. Donnelly and D. J. Economou, *J. Vac. Sci. Technol. A* **24**, 1839 (2006).

15. A. Ranjan, C. Helmbrecht, V. M. Donnelly, D. J. Economou and G. Franz, *J. Vac. Sci. Technol. B* **25**, 258 (2007).
16. T. Shimmura, Y. Suzuki, S. Soda et al, *J. Vac. Sci. Technol. A* **22**, 433 (2004).
17. G. S. Sandhu, M. F. Hineman, D. A. Steckert, J. Bai, S. J. Trapp, and T. Schrock, US Patent Application 2008/0128389, 2008.
18. T. Ohmori, T. Goto and T. Makabe, *J. Phys. D: Appl. Phys.* **37**, 2223 (2004).
19. T. Ohmori and T. Makabe, *Appl. Surf. Sci.* **254**, 3696 (2007).
20. E. Kawamura, A. J. Lichtenberg and M. A. Lieberman, *Plasma Sources Sci. Technol.* **17**, 045002 (2008).
21. K. Depoh and P. L. G. Ventzek, *J. Vac. Sci. Technol. A* **26**, 1415 (2008).
22. L. Xu, L. Chen, M. Funk, A. Ranjan, M. Hummel, R. Bravenec, R. Sundararajan, D. J. Economou, and V. M. Donnelly, *Appl. Phys. Lett.* **93**, 261502 (2008).
23. V. M. Donnelly, *J. Appl. Phys.* **79**, 9353 (1996).
24. J. P. Chang, J. C. Arnold, G. C. H. Zau et al. *J. Vac. Sci. Technol. A* **15**, 1853 (1997).
25. R. J. Hoekstra, M. J. Grapperhaus, and M. J. Kushner, *J. Vac. Sci. Technol. A* **15**, 1913 (1997).

## 5. MODELING OF IMPLANTATION AND MIXING DAMAGE DURING ETCHING OF $\text{SiO}_2$ OVER SI IN FLUOROCARBON PLASMAS

### 5.1 Introduction

In plasma etching, ion-activated chemical processes preferentially etch one material with respect to another and so lead to selectivity [1]. In many etch processes, polymer layers produced by the plasma contribute to this selectivity by being less reactive on certain surfaces. A thicker polymer layer forms on those materials which then requires ions to penetrate the polymer to activate the etch of the underlying material [2]. This below-polymer etching typically requires higher energy ions. Higher energy ions also tend to be more anisotropic and so better able to maintain critical dimensions (CD) [3]. An example of this process is fluorocarbon plasma etching of trenches and vias in  $\text{SiO}_2$  and stopping on a crystalline Si layer. The fluorocarbon radicals produced in the plasma deposit a polymer layer on the  $\text{SiO}_2$  which is partially consumed during the etching process, thereby thinning the layer. Lack of consumption of the polymer by etching of the Si results in a thicker polymer layer on the Si.

When etching through the  $\text{SiO}_2$  is nearly complete and the Si is exposed, there is often a significant over-etch period required. (The over-etch is the additional etching time required to clear the corners of the feature after the center of the feature has reached the underlying material.) At this time, selectivity of etching (that is, lack of etching of the Si) is maintained by a  $\text{C}_x\text{F}_y$  polymer layer of a few nm. The high energy ions that are required to activate etching through the overlying polymer are also capable of penetrating

the polymer and damaging the underlying Si. This damage often takes the form of an amorphized mixed-layer wherein the original Si atoms are both mixed with other Si atoms and with etchant or polymer atoms. High energy ions from the plasma can also implant into the Si, causing damage along their trajectory.

This damage is particularly problematic in high aspect ratio (HAR) etching of Si and SiO<sub>2</sub> in fluorocarbon plasmas [4]. To maintain the CD of these features to aspect ratios (AR) of 10-30, high energy ions (hundreds of eV to greater than 1 keV) are required. These high energy ions are more anisotropic with a narrower angular distribution, qualities required to enable reaching the bottom of the feature with sufficient energy to activate the etch. Even with their higher initial energy and narrow angular spread, the ions do suffer glancing collisions on the sidewalls of the feature. The higher the AR and the more glancing collisions that occur, the more tapered the feature tends to be, thereby requiring significant over-etching by high energy ions to clear the bottom of the feature. As the Si layer is exposed during the over-etch, ion bombardment causes mixing of etchant species (e.g., C<sub>x</sub>F<sub>y</sub>) into the Si and amorphizing the Si lattice [5].

As the ion energy increases, in addition to activating etching of the material underlying the polymer and mixing the surface layers, small ions can penetrate through the passivation layer and implant into the underlying material [6]. Molecular ions tend to dissociate upon striking the surface and so typically only atomic ions penetrate beneath the surface. (When ions come within a few angstroms of the surface, they usually neutralize through an Auger process and strike the surface as a neutral. In this paper, we will refer to the particles approaching and penetrating into the solid as ions.) Although mix-

ing of lattice atoms with etchant species occurs only in the top few nm of the surface, implantation can occur deeper below the surface. In the case of Si, these implantation processes both disrupt the crystal structure and contribute to producing a mixed layer. In the case of SiO<sub>2</sub>, the material is already amorphous and so disruption of the crystal structure is not an issue – however formation of the mixing layer is. Optimizing these processes is then a compromise between having a high etch rate and maintaining CD with a high bias and high ion energies, and minimizing damage and mixing in the underlying material by having low ion energies.

Defect formation (e.g., vacancies, interstitials, implanted particles) in Si resulting from energetic ion bombardment (1 keV ~ 1 MeV) has been investigated in detail in the context of etching (10's eV ~ 1 keV) and ion-implantation (several to hundreds keV) [7-17]. Characteristics of the amorphous layer produced by ions on Si surfaces have been studied in experiments [10-11] and in molecular dynamics (MD) simulations [12-15]. The sputtering yield and amorphous layer thickness have been characterized as a function of incident ion energy and angle [16,17].

The simulation of ion implantation and mixing in crystals for ions of moderate energy (< a few keV) is best addressed using MD simulations [12-15]. Although precise and first principles, MD simulations are computationally intensive. It is sometimes difficult to perform MD of etching of larger structures, such as full HAR features, rapidly enough to be compatible with CAD (computer-aided-design) tools used in industry. As such, it would be expedient to have a mechanism to address mixing and implantation in conventional feature profile models that are compatible with simulating full features and

that can be incorporated into CAD tools. Such modeling techniques using Monte Carlo simulations have been discussed by Ono et al. [18,19] and Moroz [20]. In this regard, Shimada et al used a level-set-method to simulate etching through multiple layers (e.g., polymer and mix-layer, SiO<sub>2</sub>) [21].

With this goal in mind, we have developed implantation and mixing algorithms for a Monte Carlo (MC) based feature profile model. We then used the model to investigate implantation and mixing during plasma etching of HAR features through SiO<sub>2</sub> to an underlying Si layer in dc augmented, capacitively coupled plasmas (CCPs) sustained in Ar/C<sub>4</sub>F<sub>8</sub>/O<sub>2</sub> gas mixtures [3]. Results are first discussed for tailored ion fluxes incident on blank Si wafers for the purposes of validation of the model and scaling studies. We then discuss damage of underlying Si during etching of HAR trenches in SiO<sub>2</sub> using fluxes from the simulated CCP reactor.

## 5.2 IEADs Onto the Wafer

In Ar/C<sub>4</sub>F<sub>8</sub>/O<sub>2</sub> plasmas, the dominant small ions (and their hot atom counterparts) are Ar<sup>+</sup>, F<sup>+</sup>, C<sup>+</sup>, Si<sup>+</sup>, and O<sup>+</sup>. The stopping ranges of these particles in PMMA/PR, PTFE/polymer, Si and SiO<sub>2</sub> were calculated using SRIM and are shown in Fig. 5.1 as a function of the incident particle energy. The penetration depth increases proportionally with ion energy. For a given energy, the penetration distances for materials rank, long to short: PR > SiO<sub>2</sub> > Si > Polymer. For ions in the same material, the ranking of penetration depth is: C<sup>+</sup> > O<sup>+</sup> > F<sup>+</sup> > Si<sup>+</sup> > Ar<sup>+</sup>. The penetration depths range up to 200 Å at 3,000 eV which covers the expected range of ion energies incident onto the wafer in our plasmas.

Ar/C<sub>4</sub>F<sub>8</sub>/O<sub>2</sub> plasmas were simulated in a dc augmented CCP reactor with the HPEM using the same geometry as in Ref. [3]. The base case operating conditions are Ar/C<sub>4</sub>F<sub>8</sub>/O<sub>2</sub> = 80/15/5 at 40 mTorr with a flow rate of 300 sccm (standard cubic centimeter per minute at STP). The substrate is biased at 10 MHz delivering a power of 4 kW and the dc electrode delivers 200 W.

From the PCMCM we obtained IEADs for Ar<sup>+</sup>, F<sup>+</sup>, and O<sup>+</sup> as shown in Fig. 5.2 as a function of rf bias power. The ion fluxes at the center of the substrate are shown in Fig. 5.3. The rf amplitudes  $V_{rf}$  and dc biases  $V_{dc}$  for these cases are: 1 kW: ( $V_{rf} = -617$  V,  $V_{dc} = -114$  V), 2 kW ( $V_{rf} = -894$  V,  $V_{dc} = -155$  V), 3 kW ( $V_{rf} = -1215$  V,  $V_{dc} = -203$  V) and 4 kW ( $V_{rf} = -1500$  V,  $V_{dc} = -229$  V). The power is specified in the model and the rf voltage is adjusted to obtain this power. Although C<sup>+</sup> and Si<sup>+</sup> are included in the model, they will not be discussed further here due to their low fluxes onto the surface (smaller by a factor of  $10^3 - 10^5$  compared to the major ions). The peak energies of the ions increase nearly linearly with increasing rf bias power for all particles. The heavier ions have narrower angular spreads, consistent with their longer crossing times across the sheaths [22]. At higher bias power, the IEADs are narrower in angle due to the stronger sheath electric fields orienting the ions more towards the vertical.

### 5.3 Validation of the Model

For purposes of validation, Ar<sup>+</sup> bombardment of Si was modeled using a mesh resolution of 3 Å with each mesh cell approximately representing 1 atom. Profiles are shown in Fig. 5.4 after 30 s with an ion flux of  $7 \times 10^{14}$  cm<sup>2</sup>s<sup>-1</sup> at normal incidence for ion energies of 20, 50, 100 and 200 eV. (For the purposes of better observing the mixing in

bulk Si, the initial distribution of atoms was color coded red and dark blue in alternating layers, but otherwise they represent the same material. Green squares represent implanted Ar particles.) These energies were chosen to enable comparison with the MD simulation of Humbird, et al.[13] The flux and duration of bombardment of  $\text{Ar}^+$  corresponds to 30 monolayer (ML) of  $\text{Ar}^+$  fluence. Charging effects were not included to better compare the mixing under the same conditions as the MD simulations. The depth of the mixing layer in the simulation is determined by the maximum depth for which there is significant disturbance of the lattice. That is, a single errant particle deeply penetrating will not constitute the mixing depth. The solid curves represent the average mixing depth. And the error bars represent the statistical radial variation of the mixing depth.

At 20 eV, ions penetrate only a few monolayers of Si and little mixing occurs. As the ion energy increases, ions penetrate deeper into the bulk Si and induce more mixing during and after implantation. The amorphous layer thickness as a function of bombardment time is shown in Fig. 5.5. The final mixing layer thickness is about 9 Å at 20 eV to 38 Å at 200 eV, generally in good agreement with the MD simulation (dashed lines) especially at higher ion energy (e.g. 200 eV). The statistical variation in the thickness of the mixing layer is 1-2 Å at 20 eV and increases to 6 Å at 200 eV. We also reproduce the rapid onset of mixing damage (a few s) before reaching a steady state, though we reach that steady state sooner than the MD simulations. The thickness of the mixing layers is close to the ranges calculated from SRIM, though sometimes exceeds these ranges. The ranges are average values from a statistical distribution of stopping distances, and so there are significant numbers of individual particles whose penetration distances is

greater than the ensemble average. We see this effect in the model, individual particles penetrating deep into the material, and the end result is that mixing and damage occurs at depths beyond the ensemble averaged stopping distance.

#### 5.4 Scaling of Implantation and Mixing

In order to investigate the degree of implantation and mixing under etching conditions in an Ar/C<sub>4</sub>F<sub>8</sub>/O<sub>2</sub> CCP, a multi-layer Si structure was used similar to that described above for comparisons with the MD simulations. The top layer is SiO<sub>2</sub> of thickness 9 nm followed by alternating monolayers of Si (3 Å). A thin SiO<sub>2</sub> layer was chosen to represent an actual etch process at the time that SiO<sub>2</sub> is thinned as the Si layer is approached. The fluxes of radicals and ions incident onto the surface are listed in Table I. The fluxes are obtained from the rf 4 kW case ( $V_{rf} = -1500$  V,  $V_{dc} = -229$  V). We first artificially constrained the ion energies to be mono-energetic from 1 eV to 1000 eV but having the same magnitude of fluxes as obtained from the simulation in order to observe general scaling trends.

The resulting etch profiles after processing for 25 seconds are shown in Fig. 5.6. At energies of 1 eV, which are lower than the threshold energy for etching and implanting, only polymer deposition (brown squares) occurs on the surface. When the ion energy is increased to 10 eV, which is marginally higher than the threshold energy for sputtering of C<sub>x</sub>F<sub>y</sub> polymers and implanting while still lower than that of most etching reactions, sputtering of polymer occurs. This produces polymer segments (red) and implanted species (dark blue) on the top of the SiO<sub>2</sub> but there is essentially no etching. At 100 eV, sputtering and etching reactions dominate. More broken polymer segments (red)

are on the surface, to a depth of about 1 nm. Mixing also begins to appear as a result of implantation to a depth of about 2 nm. The surface significantly roughens as micro-masking due to random collections of thicker polymer block ions. The SiO<sub>2</sub> is virtually gone at sites that are not micromasked, with the top layer becoming a mixture of polymer and Si.

Although micro-masking resulting in significant roughening is an experimentally observed effect [23,24], its representation here may be exaggerated due to the discreteness of the Monte Carlo mesh. Polymer deposition on any given site occurs strictly in the vertical direction, as opposed to having a lateral component to the deposition, an effect that is better represented in MD simulations [13]. Although the average polymer layer thickness is well represented in the MC simulation, its roughness is exaggerated due to the need to “stack cells”, which then exaggerates micromasking.

As the ion energies increase to 500 eV and above, deeper implantation occurs with a higher degree of mixing, and etching of Si commences. The polymer rich mixing layer at 1000 eV is about 5 nm while the total mixing layer below the polymer rich layer is about 12 nm thick. At the higher ion energies, Si sputtering and etching also occurs through the thick polymer layer.

Implantation and mixing as a function of RF bias power (1~4 kW) using the actual ion energy distributions and the same test structure as above are shown in Fig. 5.7 after etching for 5 seconds. Etching profiles at the same etch depth for these bias powers are shown in Fig. 5.8. Two cases are shown – with a finite thickness of SiO<sub>2</sub> as might occur as the etch approaches the Si layer and approximately when the Si interface is

reached. As with the monoenergetic ions, the etch proceeds through the top SiO<sub>2</sub> layer and nearly terminates on the underlying Si layer. There is an initial rapid etch through the SiO<sub>2</sub> followed by a slow etch into the Si. Note that there is roughness produced by micro-masking resulting from regions having statistically larger polymer thickness, as discussed above. As the rf power and ion energies increase, there is more mixing of the underlying Si layers below the etched surface. For a constant etch depth, the higher biases statistically have ions which have long ranges through the SiO<sub>2</sub> and which penetrate into the Si. For example, at and above 4 kW, ions penetrate through the remaining SiO<sub>2</sub> produce mixing in the underlying Si to a depth of 5-8 nm even before the etch has reached the Si interface. At a bias of 1 kW, there is negligible penetrate of ions through the remaining SiO<sub>2</sub>. When the etch reaches the Si interface, the mixing depth is 10-12 nm at 4 kW whereas at 2 kW, the depth of mixing is 6 nm. At this point, there is significant mixing even for the 1 kW case.

Even though the peak ion energies scale with bias power, at all bias powers there is a distribution of ion energies, as shown in Fig. 5.2. There is clearly more ion penetration and mixing at the higher bias powers due to the higher range of ion energies. At the same time, a polymer layer persists due to the low energy portion of the ion distribution.

As HAR trenches are etched through SiO<sub>2</sub> to a Si layer below, tapering of the feature results in Si at the center of the feature being exposed to the plasma prior to the sides of the feature. An over-etch is therefore required to clear the feature, which affords greater opportunity for damage to the Si to occur. Mixing of Si at the bottom of HAR trenches etched through SiO<sub>2</sub> was investigated as a function of rf bias power. For exam-

ple, trenches having an aspect ratio of 15 are shown in Fig. 5.9. Profiles are shown for the same etching time 59 s, for bias powers of 1-4 kW. The bottoms of the features are also shown with some over-etching for the different etch times required to clear the bottom of the feature. For comparison of etch selectivity, an etch profile is shown in the absence of implantation mixing or cross-linking at 4 kW after etching for 28 s with a similar etch depth of PR. Implantation and mixing in the Si through the overlying polymer layer produces an amorphous, mixed layer at the bottom of the feature. The higher biases produce more mixing though not to the degree predicted in Fig. 5.7 for a flat surface. The initially larger ion energies are moderated by glancing collisions with the side-walls, thereby reducing their energy by the time they reach the bottom of the feature. As long as these ions have energies exceeding the etching threshold, the feature is cleared. However, the range of these lower energy ions into the underlying material is significantly reduced.

Ion interactions with hydrocarbon PR produce dangling bonds which then cross-link – and the cross-linked polymer surface is then more resistive to etching. As such, there is less degradation of the PR with increasing bias as the PR becomes more resistive through the cross-linking. This enables the CD to be maintained to higher aspect ratios. Although not the focus of this study, the cross linked polymer is shown in Fig. 5.9 as the darkened layer on top of the PR.

Higher bias powers are usually preferred in HAR etching since the etch rate is higher, the feature is straighter and charging effects are minimized due to the higher ion energies and narrower angular distributions. There are, however, drawbacks to etching

with higher ion energies. As shown in Fig. 5.9, higher energy ions cause deeper implantation and more mixing in the underlying Si at the moment that SiO<sub>2</sub> is etched through. To investigate the scaling of mixing depth as a function of rf bias power and over-etch time, we simulated etching of a trench with an aspect ratio of 1 (trench width = trench depth  $\approx$  25 nm) as shown in Fig. 5.10a. The underlying Si layer is a multilayer structure with two colors representing the same material to better visualize the mixing. The mesh resolution is 3 Å. Over-etching begins when the SiO<sub>2</sub> is removed from the middle of the trench. The depth of the mixing layer generally increases with over etch time to an asymptotic value which increases with increasing bias power. The time evolution of the mixing depth at different rf bias powers is shown in Fig. 5.10b. The average mixing depth is plotted using data read from 10 identical profiles simulated with different random seed numbers. The onset of mixing during over-etch is somewhat randomly distributed and does not have a clear scaling correlation with rf bias power. This is because the first implanted particles are not necessarily more energetic at higher rf bias power since there is a distribution of ion energies which extends to lower energies. The general trend is an increase in mixing depth with increasing rf power up to about 15 nm at 4 kW.

Note that in these cases, there is significantly micro-masking of the SiO<sub>2</sub> which produces large variations in the height of the bottom of the trench [23,24]. As mentioned above, its representation here may be exaggerated due to the numerical meshing of our model. Micro-masking is also expected to worsen (on a relative basis) as the feature size decreases. Although particle (ions and neutrals) fluxes can be quite uniform along the wafer surface at macro scale, they can be statistically non-uniform on a micro-scale sur-

face. For our conditions, the ion flux is as high as  $10^{16} \text{ cm}^{-2}\text{s}^{-1}$  and neutral flux is as high as  $10^{17} \text{ cm}^{-2}\text{s}^{-1}$ . The time interval between two incident ions on a single surface site ( $3 \text{ \AA} \times 3 \text{ \AA}$ ) is around 0.1 s and 0.01 s between two incoming neutrals, an effect that is exacerbated by shadowing in high aspect ratio features having small openings to the plasma. Statistically, it is likely to have a sequence of radicals into the feature that locally produces a thicker polymer layer and other locations have an anomalously thin polymer layer. The end result is severe micro-masking that produces needle like structures that requires an over-etch to removed. Fortunately, the selectivity is high enough that the needles can be removed without significant damage to the underlying Si. The micro-masking is amplified compared to previous cases (as in Figs. 7-9) due to the thicker  $\text{SiO}_2$  layer and longer processing time. This micromasking is also more apparent in this lower aspect ratio feature compared to HAR features, as in Fig. 5.9. In HAR features, micro-masking is remediated by ions reflected from the side walls.

AR is another factor that may affect the mixing depth and shape of the damaged layer. For example, profiles for the bottom of trenches having different aspect ratios are shown in Fig. 5.11 for etching with an rf bias of 4 kW. The feature depth is 25 nm for an etch time of 17 s. The mesh resolution is  $3 \text{ \AA}$ . For an  $\text{AR} = 1$ , the trench bottom is relatively flat as is the underlying implanting and mixing layer. Some micro-trenching appears near the side walls. The thickness of the mixing layer (around 14 nm) does not appreciably change with AR nor does the extent of the mixing layer extending laterally to the sides of the feature (around 5 nm) appreciably change.

However as the AR increases by having a narrower feature while the lateral range of mixing remains constant, the relative extent of the mixing increases – that is, the lateral extent of mixing compared to the width of the feature increases. The more tapered profile at higher AR also results in more ions striking a surface at a more normal angle of incidence near the corners of the trench. The range of the ions into the solid at near normal incidence is generally larger than at grazing incidence. Therefore, even though on the average the ion energy is lower at the bottom of HAR features due to sidewall collisions, the mixing layer retains a broad extent.

Another consequence of mixing is vertical spatial variation in the mole fractions of species. For example, Si has a mole fraction of 1.0 in the undisturbed lattice below the mixing layer and a lower value in the mixing layer where there are, in these cases, significant mole fractions of  $C_xF_y$ . Predicted mixing layers on flat surfaces of trench bottom are shown in Fig. 5.12 after 8 s with parameters chosen to compare to the MD simulations of Végh et al. [25] Mixing of a Si layer was simulated for incident fluxes of  $CF/Ar^+ = 99/1$  with the CF at 300 K and the  $Ar^+$  at 200 eV (Fig. 5.12a); and for fluxes of  $CF/F/Ar^+ = 20/5/1$ , with CF at 1.5 eV, F at 300 K and  $Ar^+$  at 200 eV (Fig. 5.12b). The  $Ar^+$  flux is  $10^{15} \text{ cm}^{-2}\text{s}^{-1}$ . Results are shown “as etched” with the Ar still implanted, and “post-etch” after the Ar has diffused out of the mixed layer. The post-etch feature was obtained by simply removing the Ar from the lattice, assuming that the interstitial Ar would diffuse out during subsequent heating of the wafer without significantly disturbing the atom arrangement. There are some remaining dark blue squares, which are  $SiO_2C_xF_y$  complex.

For both cases the mixing layer has a reached steady state with little additional change in composition with time. The thickness of the polymer layer on top of Si will, however, continue to grow since there is almost no etching for the CF/Ar<sup>+</sup> case and very slow etching for the CF/F/Ar<sup>+</sup> case. In our model, the mixing depth under the C<sub>x</sub>F<sub>y</sub> polymer for either case is around 20~40 Å which is comparable to the MD results [25]. A comparison of our computed mixing layer composition as a function of depth with the MD simulation is shown in Fig. 5.13. The fluxes onto the surface in the MCFPM are the same as in the MD simulations. We do not resolve individual C and F atoms on the surface, and so our comparison for surface composition is based on polymer cells, referred to as C<sub>x</sub>F<sub>y</sub>. A difference between the accounting between our results and the MD is that C<sub>x</sub>F<sub>y</sub> polymer molecules are counted in our model whereas C atoms and F atoms are separately counted in the MD simulation. For the CF/Ar<sup>+</sup> case (Fig. 5.13a), the mixing layer in our model starts from about 13 Å and ends at about 42 Å which is comparable to MD result (18 Å ~ 41 Å). For the CF/F/Ar<sup>+</sup> case (Fig. 5.13b), although the mixing layer in our model is from 8 Å to 35 Å which is a bit shallower than MD result (20 Å ~ 41 Å), the thickness of the mixing layer is still comparable. In both cases, there is a region of about 10 Å thick where the C/Si ratio is about 1.

## 5.5 Concluding Remarks

Implantation and mixing have been incorporated into a Monte Carlo based feature profile model to predict damage during HAR etching of SiO<sub>2</sub> over Si in Ar/C<sub>4</sub>F<sub>8</sub>/O<sub>2</sub> plasmas. A quantitative validation of the model was conducted for mixing of a Si substrate during Ar<sup>+</sup> bombardment by comparison with MD simulations. When increasing

either bias power or ion energy, particles implant deeper and induce more mixing in the underlying material. For sufficiently thin SiO<sub>2</sub> layers over Si, the particles are able to penetrate through the SiO<sub>2</sub> to produce mixing in the underlying Si. Although the onset of mixing during over-etch has a somewhat statistical distribution, the mixing depth is proportional to bias power at the steady state. As the AR increases, the relative extent of the mixing layer laterally beyond the feature increases. For low AR, the bottom of the etch profile is relatively flat as is the mixing layer with small amounts of micro-trenching near the side walls. As the AR increases and feature width shrinks, the bottom of profile is more tapered whereas the lateral extent of the mixing is nearly constant. On average, mixing is deeper at lower AR due to more there being energetic ions incident onto the bottom of the feature – more ions strike the bottom prior to having glancing sidewall collisions.

## 5.6 Figures and Tables

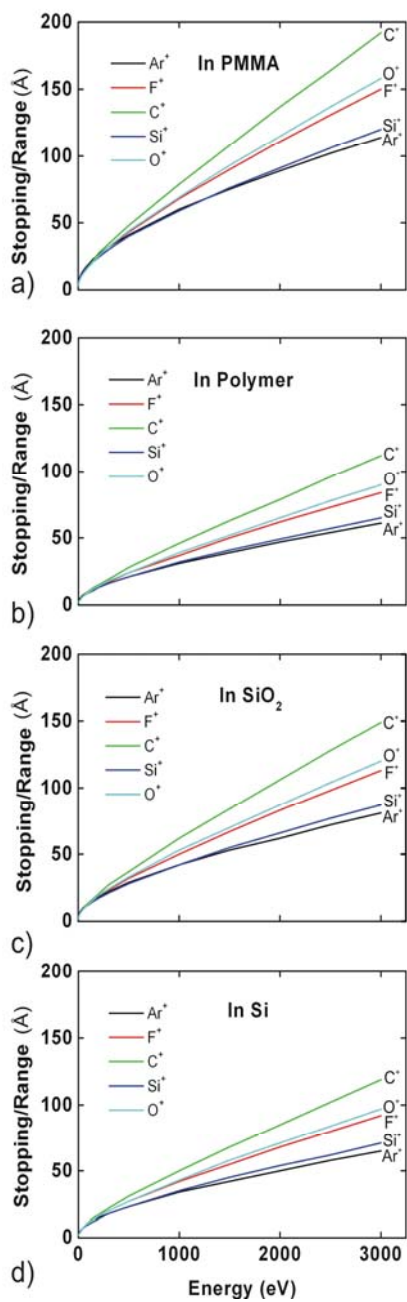


**Fig. 5.1** Stopping range as a function of ion energy calculated from SRIM for Ar<sup>+</sup>, F<sup>+</sup>, O<sup>+</sup>, Si<sup>+</sup>, and C<sup>+</sup> in a) PMMA (Polymethylmethacrylate); b) C<sub>x</sub>F<sub>y</sub> polymer (Teflon); c) SiO<sub>2</sub>; and d) Si.

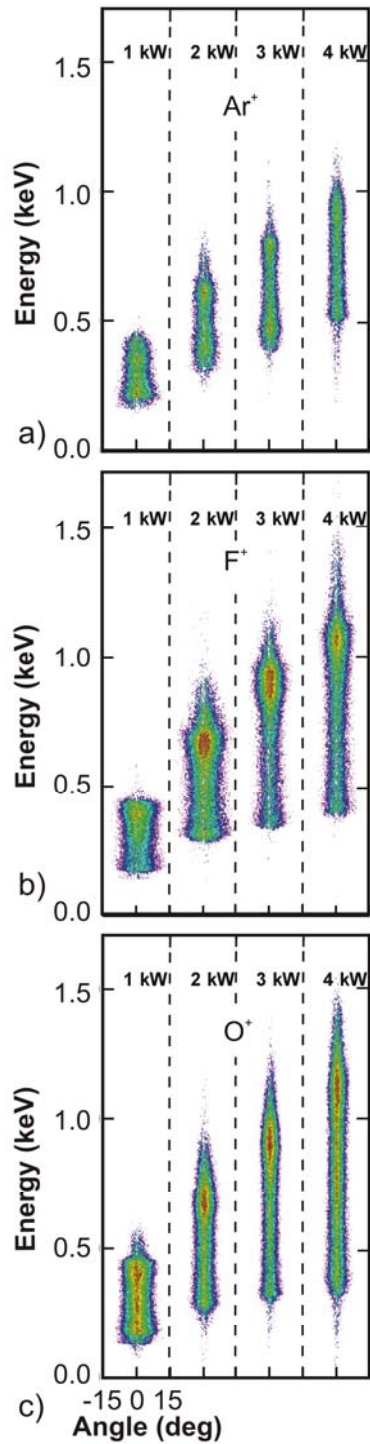


**Fig. 5.2** Energy and angular distributions of ions onto wafer surface at rf bias powers of 1-4 kW for: a) Ar<sup>+</sup>; b) F<sup>+</sup>; and c) O<sup>+</sup>. The operating conditions are Ar/C<sub>4</sub>F<sub>8</sub>/O<sub>2</sub> = 80/15/5 at 40 mTorr with a flow rate of 300 sccm. The substrate is biased at 10 MHz and the dc electrode delivers 200 W.

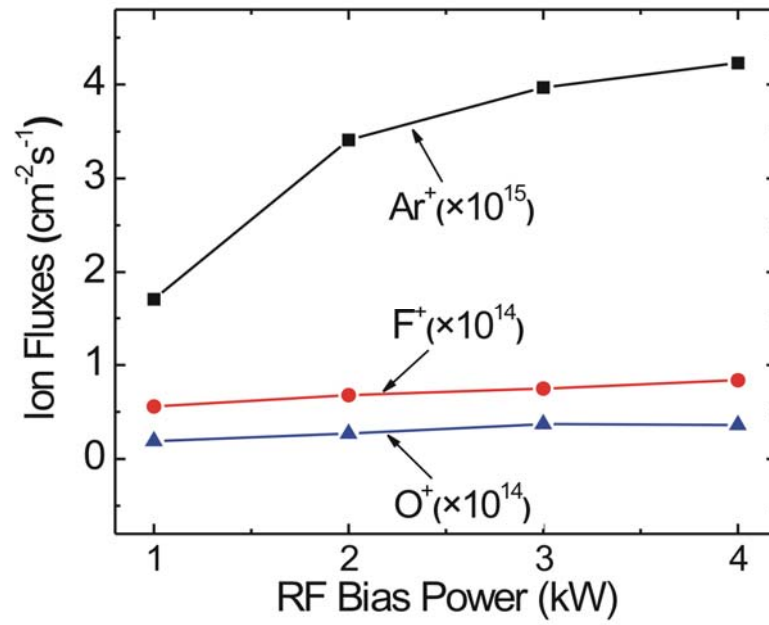


**Fig. 5.3** Ion fluxes onto the wafer surface at rf bias powers 1-4 kW (Ar/C<sub>4</sub>F<sub>8</sub>/O<sub>2</sub> = 80/15/5, 40 mTorr, 300 sccm, 10 MHz)

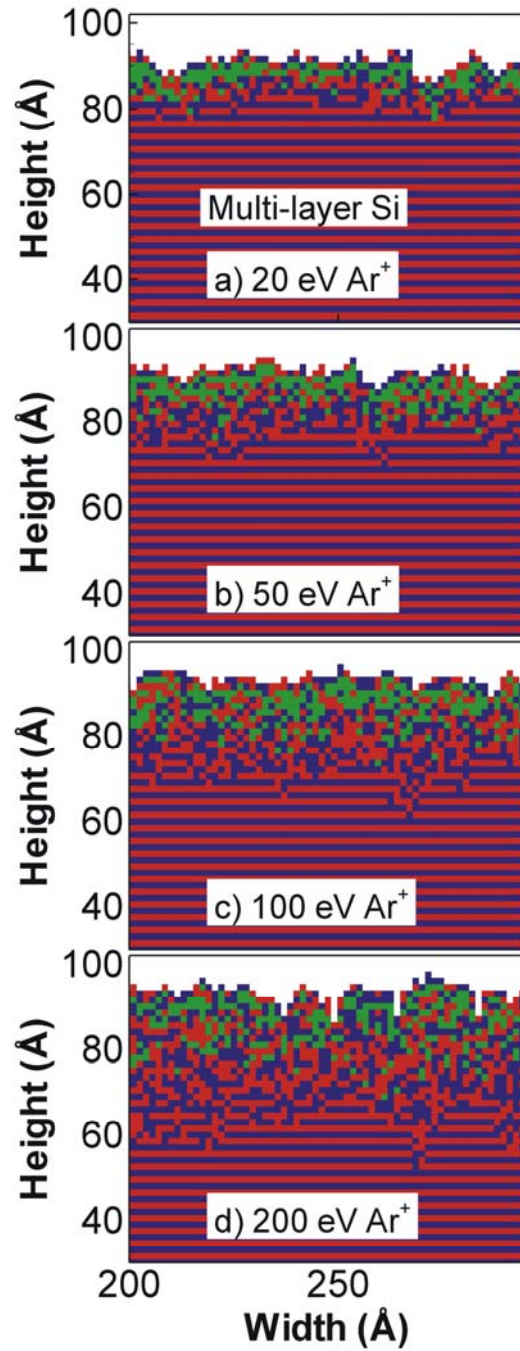


**Fig. 5.4** Implanting and mixing depth in Si substrate under  $\text{Ar}^+$  bombardment with an energy of: a) 20 eV; b) 50 eV; c) 100 eV; and d) 200 eV. The Si is shown multi-layer (different colors) to better display the mixing. The green is interstitial argon.

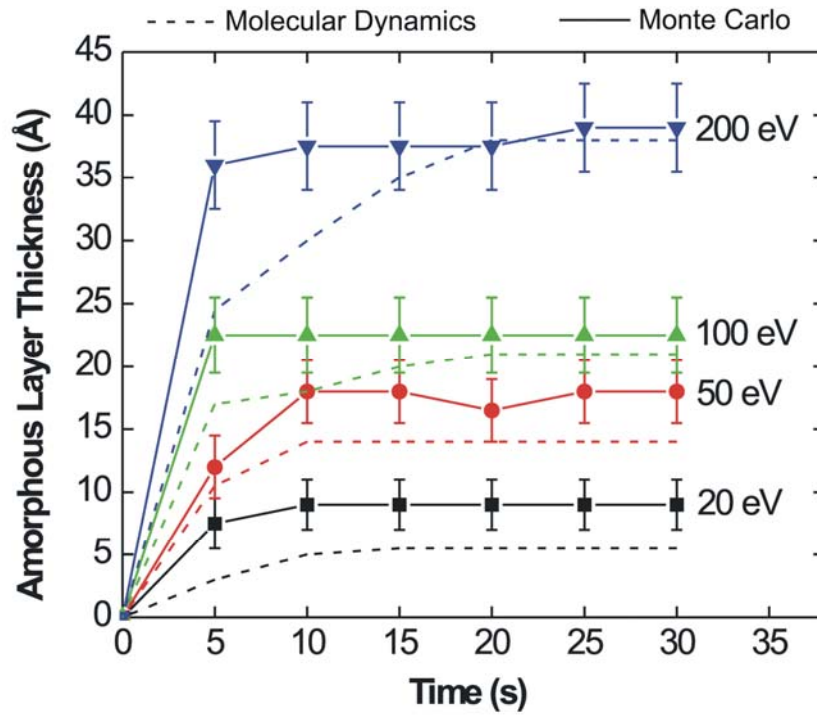
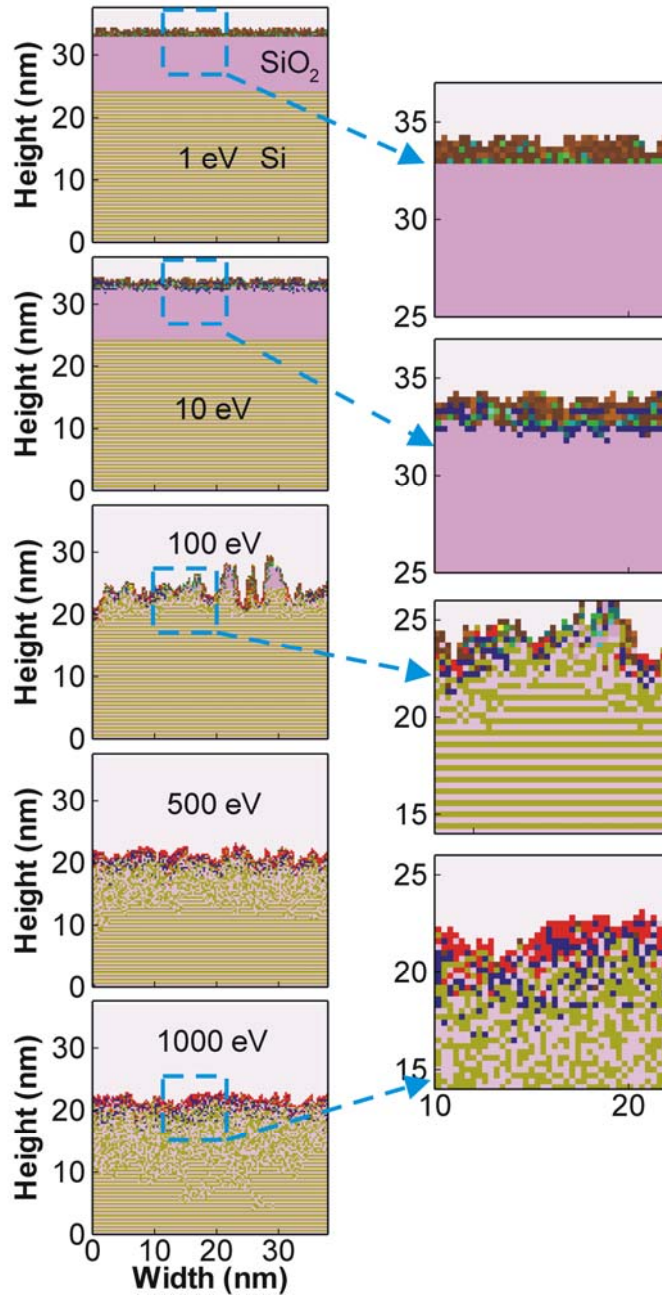
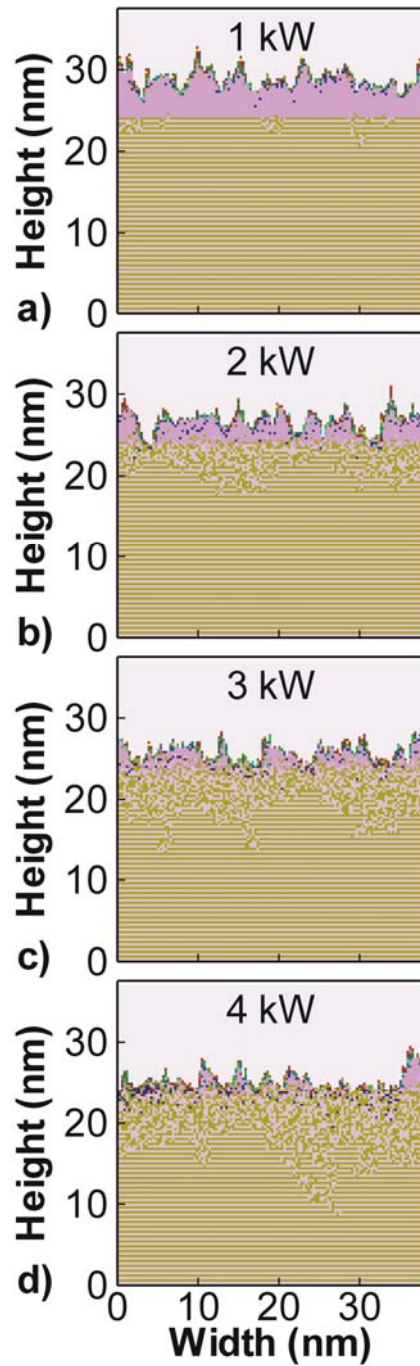


Fig. 5.5 Amorphous (mixing) layer depth as a function of ion energy. Solid lines are results from the model, dashed lines are published MD simulations from Ref. [13]. The mixing layer forms quickly before achieving a near steady state.



**Fig. 5.6** Profile and composition during etch of SiO<sub>2</sub> over Si at ion energies of (top to bottom): 1 eV, 10 eV, 100 eV, 500 eV; and 1000 eV. Although the ion energies are fixed, the composition of the fluxes is as produced by the model. The Si is shown multi-layered to better visualize mixing. Color coding: Brown and green - polymer species. Dark blue - implanted particles. Red - sputtered residues.



**Fig. 5.7** Profile and composition during etch of SiO<sub>2</sub> over Si for a constant etch time of 5 s for rf powers of a) 1 kW; b) 2 kW; c) 3 kW; and d) 4 kW. The color coding is the same as for Fig. 7. The mixing depth increases due to the thinning of the SiO<sub>2</sub> layer and longer range with increasing power.

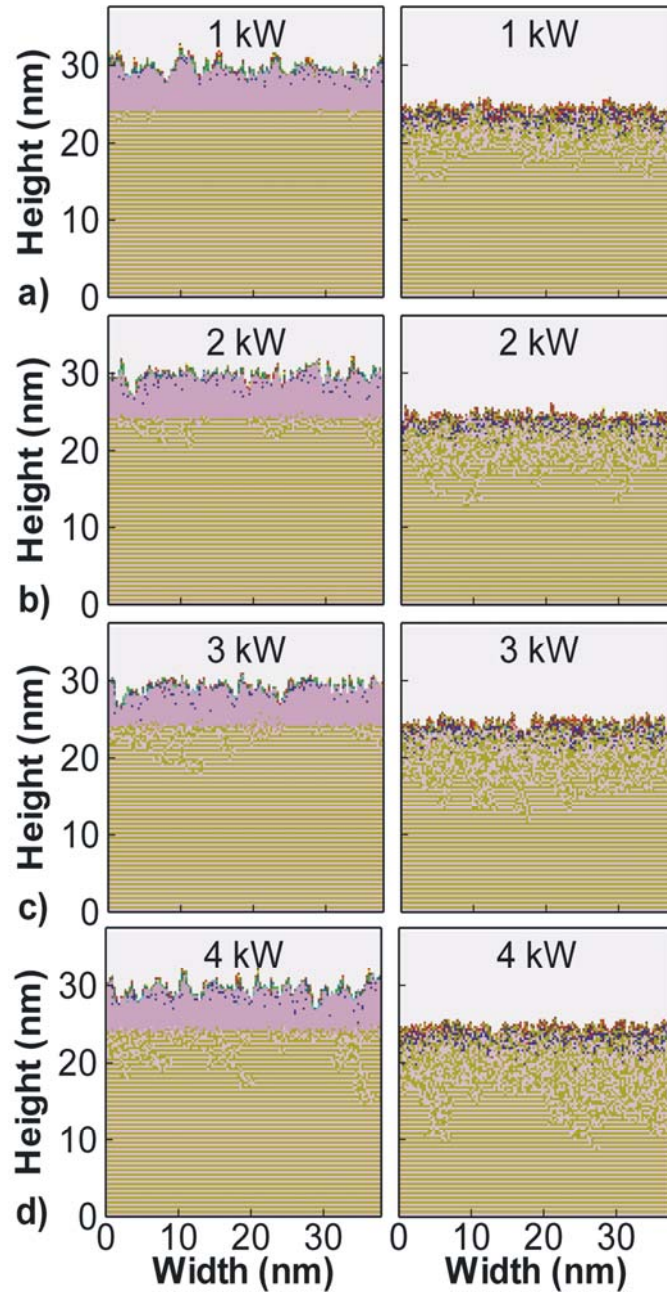


**Fig. 5.8** Profile and composition during etch of  $\text{SiO}_2$  over Si for a constant etch depth for rf powers of a) 1 kW; b) 2 kW; c) 3 kW; and d) 4 kW. (left) With a finite thickness of  $\text{SiO}_2$  and (right) approximately when the Si interface is reached. The color coding is the same as for Fig. 7. At higher powers, mixing in the Si occurs even with a thick  $\text{SiO}_2$  layer due to the longer range of ions.

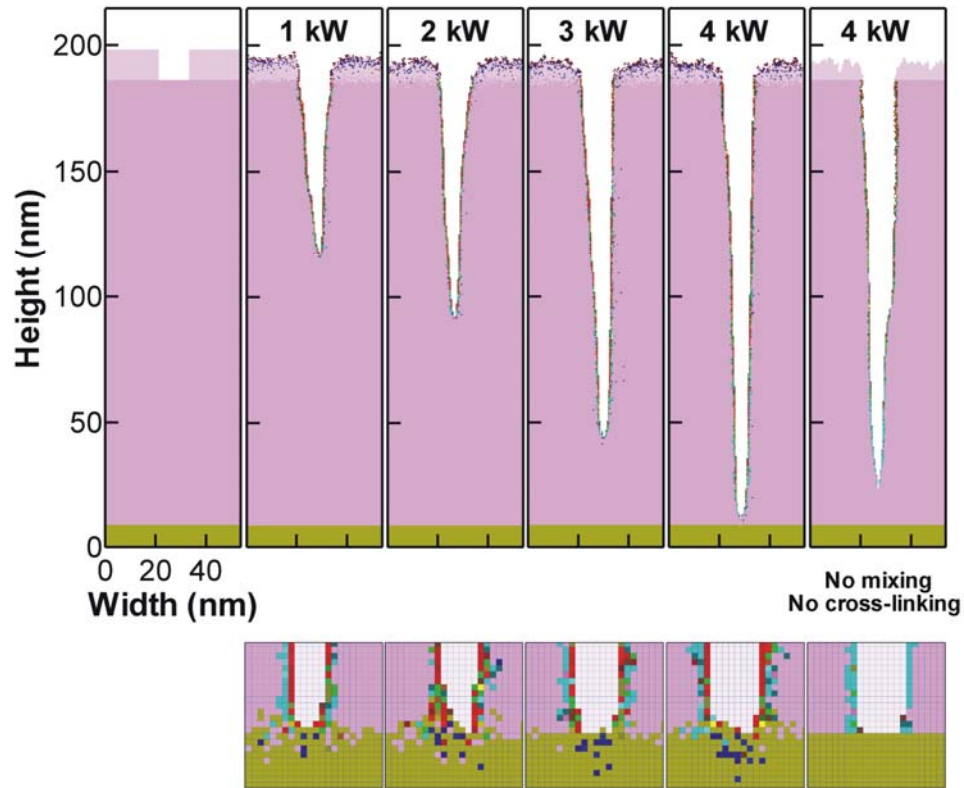


**Fig. 5.9** Etch properties as a function of bias power (1-4 kW). (top row) Etch profiles as a function of power for the same etch times. (bottom row) Mixing at the bottom of the trench for the same over etch time. A case without implantation and PR cross-linking is shown for comparison.

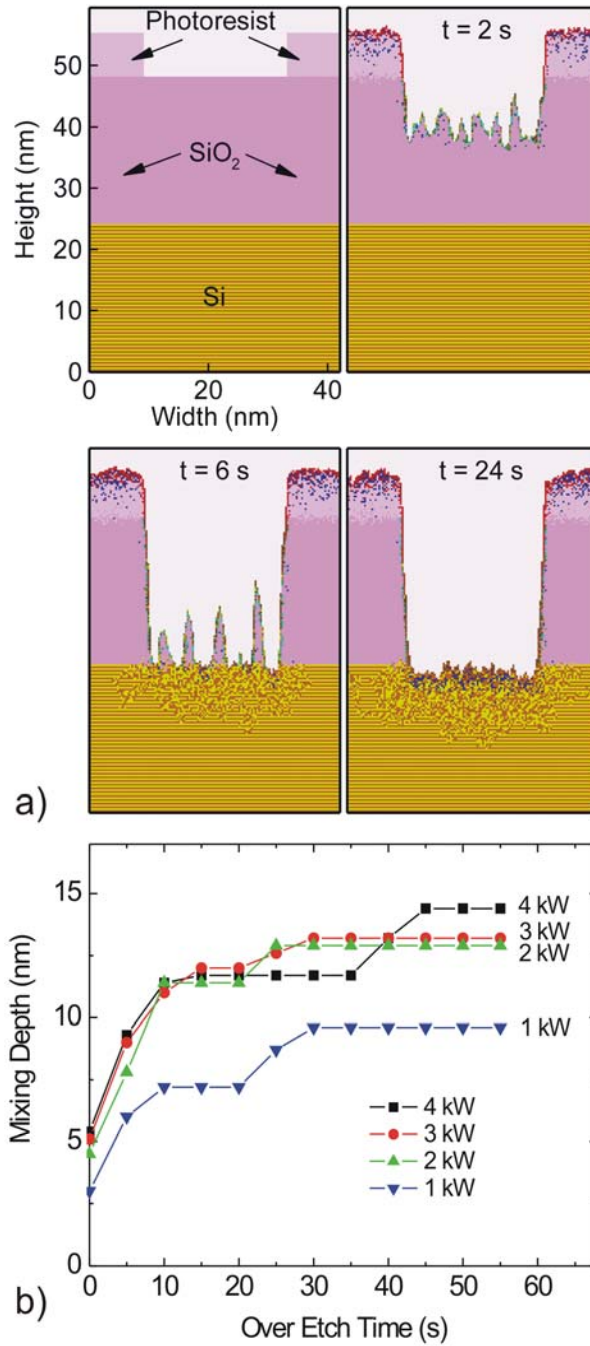


**Fig. 5.10** Mixing layer depth as a function of over-etch time. a) Etching of a small AR feature as a function of time. b) Mixing layer depth in this feature as a function of over-etch time for bias powers of 1-4 kW.

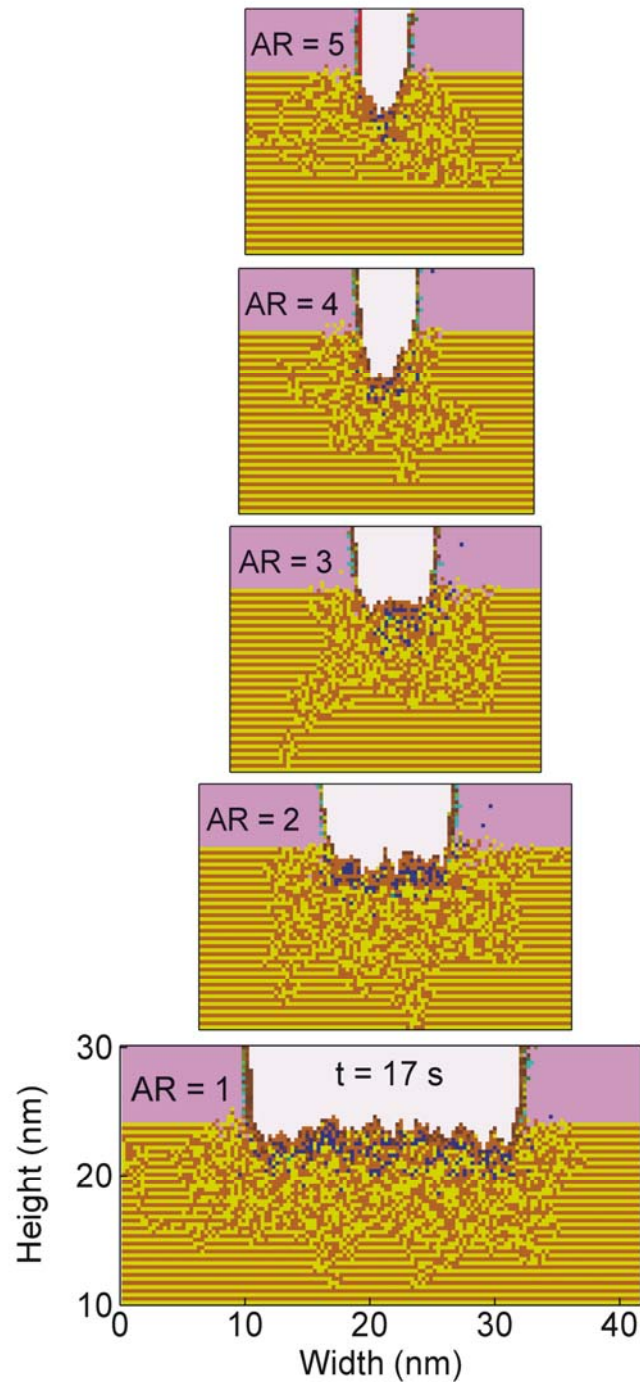


**Fig. 5.11** Etching profile and mixing layer shape as a function of feature aspect ratio (from top to bottom, 5, 4, 3, 2 and 1) for a bias power of 4 kW. At high AR, the relative lateral extent of the mixing layer is larger.

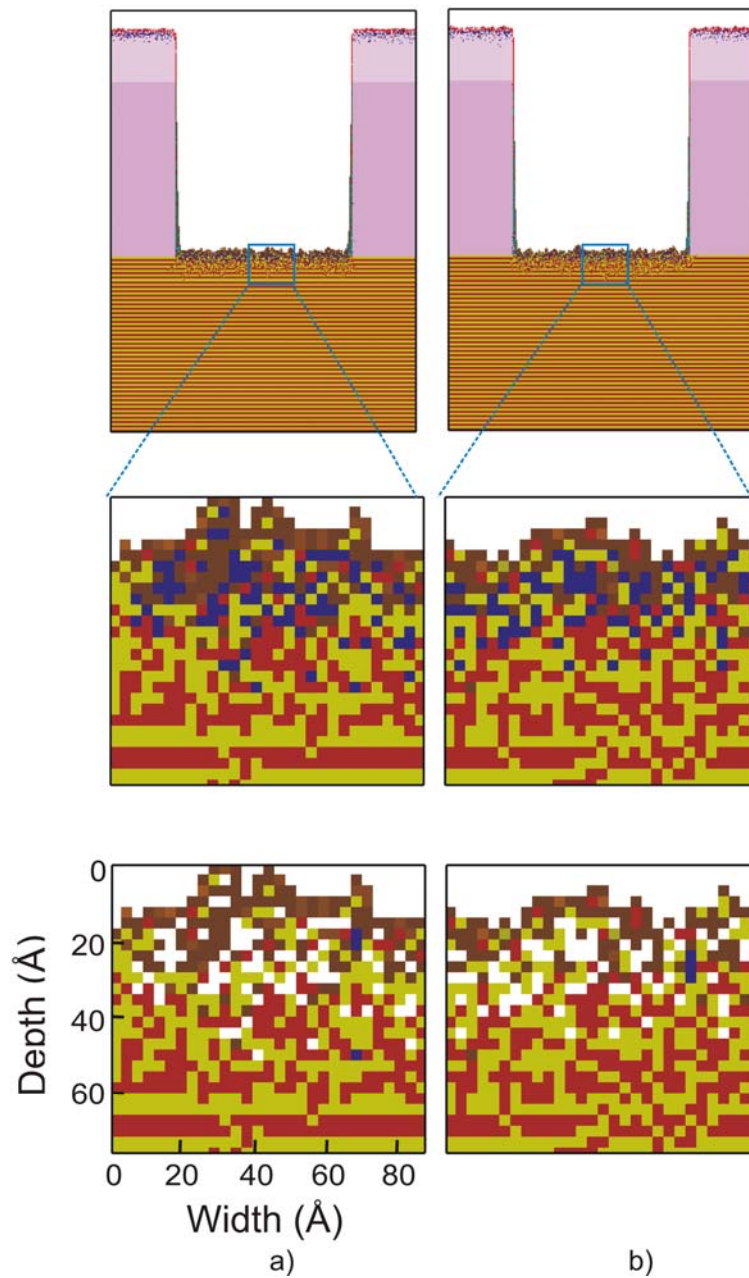


**Fig. 5.12** MCFPM simulation of polymer deposition and mixing in underlying Si for fluxes of a). CF/Ar<sup>+</sup> = 99/1. The CF is at 300 K and the Ar<sup>+</sup> is monoenergetic at 200 eV. b) CF/F/Ar<sup>+</sup> = 20/5/1. The CF is at 1.5 eV, the F at 300 K and the Ar<sup>+</sup> is at 200 eV. The enlarged images are for (middle) as etched with Ar implantation (dark blue) and (bottom) post-etch with Ar having diffused out of the mixing layer.

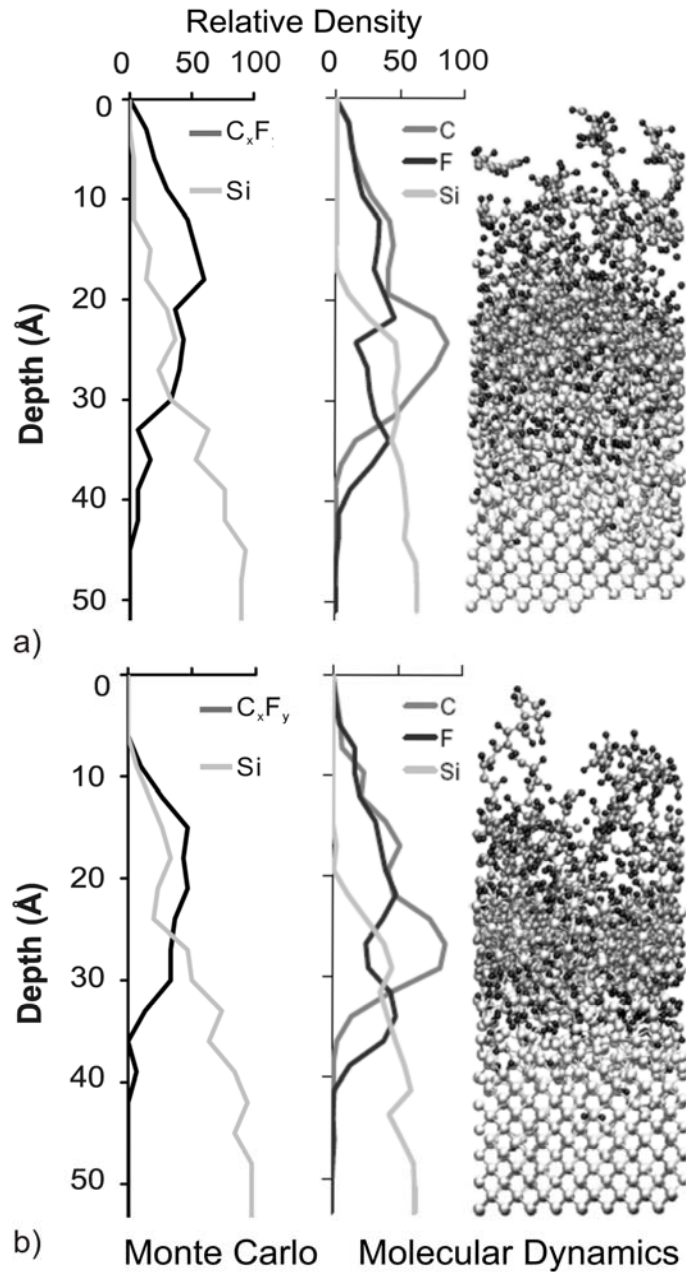


**Fig. 5.13** Comparison between (left) MCFPM and (right) molecular dynamics simulation (from Ref. [26]) for atomic or molecular constituents as a function of depth for fluxes of:  $CF/Ar^+ = 99/1$ . The CF is at 300 K and the  $Ar^+$  is monoenergetic at 200 eV. **b)**  $CF/F/Ar^+ = 20/5/1$ . The CF is at 1.5 eV, the F at 300 K and the  $Ar^+$  is at 200 eV. The Monte Carlo results are “post-etch” with the implanted Ar atoms removed.

**Table I. Fluxes of radicals and ions incident onto the wafer**

Particle	Flux ( $10^{15} \text{ cm}^{-2} \text{ s}^{-1}$ )		Particle	Flux ( $10^{15} \text{ cm}^{-2} \text{ s}^{-1}$ )
$\text{Ar}^+$	4.23		CF	0.32
$\text{CF}_3^+$	0.26		$\text{CF}_2$	1.86
$\text{CF}_2^+$	0.15		$\text{C}_2\text{F}_4$	29.6
$\text{F}^+$	0.08		$\text{C}_3\text{F}_5$	0.32
$\text{O}^+$	0.04		F	3.2
$\text{C}_2\text{F}_4^+$	4.28		$\text{F}_2$	0.04
$\text{C}_3\text{F}_5^+$	1.23			
$\text{C}_3\text{F}_6^+$	0.002			
$\text{C}_4\text{F}_7^+$	0.006			

## 5.7 References

1. K. H. R. Kirmse, A. E. Wendt, S. B. Disch, J. Z. Wu, I. C. Abraham, J. A. Meyer, R. A. Breun, and R. Claude Woods, *J. Vac. Sci. Technol. B* **14**, 710 (1996).
2. G. S. Oehrlein and H. L. Williams. *J. Appl. Phys.* **62**, 662 (1987).
3. M. Wang and M. Kushner, *J. Appl. Phys.* **107**, 023309 (2010).
4. S. Noda, N. Ozawa, T. Kinoshita, H. Tsuboi, K. Kawashima, Y. Hikosaka, K. Kinoshita, M. Sekine, *Thin Solid Films*, **374**, 181 (2000).
5. D. Humbird and D. B. Graves, *J. Appl. Phys.* **96**, 65 (2004).
6. S. Rauf, T. Sparks, P. L. G. Ventzek, V. V. Smirnov, A. V. Stengach, K. G. Gaynul-lin, and V. A. Pavlovsky, *J. Appl. Phys.* **101**, 033308 (2007).
7. I. H. Wilson, N. J. Zheng, U. Knipping, I. S. T. Tsong, *Phys. Rev. B* **38**, 8444 (1988).
8. A. Agarwal, T. E. Haynes, D. J. Eaglesham, H-J. Gossmann, D. C. Jacobson, J. M. Poate, Y. E. Erokhin, *Appl. Phys. Lett.* **70**, 3332 (1997).
9. J. P. Chang and H. H. Sawin, *J. Vac. Sci. Technol. A* **15**, 610 (1997).
10. T. K. Chini, F. Okuyama, M. Tanemura, K. Nordlund, *Phys. Rev. B* **67**, 205403 (2003).
11. A. A. E. Stevens, W. M. M. Kessels, M. C. M. vande Sanden, and H. C. W. Beijer-inck. *J. Vac. Sci. Technol. A* **24**, 1933 (2006).
12. D. B. Graves and D. Humbird, *Appl. Sur. Sci.* **192**, 72 (2002).
13. D. Humbird, D. B. Graves, A. A. E. Stevens and W. M. M. Kessels, *J. Vac. Sci. Technol. A* **25**, 1529 (2007).

14. T. Ohchi, S. Kobayashi, M. Fukasawa, K. Kugimiya, T. Kinoshita, T. Takizawa, S. Hamaguchi, Y. Kamide, and T. Tatsumi, *Jap. J. Appl. Phys.* **47**, 5324 (2008).
15. A. Matsuda, Y. Nakakubo, Y. Takao, K. Eriguchi, K. Ono, *Thin Solid Films*, **518**, 3481 (2010).
16. C. Steinbrüchel, *Appl. Phys. Lett.* **55**, 1960 (1989).
17. W. Eckstein, C. García-Rosales and J. Roth and J. László, *Nucl. Instrum. Methods Phys. Res. B* **83**, 95 (1993).
18. K. Ono, H. Ohta and K. Eriguchi, *Thin solid Films* **518**, 3461 (2010).
19. Y. Osano and K. Ono, *J. Vac. Sci. Technol. B* **26**, 1425 (2008).
20. P. Moroz, 52<sup>nd</sup> Annual Meeting of the APS Division of Plasma Physics, Paper PP9.33, 2010. [Bulletin Am. Phys. Soc. 2010.DPP.PP9.33, 2010]
21. T. Shimada, T. Yagisawa and T. Makabe, *Japn. J. Appl. Phys.* **45**, 8876 (2006).
22. A. V. Vasenkov and M. J. Kushner, *J. Appl. Phys.* **95**, 834 (2004).
23. K. P. Larsen, D. H. Petersen, and O. Hansen, *J. Electrochem. Soc.* **153**, G1051 (2006);
24. P. Dixit and J. Miao, *J. of Physics: Conference Series* **34** 577 (2006).
25. J. J. Végh, D. Humbird, and D. B. Graves, *J. Vac. Sci. Technol. A* **23**, 1598 (2005).

## **6. ELIMINATING OF POLYMETHYLMETHACRYLATE (PMMA) DEGRADATION BY VUV EXPOSURE AND SI DEPOSITION IN DIELECTRIC ETCHING**

### **6.1 Introduction**

In plasma etching, bowing is an anomalous behaviors in which the sides of the feature near the top bow out late during the etch [1, 2]. Bowing is typically a more reproducible and systematic effect than twisting. One of the proposed bowing mechanisms is a result of ion-induced changes in the slope of the photoresist (PR, usually is a C-H based polymer) surface [3]. 193 nm PR material polymethylmethacrylate (PMMA), as shown in Fig. 6.1, for example, is widely used in defining sub-micron to nano-scale features [4, 5]. Its softness makes it is easy to degrade and this degradation produces a rough surface during the energetic ion bombardment that occurs during plasmas etching[6–8]. Energetic ions impacting onto the PR surface can reflect to the side walls of trenches as shown in Fig. 6.2.

The PR initially usually has a domed shape and is relatively thick compared to the trench width. The initial surfaces do not reflect many energetic ions onto the trench side walls. As etching proceeds, the PR is eventually eroded. When the PR is thin enough, bowing occurs due to reflection off the facets. Multi-layer masks (PR-hard mask) and deposition of a passivation layer onto the PR surface have been proposed to protect the PR to prevent this erosion and so minimize bowing. Meanwhile, as more dangling bonds are created due to ion bombardment, they may reconnect to cross-link the polymer. These cross-linked C-H polymers are more resistive to etching than the original polymer,

such as PMMA. VUV (vacuum ultraviolet radiation) exposure also has the ability of breaking C-O-C and C=O bonds in 193 nm PR and inducing cross-linking [9, 10].

Strategies for protecting the integrity of PR during plasma etching and maintaining the desired etch feature shape will be discussed using results from a computational investigation. A dc augmented dual frequency Capacitively Coupled Plasma (CCP) Reactor is simulated using the Hybrid Plasma Equipment Model (HPEM). The gas mixture is  $r/C_4F_8/O_2$  plasmas with powers of 1~4 kW rf bias power at 5 MHz applied to the bottom electrode to produce energetic ions, neutrals, and UVU fluxes. A dc power of 200~2000 W is applied to the top electrode to produce Si fluxes by bombarding the top electrode surface with energetic ions. A 500 W rf power at 60 MHz is also applied to the top electrode to enhance ionization. The reaction mechanism of degradation and cross-linking of PR (PMMA) due to ion bombardment will be investigated in nano-scale using the MCFPM (Monte Carlo Feature Profile Model). Also, consequences of VUV-induced cross-linking and Si deposition in the surface layer of PR will be discussed in detail.

## 6.2 Scaling of Etch Selectivity

A dc augmented dual frequency CCP reactor was simulated in  $Ar/C_4F_8/O_2$  plasmas using HPEM. The base case conditions are: 500 W at 60 MHz and dc 200 W applied on top electrode, 1 kW at 5 MHz applied to the bottom electrode, 40 mTorr, 300 sccm,  $Ar/C_4F_8/O_2=80/15/5$ . The reactor is the same as shown in Fig. 4.1. For a rf bias power of 4 kW, etch selectivity for  $SiO_2$  over PR (PMMA) and Si was investigated using MCFPM as shown in Fig. 6.3. After processing for 10s, there is almost no etching for Si. An etch stop occurs because of the low reaction rate between Si and  $C_xF_y$  polymer spe-

cies on the surface.  $C_xF_y$  polymer deposition, energetic ion ( $Ar^+$  for example) sputtering, implanting, and mixing coexist at Si surface, which produces a steady state polymer layer. 10-nm-thick PR material (PMMA) is eroded if cross-linking is not considered as shown in Fig. 6.3b. The etch selectivity (S) between  $SiO_2$  over PMMA is around 10. When cross-linking due to bond-breaking is included (Fig. 6.3c), the etch selectivity increases to 17. There is still 5-nm-thick PMMA eroded since sputtering and etching dominants over cross-linking. Cross-linking is produced by the reconnection of exposed dangling bonds on the PMMA surface due to ion bombardment. In the current model, the etching yield for cross-linked PMMA is 5 times smaller than for non-crosslinked PMMA.

The scaling of etching selectivity S for  $SiO_2$  over PMMA with ion energy ( $\epsilon_{ion}$ ) is shown in Fig. 6.4. First, we investigated S as a function of ion energy without considering cross-linking as shown in Fig. 6.4a. At 100 eV, when ions are not energetic enough to etch rapidly, the etch selectivity is  $S \approx 1$ . As the ion energy increases, the etching rate for both materials increases. A higher etch rate increment for  $SiO_2$  results in a higher selectivity,  $S \approx 7$  at  $\epsilon_{ion} = 100$  eV; and  $S \approx 9$  at  $\epsilon_{ion} = 1000$  eV. Then, the same cases are simulated while including cross-linking of PMMA (Fig. 6.4b). With higher  $\epsilon_{ion}$ , the sputtering yield also increases, which generates more dangling bonds on the surface. Thus, the dominant process for PMMA is still etching but with there being more cross-linking as well. As shown in Fig. 6.4b, the etch selectivity for  $SiO_2/PMMA$  responds proportionally to ion energy:  $S \approx 3$  at  $\epsilon_{ion} = 100$  eV;  $S \approx 13$  at  $\epsilon_{ion} = 500$  eV; and  $S \approx 16$  at  $\epsilon_{ion} = 1000$  eV.

The correlation between PR (PMMA) thickness and feature aspect ratio was then investigated. The limiting feature aspect ratio (LFAR) is that depth at which the PR mask is fully eroded so that the feature is no longer defined. Results are shown in Fig. 6.5a. If PMMA cross-linking is not considered (square dots), the LFAR increases almost linearly with PMMA layer thickness up to 25 nm. At that point, thicker PMMA is needed to produce a given increase in LFAR. This is because the etch rate decreases with increasing AR due to there being collisions with the side walls which reduces ion energy as well as charging on the feature sidewall surfaces. When including PMMA cross-linking (triangle dots), a larger LFAR is obtained with same PR thickness. The difference between with and without cross-linking tends to be larger as the PMMA thickness increases. This is due to there being more cross-linking producing more etch rate drop in the PR layer the longer the PMMA is exposed. As the trench depth and aspect ratio increases, the PMMA continues to be eroded until feature definition is lost at 96 s as shown in Fig. 6.5b. Other strategies are needed to protect the PR and to retain the CD (critical dimension) when the PR is too thin to achieve a desired high aspect ratio feature profile.

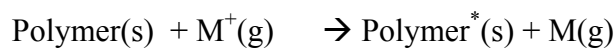
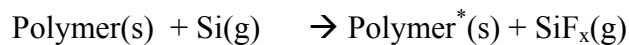
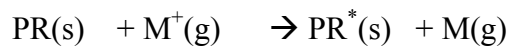
### **6.3 Strategies to Eliminate PR Erosion**

One of the proposed mechanisms to prevent PR etching and retain CD is to generate fluxes of Si radicals onto the PR surface. The mechanism for this method is shown in Fig. 6.6. We add a negative DC voltage on the top electrode, which forms a negative dc sheath. This strong negative sheath potential accelerates ions in the bulk plasma through the sheath into the top electrode surface (Si coated), and so produce Si radicals by sputtering. These Si radicals then diffuse through the plasma to the substrate. Most of the Si

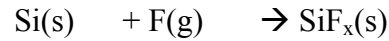
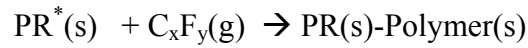
radicals deposit on the PR surface since the trench opening is small, and the trajectory of incident Si particles is isotropic. The physical absorption of Si could protect the under-layer PR since Si itself is much less reactive in  $C_xF_y$  plasma. Chemical absorption of Si (e.g. formation of harder Si-C bonds) could also protect the PR. Furthermore, Si extraction of one or more F atoms from deposited  $C_xF_y$  polymer on the PR surface can produce a more reactive surface which can promote further polymer deposition, which can protect the PR from erosion.

VUV (vacuum ultraviolet radiation) photons are also included in the reaction mechanism. Here, we only consider the 105 nm lines ( $\sim 11.8$  eV) produced by relaxation of excited state  $Ar^*$ . VUV photons can break chemical bonds (C=O or C-O-C) in PMMA to produce  $C\cdot$  dangling bonds. Thus, they can induce cross-linking and form a carbon rich layer, which is more resistive to etching than virgin PMMA [11]. Also, Si radicals can easily attach to the  $C\cdot$  dangling bonds on the PR surface produced by VUV photons. The reaction mechanism is shown below:

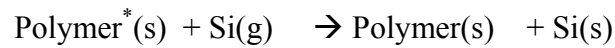
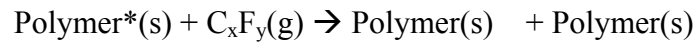
Step 1: PR and  $C_xF_y$  polymer activation.



Step 2: Deposition of Si,  $C_xF_y$  polymer passivation.



Step 3: Further deposition.



Where  $M^+$  is an energetic ion and  $M$  is its corresponding fast neutral.

### 6.3.1 Scaling of Si and VUV Fluxes with DC Power

When varying the DC power on the top electrode, we obtained different ion angular and energy distributions onto the top electrode surface as shown in Fig. 6.7. As the DC power increases from 200 W to 2 kW, the potential of the DC sheath near the surface of the top electrode also increases. This stronger negative potential then attracts more positive ions striking onto the electrode surface. The higher sheath potential provides more acceleration to the ions, which results in their higher energy and narrower angle spread (Fig. 6.7).

More energetic ion bombardment produces more Si by sputtering and so larger fluxes to the substrate. Si and photon fluxes as a function of DC power are shown in Fig. 6.8. The Si flux as well as the Si flux to ion flux ratio increases at higher DC power.

More VUV flux is also generated when increasing the DC power, although the magnitude of the VUV flux is two orders of magnitude lower than the Si flux and ion flux. The VUV photon flux over total ion flux ratio does not show a clear correlation with DC power.

### 6.3.2 Effects of Si and VUV fluxes on PR erosion

Si and VUV photon fluxes obtained at a DC 2 kW were used to investigate their effects on PR erosion as shown in Fig. 6.9. Without Si and VUV photon fluxes, the PR is slowly etched due to ion bombardment (Fig. 6.9a). When only additional VUV photon fluxes are included, the etch rate does not significantly change (Fig. 6.9b). Due to the long mean-free-path of the VUV photons into the PR, cross-linking (shown by red pixels) are distributed deep into the PR and not concentrated near the surface where cross linking could slow the etch rate. The VUV flux also has a small effect due to its lower value ( $\sim 5 \times 10^{13} \text{ cm}^{-2}\text{s}^{-1}$ ) compared to the ion flux. When only the additional Si flux is introduced, it is sufficient to ultimately increase the rate of polymer deposition (green) and produce a Si-C rich layer (yellow) on the PR surface (Fig. 6.9c). Si radical extracts F atoms from  $\text{C}_x\text{F}_y$  polymer and then produces more polymer deposition. An etch stop is basically achieved. When VUV photon flux and Si fluxes coexist, more fluorocarbon polymer is deposited due to a synergic effect from these two fluxes (Fig. 6.9d).

### 6.3.3 Flux Sensitivity

The VUV photon flux ( $\sim 5 \times 10^{13} \text{ cm}^{-2}\text{s}^{-1}$ ) obtained at DC 2 kW is too small to cause any significant effect on PR erosion, while the Si flux ( $\sim 3 \times 10^{15} \text{ cm}^{-2}\text{s}^{-1}$ ) is high enough to produce an etch stop on the PR surface. To obtain a quantitative estimate of

how high the VUV flux needs to be to affect the etching rate, we simulated PR etch with different VUV fluxes as shown in Fig. 6.10. When doubling the VUV flux ( $\Gamma_{\text{VUV}}$ ), the PR etch rate is slightly reduced (Fig. 6.10c). If increasing the VUV flux by 10 times, polymer deposition begins to dominate (Fig. 6.10d).

Also, to investigate how small the Si flux needs to be to lose its capability of stopping etch, we simulated PR etch with different Si fluxes (Fig. 6.11). When reducing the Si flux ( $\Gamma_{\text{Si}}$ ) a factor of 2, there is a reduction of polymer deposition on PR surface but there is sufficient polymer to slow the etch rate Fig. 6.11c. When reducing the Si flux by a factor of 10, etching starts to dominate (Fig. 6.11d).

#### 6.4 Concluding Remarks

We have investigated the consequences of energetic ion bombardment as a means to etch and to protect the PR. Ion sputtering can degrade the PR polymer chain and induce cross-linking at the same time. Cross-linked PR surfaces are approximately five times more resistive to etch than normal PR. However, as etching proceeds and the aspect ratio of a trench increases, the PR is eventually eroded. Another strategy to protect the PR and increase the LFAR is to deposit a Si layer on the PR surface. Si fluxes obtained from a dc-CCP reactor due to ion sputtering of the top electrode surface can form Si-C bonds or extract F atoms from the  $\text{C}_x\text{F}_y$  polymer to promote further polymer deposition. The SiC-rich layer combined with a thicker  $\text{C}_x\text{F}_y$  polymer layer can lead to an etch stop if the Si flux is sufficiently high ( $> 10^{15} \text{ cm}^{-2}\text{s}^{-1}$ ). VUV photons can also induce PR cross-linking of PR and  $\text{C}_x\text{F}_y$  polymer chains. When VUV flux is sufficiently high, it can

promote cross-linking and polymer deposition on the PR surface and protect the PR.

VUV and Si fluxes can have a synergic effect that better preserves PR.

## 6.5 Figures

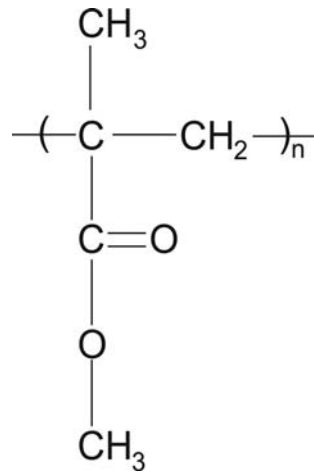


Fig. 6.1 Schematic of PMMA molecular structure.

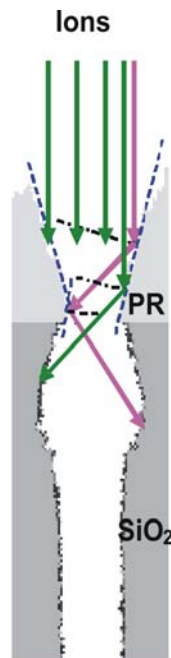
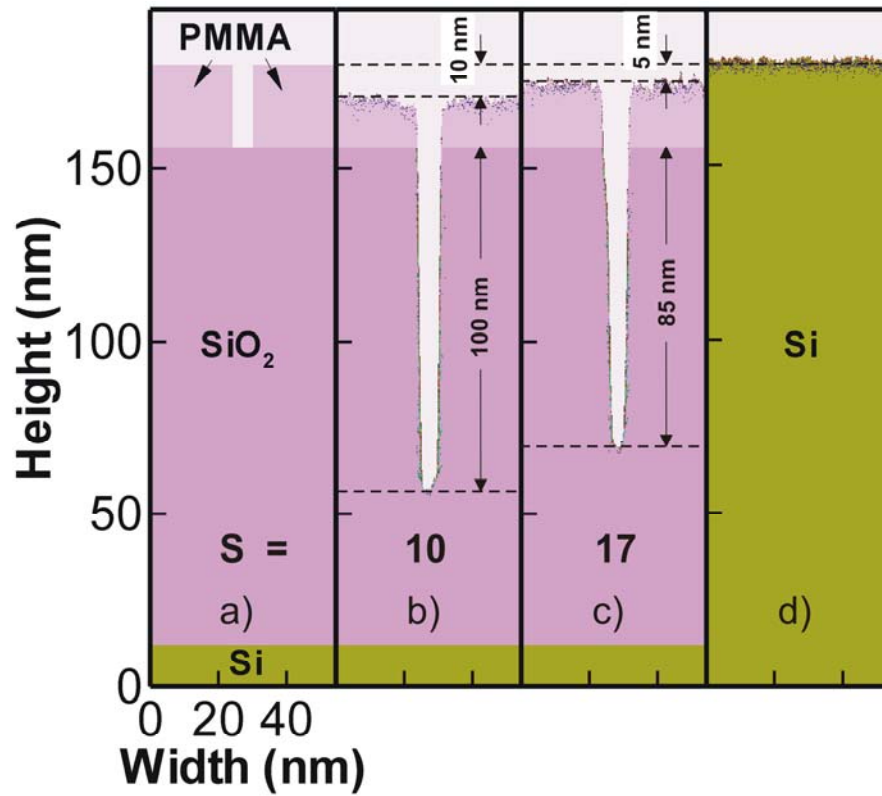
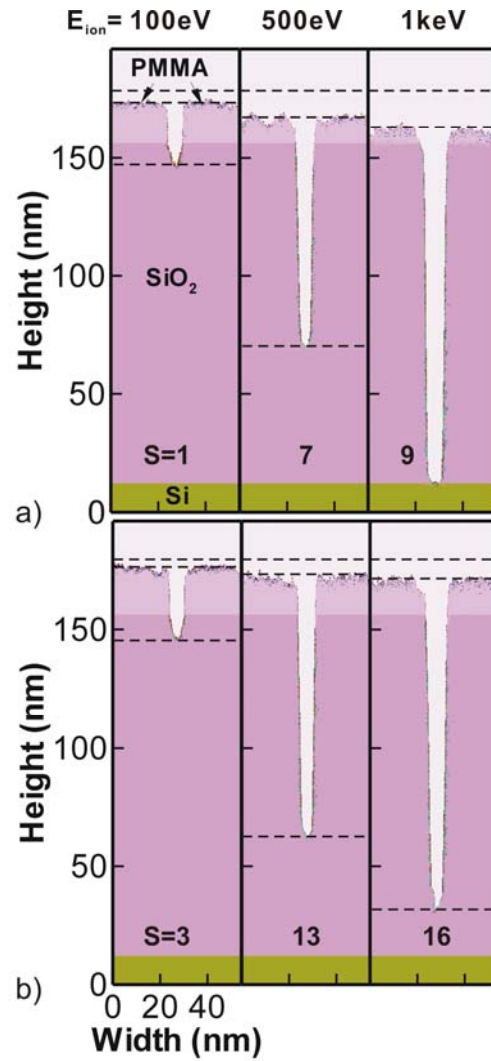


Fig. 6.2 Bowing mechanism during HAR etching in SiO<sub>2</sub>. Energetic ions striking onto the tapered photoresist surface reflect to the top of etching feature where bowing is created.



**Fig. 6.3 Etching selectivity for SiO<sub>2</sub> / PMMA: (a) Initial profile; (b) Without cross-linking; (c) With cross-linking. (d) Etching profile for Si. Profiles are shown after etching for 10 second. Etching selectivity for SiO<sub>2</sub> / PMMA is: (b) 10; (c) 17. Etching selectivity for SiO<sub>2</sub> / Si is infinite.**



**Fig. 6.4** Etching selectivity  $S$  for PMMA/SiO<sub>2</sub> as a function of ion energy: (a) Without PR cross-linking ( $S \approx 1$  at 100 eV,  $S \approx 7$  at 500 eV, and  $S \approx 9$  at 1000 eV); (b) With PR cross-linking ( $S \approx 3$  at 100 eV,  $S \approx 13$  at 500 eV, and  $S \approx 16$  at 1000 eV).

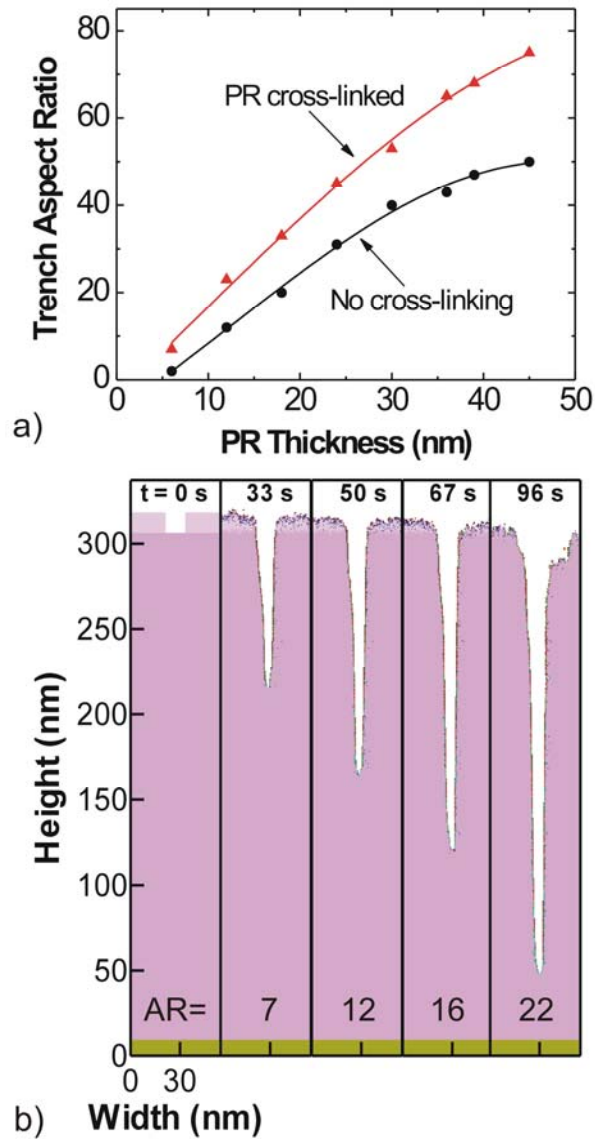


**Fig. 6.5** Correlation between trench aspect ratio and PR thickness. (a) Trench aspect ratio as a function of PR thickness without PR cross-linking (triangle dots) and with PR cross-linking (square dots); (b) Time sequence of HAR etching profiles. Before 67s (AR = 16), the CD is maintained well. After etching for 96s (AR = 22), PR is eroded and feature profile is depleted.

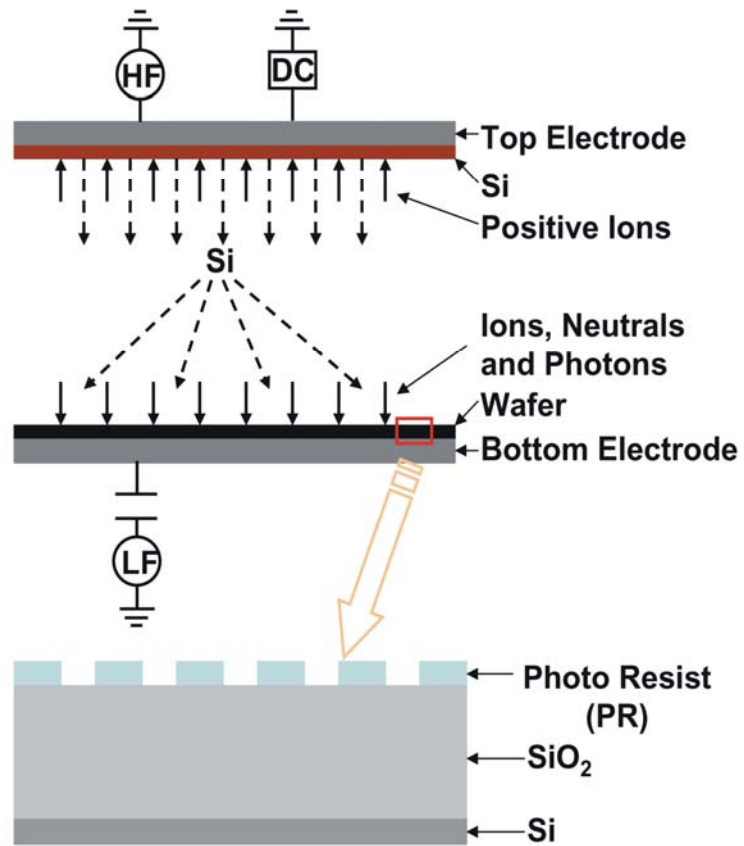


**Fig. 6.6** Schematic of Si sputtering and deposition in a dual-frequency CCP reactor with dc augmentation on the top electrode. Dc augmentation is used to enhance the sheath near top electrode and promote Si sputtering yield.

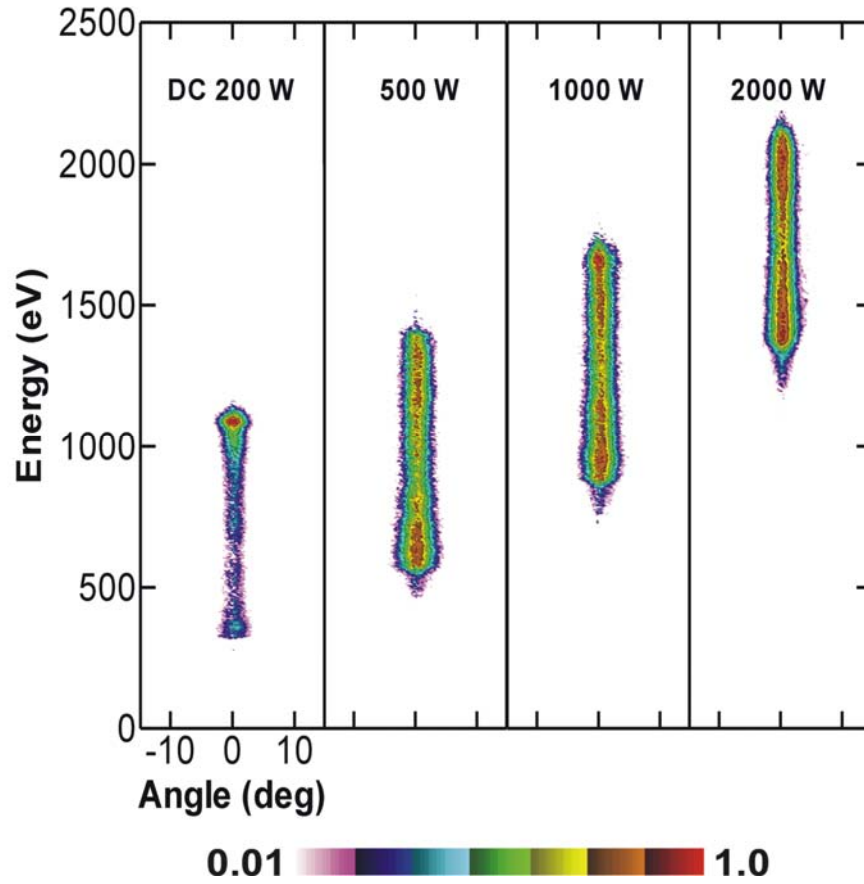


**Fig. 6.7** Total ion energy at the center of top electrode surface as a function of dc power. Dc power varies from 200 W to 2000 W. Peak of ion energy reflects the change of dc power.

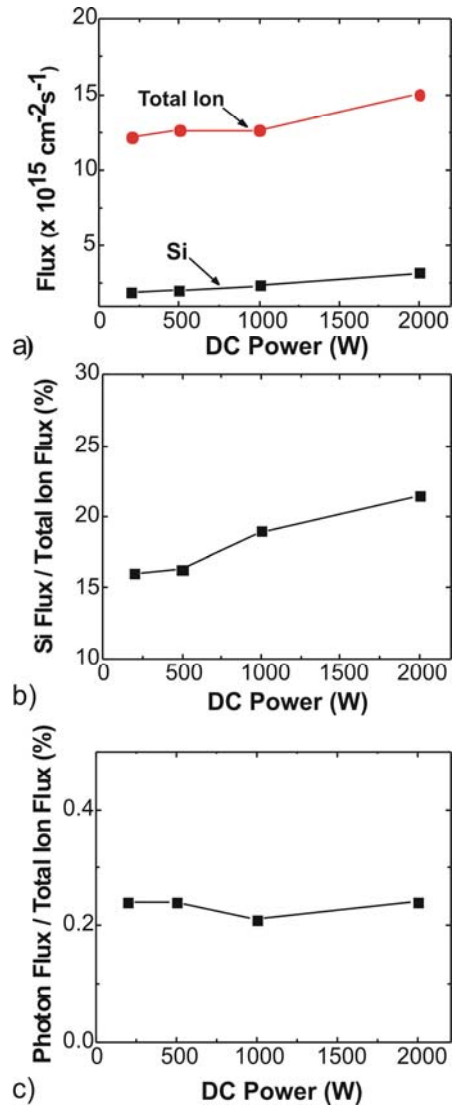


**Fig. 6.8 Particle fluxes incident onto wafer surface as a function of dc power. Total ion and Si fluxes; (b) Si / total ion flux ratio; (c) Photon (VUV) / total ion flux ratio.**

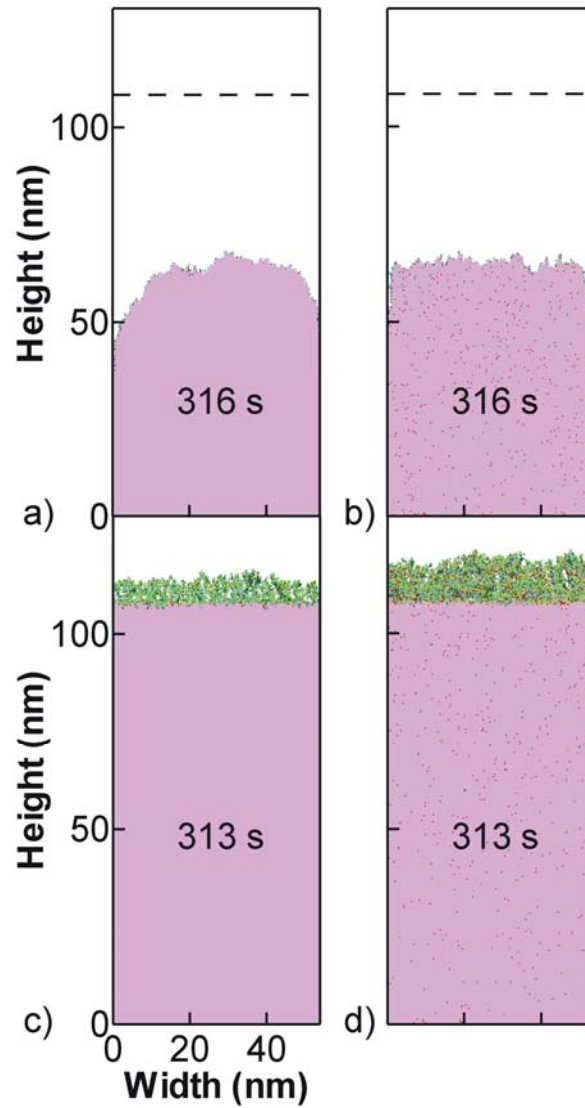


**Fig. 6.9** Comparison of PR etching rate: (a) with ion bombardment only; (b) with ion bombardment and VUV exposure; (c) with ion bombardment and Si deposition; (d) with ion bombardment, VUV exposure and Si deposition.

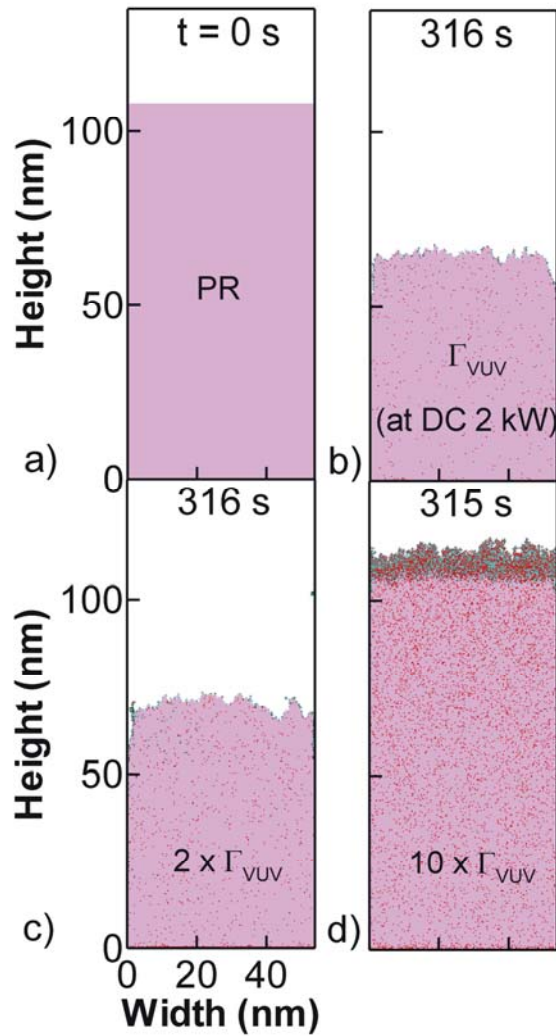


**Fig. 6.10** Quantitative investigation of VUV flux effects on etching of PR. (a) Initial profile; (b) Etching at dc 2 kW with VUV exposure (VUV flux =  $\Gamma_{VUV}$ ); (c) Etching with VUV flux =  $2\Gamma_{VUV}$ ; (d) Etching with VUV flux =  $10\Gamma_{VUV}$ .

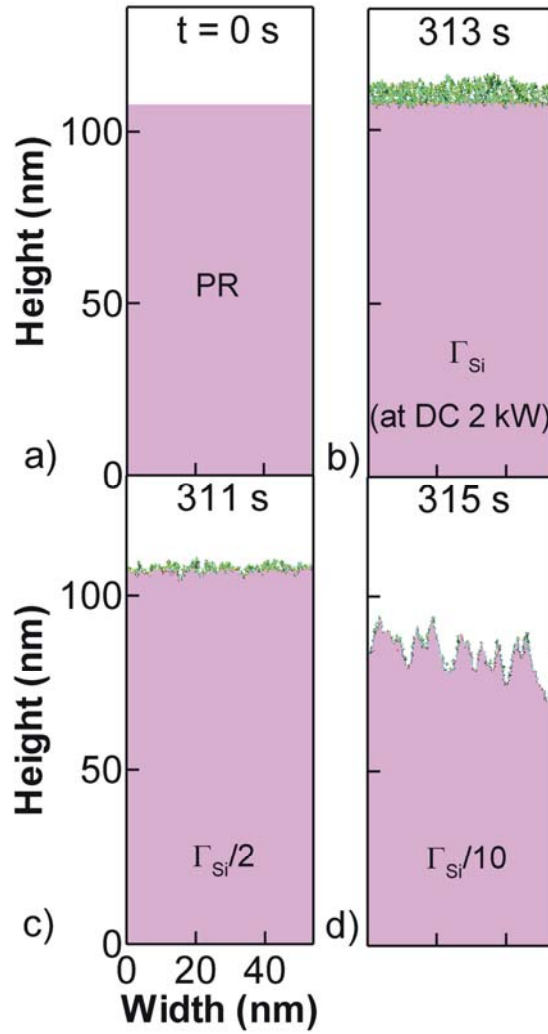


**Fig. 6.11** Quantitative investigation of Si flux effects on etching of PR. (a) Initial profile; (b) Etching at dc 2 kW with Si deposition (Si flux =  $\Gamma_{Si}$ ); (c) Etching with Si flux =  $\Gamma_{Si}/2$ ; (d) Etching with Si flux =  $\Gamma_{Si}/10$ .

## 6.6 References

1. T. Ohchi, S. Kobayashi, M. Fukasawa et al. *Jap. J. Appl. Phys.* **47**, 5324 (2008).
2. A. Matsuda, Y. Nakakubo, Y. Takao et al. *Thin Solid Films*, **518**, 3481 (2010).
3. W. Eckstein, C. Garcia-Rosales and J. Roth, *Nucl. Instrum. Methods Phys. Res. B* **83**, 95 (1993).
4. M. C. Kim, D. Shamiryan, Y. Jung et al. *J. Vac. Sci. Technol. B* **24**, 2645 (2006).
5. N. Negishi, H. Takesue, M. Sumiya et al. *J. Vac. Sci. Technol. B* **23**, 217 (2005).
6. E. Pargon, D. Nest, and D. B. Graves, *J. Vac. Sci. Technol. B* **25**, 1236 (2007).
7. M. Sumiya, R. Bruce, S. Engelmann et al. *J. Vac. Sci. Technol. B* **26**, 1647 (2008).
8. E. Pargon, M. Martin, K. Menguelti et al. *Appl. Phys. Lett.* **94**, 103111 (2009).
9. D. Nest, T. -Y. Chung, D. B. Graves et al. *Plasma Process. Polym.* **6**, 649 (2009).
10. M. J. Titus, D. Nest, T. -Y. Chung et al. *J. Phys. D: Appl. Phys.* **42**, 245205 (2009).
11. D. Nest, D. B. Graves, S. Engelmann, et al. *Appl. Phys. Lett.* **92**, 153113 (2008).

## 7. PLASMA BREAKDOWN IN INNER PORES OF THIN POROUS MEMBRANES

### 7.1 Introduction

Commercially available micro-porous polyvinylidene difluoride (PVDF, shown in Fig. 7.1) membranes, which are naturally hydrophobic, are widely used for microfilters, ultrafilters and ion-exchange membranes. The porous surfaces of PVDF membranes need to be modified to achieve specific goals, for example, to improve wettability. Chemical methods are often used to modify the internal surfaces of porous membrane surfaces for biomedical applications [1-3]. Atom transfer radical polymerization (ATRP) is used to convert PVDF into ion-exchange membranes using primary anchoring polymer (mono)layers and graft polymerization from the surfaces of the membranes [1]. PVDF porous membranes could be surface-modified via poly 3,4-dihydroxy-L-phenylalanine (DOPA) coating and subsequent heparin immobilization to improve the hemocompatibility of blood-contacting materials and form a bioacceptable surface [2]. Irreversible adsorption of poly vinyl alcohol (PVA) on PVDF membranes results in a maximum water permeability after the membranes are treated with 4% PVA solution [3].

Another method for surface modification of PVDF membranes is using plasmas [4-9]. Plasma treatment may also change the pore diameter and pore size distribution due to ablation or polymer deposition. Different gas mixtures are used to treat different polymer membranes: poly acrylonitrile (PAN) membrane in air [4], or perfluorohexane plasmas [5]; polysulfone (PSU) membrane in CO<sub>2</sub> [6], N<sub>2</sub> [7], or acrylic acid plasmas [8]; sulfonated PSU membrane in allylamine plasmas [9]. Changing of pore size or grafting

functional groups onto pore surfaces leads to higher wettability and hydrophilic surfaces in porous membranes. The advantages of plasma treatment include faster processing, less waste compare to chemical method and potentially better cleanliness.

In this chapter, electrical gas breakdown through pores of porous membranes using dielectric barrier discharges (DBD) is discussed using results from a computational investigation. The gas mixture is air with 1% humidity. The membrane thickness varies from 50  $\mu\text{m}$  to 600  $\mu\text{m}$ . The pore size ranges from 10  $\mu\text{m}$  to 100  $\mu\text{m}$ . Plasma properties are simulated using *nonPDPSIM*. Breakdown conditions will be discussed in detail.

At atmospheric or a higher pressures, and for material thickness of 100s of  $\mu\text{m}$ , approximately 100s of kV are required to break down gases inside pores according to Paschen's Law [10]. In most porous membranes, interconnectivity is 100% to allow transport of material through the membrane, and so the voltage and pressure requirements may be relaxed. The breakdown path (d of pd) could be considerably longer than the pore size or material thickness. Operation at  $\sim 10$  kV and  $\sim 1$ -2 atm may be possible with high interconnectivity, though uniformity becomes an issue. By operating at different pressures, we are able to address the plasma variability.

Plasmas at atmospheric pressure typically propagate as streamers, filamentary structures that have diameters of hundreds of microns at 1 atm. The streamers are sustained by electron impact ionization and by photoionization. In positive corona discharges, net electron motion is in the opposite direction of the desired propagation of the streamer. As a result, there is not mechanisms for electrons to move ahead of the streamer to produce ionization that propagates the streamer. Photoionization is one such

mechanism to provide these seed electrons ahead of the streamer. Since photons are emitted and absorbed in all directions, photoionization process does not depend upon the direction of the electric field and so can seed electrons ahead of the streamer. Settaouti [11] simulated the streamer development in air using Monte Carlo simulation, in which he found that photoionization is the only mechanism that the streamer can develop and propagate to the cathode. The electron clouds grow and propagate only toward the anode and the cathode-directed streamer does not appear in the absence of photoionization.

Since the diameter of the streamer is commensurate with the size of the pores, the streamer interacts with the sidewalls of the pores, which are typically made of dielectric materials (hydrocarbons). This interaction is dominantly in the form of charging the capacitance of the sidewalls. This charging creates electric fields that can oppose the propagation of the streamer. In fact, if the charging is sufficient, the streamer can be stopped. This is particularly important when the topology of the pores creates obstacles or the interconnected pores “turns corners”. In these situations, photoionization is important to provide seed electrons “around the corner” that enables a way for the streamer to propagate around and overcome the retarding electric fields produced by charging the sidewalls of the pores.

The gas mixture we used is air with 1% humidity. Photons are generated by relaxation of excited state  $N_2^*$  and then are absorbed by  $O_2$  molecules, which produces  $O_2^+$  ions and electrons. This particular photoionization process should be considered generic as the actual rate of photoionization depends on the humidity and the impurity level inside the pores. We will therefore use an effective photoionization cross section to dem-

onstrate the influence of this process in propagating the streamer. A larger photoionization cross section may help overcome obstacles such as sharp corners and narrow channels. The smallest mesh size in our modeling is  $0.1\mu\text{m}/8 = 12.5\text{ nm}$ . Since the mean free path (MFP) for particles in air at ambient pressure and room temperature is  $68\text{nm}$  [12], the Knudsen number at 6 atm is  $\frac{68}{12.5 \times 6} = 0.9 < 1$ . In most cases, the Knudsen number in our modeling is less than 0.5. So the continuum assumption of fluid mechanics is still valid in our modeling even though the meshes are very small.

## 7.2 Plasma Properties in 50- $\mu\text{m}$ -thick Membranes.

### 7.2.1 Gas Breakdown in Unconnected Pores.

Plasma properties in unconnected pores are simulated in a thin membrane which is  $50\mu\text{m}$  thick. As shown in Fig. 7.2a, gas breakdown occurs between two parallel planar electrodes. The upper electrode is negatively biased at  $-6\text{ kV}$ , and the lower electrode is grounded. The pore is located in the middle of the membrane. When applying a pressure of  $2500\text{ Torr}$ , gas breakdown is observed in the pore. The potential distribution during plasma propagation is shown in Fig. 7.2b). The electric field lines are vertical everywhere except for the gas-solid interfaces. The interface generates a small modulation to the electric field due to the different dielectric constant  $\epsilon$  for the two materials ( $\epsilon_{\text{air}}=1$ ,  $\epsilon_{\text{polymer}}=4$ ). The electron density evolution as a function of time is shown in Fig. 7.2c. Seed electrons with a density of  $10^{12}\text{ cm}^{-3}$  are applied before turning on the power. After processing for  $6.7\text{ picoseconds}$ , we can see gas breakdown happens from the top to the bottom of the pore. The plasma finally dies out at the bottom surface as the surface is

charged by the plasma. According to the Paschen Curve for air as shown in Fig. 7.3, the breakdown voltage for  $pd = 2500\text{Torr} \times 10\mu\text{m} = 2.5 \text{ Torr-cm} \approx 1 \text{ Torr-inch}$  is around 2 kV. Our simulation result 6 kV is higher than the theoretical value. This is because the humidity dependence. Increasing humidity increases breakdown voltage in air. There are also larger losses to the walls due to the large surface-to-volume ratio of the pores, which also contributes to increasing the breakdown voltage.

Five separate pores in the same membrane are then investigated as shown in Fig. 7.2d. The potential distribution in this geometry is similar to that in one single pore. Plasmas are again generated from the top of each pore and then propagate to the bottom where the plasma density reaches a peak. Then the plasma dies out after powering for 8 picoseconds due to the charging of the inside surface of the pores. Since no electron transports from one pore to another, plasma development and propagation in each pore is not dramatically affected by its neighbors. The interaction is through the deformation of the electric potential.

### 7.2.2 Gas Breakdown in Connected Pores.

In reality, polymer membranes have high porosity and the pores are highly interconnected. Six lined-up connected pores with the same size ( $10 \mu\text{m}$ ) are simulated using the same electrodes as previous cases. Fig. 7.4 shows the potential (Fig. 7.4a) and electron density (Fig. 7.4b) distribution as a function of time in the porous channel. The plasma contacts the metal electrodes which enable a current to flow through the channel without directly charging surfaces in the path of the streamer. The plasma is generated from seed electrons at the top of the first pore and then propagates to the bottom rapidly

by electron impact ionization. Once the channel is filled with plasma to make a conductive connection between the electrodes, a more intense plasma propagates upward as can be seen in Fig. 7.4a. After 0.5 ns, all inner surfaces in the porous channel are covered with plasma with a density of  $10^{10} \text{ cm}^{-3}$  or higher. This density is sufficient to provide any chemical reactions on inner pore surfaces.

Another geometry with connected pores has an angled path in the membrane as a model of pores that are not connected top-to-bottom by line-of-site (Fig. 7.5a). Unfortunately, the plasma dies out after propagating for 5 picoseconds. This is largely due to the charging of the pore surfaces which creates electric fields which retard the propagation of the streamer. With a small photoionization cross-section ( $10^{-19} \text{ cm}^2$ ), there is insufficient seeding of electrons beyond the obstacle to allow propagation of the plasmas. The lateral components of the electric field are not strong enough to pull the electrons to the second pore and produce ionization there. A larger photoionization cross section ( $10^{-14} \text{ cm}^2$ ) enables a gas breakdown throughout the pores after processing for 10 picoseconds (Fig. 7.5b). As time goes on, the plasma density keeps increasing which forms an arc in the porous channel between the two electrodes due to there being a conductive connection between the electrodes and no ballasting resistor to limit the current.

For all above cases, we used the same breakdown conditions: 2500 Torr, 6 kV, 50- $\mu\text{m}$ -thick membrane in air with 1% humidity. It is difficult to obtain breakdown when the path through the membrane has sharp angles or horizontally oriented pathways. Increasing the photoionization cross section is an effective way to solve this problem. This is not only a numerical exercise. In experiments, we can also change the photoionization

cross section by adding impurity gases (Xe for example) to the plasma that have significantly larger photoionization cross sections.

### **7.3 Gas Breakdown in Highly Interconnected Pores in 600- $\mu\text{m}$ -thick Membranes.**

The actual thickness of membranes is usually 100s of  $\mu\text{m}$ , and the pore size is usually  $\sim 100 \mu\text{m}$  and the pores are highly interconnected. A more randomly distributed porous geometry with larger pores (pore diameter  $\approx 100 \mu\text{m}$ ) in thicker membranes (600- $\mu\text{m}$ -thick) was simulated as shown in Fig. 7.6. As usual, the plasma propagates in more vertically oriented channels due to a parallel electric field. After the plasma reaches the bottom electrode surface and a conductive path is established, there is a reverse ionization wave. For a small photoionization cross section, the plasma path is established only in the pore-connected path that is near line-of-sight between the electrodes (Fig. 7.6a). This results in the electric field being shorted by the conductive path, thereby producing a smaller electric field in other more circuitous paths.. The gases in these regions do not break down due to a lack of sufficient electric field (see Fig. 7.6b).

A larger photoionization cross section ( $10^{-16} \text{ cm}^2$ ) is applied to evaluate whether it can help to ionize those non-plasma regions. It turns out that this is remarkably effective. Although the vertical pathways are still favored for plasma propagation, the seeding of electrons in the more circuitous paths enables plasma to propagate into those paths before the electric field collapses, as shown in Fig.7.6d. The collapse of the electric field is relatively uniform (see Fig. 7.6c).

Plasmas prefer to propagate vertically due to a the vertical electric field formed between two parallel planar electrodes. A round electrode on the top is proposed to be able to generate horizontal electric field lines. The top round electrode is negatively biased in air. A grounded boundary for the electric potential is located far away (800  $\mu\text{m}$ ) from the electrode so that there is no strong electric field in that region (Fig. 7.7). When the photoionization cross section is  $10^{-19} \text{ cm}^2$ , plasma propagates through a path (Fig. 7.7b) which is different from that with planar electrodes. When the photoionization cross section is increased to  $10^{-16} \text{ cm}^2$ , gas breakdown is observed in all porous channels as shown in Fig. 7.7d. Curved electric field is obtained before the plasma reaches the bottom electrode in both cases (Fig. 7.7a and Fig. 7.7c). When the plasma turns back to the top electrode, the electric field becomes more vertical again. Plasmas are also observed in the top air region surrounding the round electrode in the high photoionization cross section case. In this case, plasma density still increases after processing for 1 ns.

To avoid arcing, which might damage the membrane due to an extremely high gas temperature inside, a thick dielectric layer with a dielectric constant of  $\epsilon = 4$  is added to the bottom electrode surface. This thick dielectric at the bottom of the path charges negatively when the plasma reaches it. This charging reduces the electric field which then prevents arcing. This is, in fact, the principle behind dielectric-barrier-discharges (DBDs). As can be seen in Fig. 7.7e, plasmas require more time to reach the bottom surface (2 ns) compared to the previous case without the dielectric layer (0.6 ns). Immediately after the plasma touches the bottom dielectric layer the plasma density starts to decrease due to the smaller electric field produce by charging of the bottom dielectric. This

provides an effective way to prevent the membrane from being damaged during plasma processes under high voltage and high pressure.

#### **7.4 Gas Breakdown in Highly Interconnected Pores in 300- $\mu\text{m}$ -thick Membranes.**

The size of pores in membranes varies from a few  $\mu\text{m}$  to 100s of  $\mu\text{m}$  and is not always uniform. A challenging geometry, with 5~10  $\mu\text{m}$  wide porous channels connected and twisted with each other in a 300- $\mu\text{m}$ -thick membrane, is simulated to investigate the breakdown conditions and critical dimensions for plasma propagation. The unstructured mesh, shown in Fig. 7.8, has a refined plasma region. Three photoionization cross sections were selected to test their effects on plasma properties. Fig. 7.8 shows plasma properties with photoionization cross section:  $\sigma_{\text{ph}} = 10^{-16} \text{ cm}^2$  (left);  $\sigma_{\text{ph}} = 10^{-18} \text{ cm}^2$  (middle); and  $\sigma_{\text{ph}} = 10^{-19} \text{ cm}^2$  (right). When gas pressure is set to 3 atm with bias voltage of -15 kV on the top electrode, plasma propagation prefers the left channel as shown in Fig. 7.8a. Varying  $\sigma_{\text{ph}}$  from  $10^{-16} \text{ cm}^2$  to  $10^{-19} \text{ cm}^2$  does not produce a significant change for plasma density distribution in the porous channels. The photoionization source (Fig. 7.8b and 7.8d) reflects plasma density accordingly, which proves that photoionization is the dominant ionization mechanism in these porous channels. When gas pressure increases to 6 atm with a higher bias voltage of -30 kV, interestingly, the plasma chooses the right channel to propagate. This is because the porous channel on the right is more ‘straight’ compared to the left channel if we observe the geometry more closely. The reason why the plasma cannot go through the right channel at low pressure is because the right channel has the narrowest ‘neck’.

## 7.5 Critical Dimension for Plasma Propagation

### 7.5.1 0.1- $\mu\text{m}$ -wide ‘Neck’ without Thickness

Two operating conditions (Fig. 7.9b: 3 atm, -15 kV; and Fig. 7.9c: 6 atm, -30 kV) are compared in the same porous structure with a 0.1- $\mu\text{m}$ -wide ‘neck’. The ‘neck’ region is refined to get an accurate calculation as shown in Fig. 7.9a. For both cases, the plasma can penetrate through the ‘neck’. The only difference is that the plasma propagates faster at high pressure and high voltage. This may not be true in general. The calculated Debye length is:

$$\lambda_{De}(cm) \approx 743 \sqrt{T_e / n_e} \quad (7.2)$$

In both cases,  $T_e \approx 4 \text{ eV}$ ,  $n_e \approx 10^{16} \text{ cm}^{-3}$ . So  $\lambda_{De} \approx 1.5 \times 10^{-5} \text{ cm} = 0.15 \mu\text{m}$ , which is larger than the ‘neck’ width. The reason why plasma can still penetrate through the ‘neck’, we think, is because the ‘neck’ is zero in thickness, which is not possible in actual porous polymers. The thickness of the ‘neck’ should be taken into account.

### 7.5.2 0.1- $\mu\text{m}$ -wide and 1- $\mu\text{m}$ -thick ‘Neck’

A similar geometry is simulated with a ‘neck’ thickness of 1  $\mu\text{m}$  as shown in Fig. 7.10. The ‘neck’ region is also geometrically refined numerical accuracy. For the first case with a gas pressure of 3 atm and bias voltage of -15 kV, plasma breakdown occurs in the region above the ‘neck’. The plasma tries to penetrate through the ‘neck’ at 0.03 ns as shown in Fig. 7.10b, but it fails after the try. The plasma simply continues to develop in the upper region while no breakdown is observed in the region below the ‘neck’. The

charging of the surface produces retarding electric fields which prevent the plasma from penetrating through the neck. Since the Debye length (around  $0.15\ \mu\text{m}$ ) is commensurate with the size of the opening, the plasma is not able to be conformal to the shape of the neck. For the second case with gas pressure of 6 atm and bias voltage of -30 kV, the penetration of the plasma through the neck is slowed but if eventually passes through the 'neck' after 0.025 ns. Both the upper region and lower region develop plasmas at a comparable speed with a comparable plasma density. The higher pressure sustains a high density plasma, which reduces the Debye length and allows the plasma to be more conformal along the neck and shield out the surface charge. This enables electron transport through the neck and ultimately electron impact ionization in the lower region below the 'neck'.

## 7.6 Concluding Remarks

Gas breakdown was investigated in different pores or porous channels in membranes of differing thickness. When the thickness of the membrane is  $50\ \mu\text{m}$  with a pore size of  $10\ \mu\text{m}$ , the breakdown conditions in air (1% humidity) are: 3 atm and -6 kV. When the thickness of the membrane is  $600\ \mu\text{m}$  and the diameter of the porous channel is  $100\ \mu\text{m}$ , the breakdown conditions in the same gas are: 1 atm and -10 kV. The theoretical breakdown voltages read from the Paschen Curve in Fig. 7.3 are approximately 2 kV and 7 kV respectively, which are acceptably lower than our results due to a 1% humidity in our model, and the larger surface-to-volume ratio. Plasma propagation at sharp angles and in more horizontally-oriented porous channels needs larger photoionization cross sections to produce seed electrons beyond the obstacle. The shape, location, or the number

of electrodes may affect the electric field and, thus, the gas breakdown. Gas pressure affects the plasma density and plasma propagation paths. At higher gas pressure, plasmas may go through more straight channels with smaller critical dimensions due to their ability to produce a higher plasma density for the same  $E/N$ . The thickness of the critical dimension (or 'neck') also affects the plasma propagation. A thicker 'neck' leads to more electron loss to the walls and is less likely to allow plasma to penetrate.

## 7.7 Figures

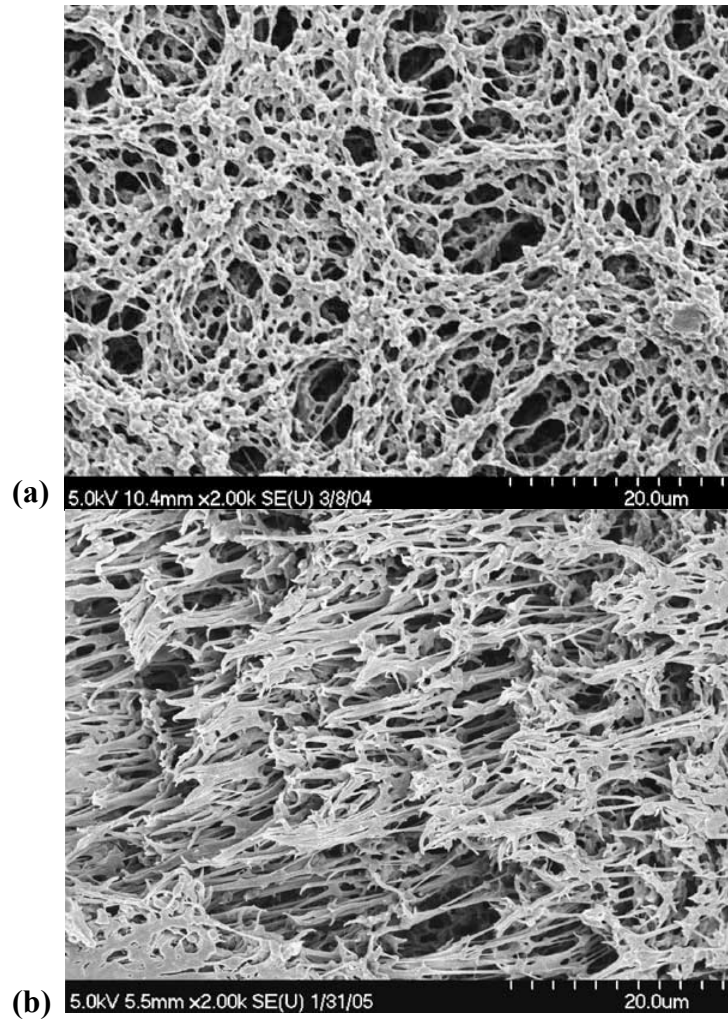


**Fig. 7.1** SEM micrographs of the unmodified PVDF membrane. (a) Surface image; and (b) Cross-sectional image [1].

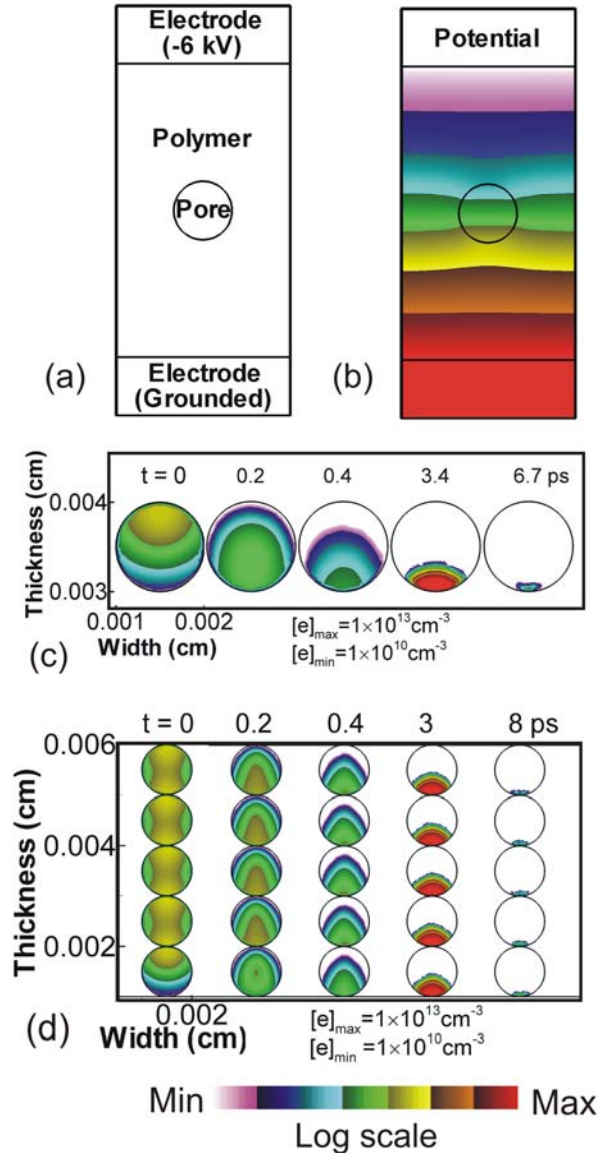


**Fig. 7.2** Plasma propagation in separate pores in porous membrane. (a) Schematic of dielectric barrier discharge with upper electrode negatively powered and bottom electrode grounded; (b) Potential distribution in the polymer with a pore in the middle; (c) Time sequence of plasma propagation in the pore; (d) Time sequence of plasma propagation in five separate pores in the polymer.

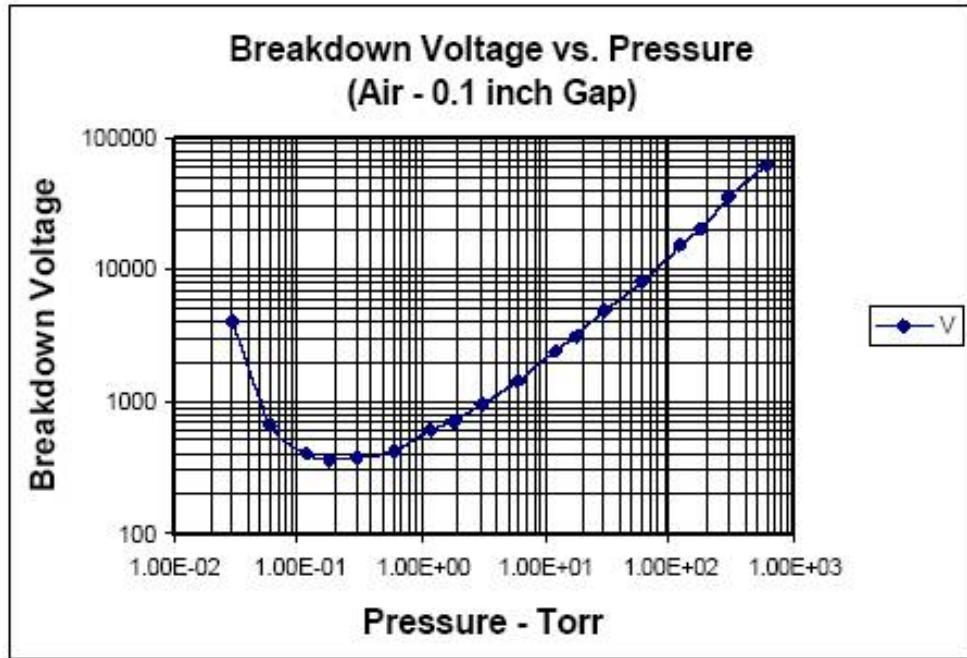


**Fig. 7.3 Paschen Curve for air between two float parallel copper electrodes separated by 0.1 inch. (Courtesy High Voltage Connection Inc.)**

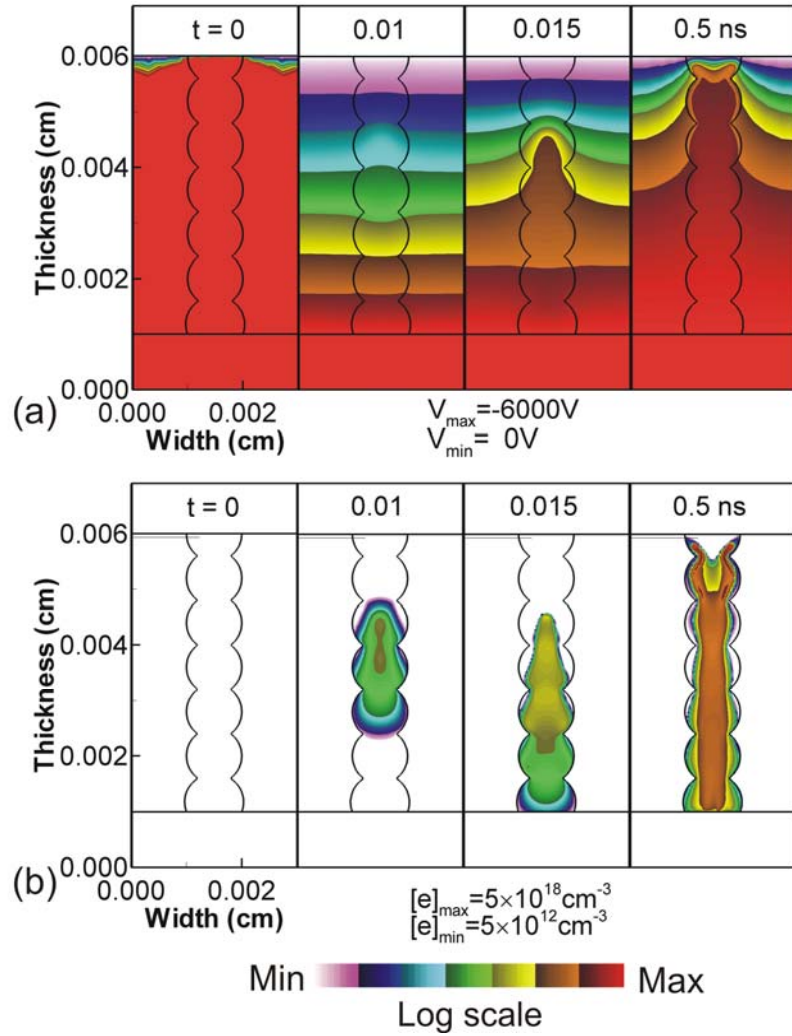


**Fig. 7.4 Plasma properties in a straight porous channel in the polymer sheet. (a) Potential distribution as a function of time; (b) Time sequence of plasma density evolution in the channel.**

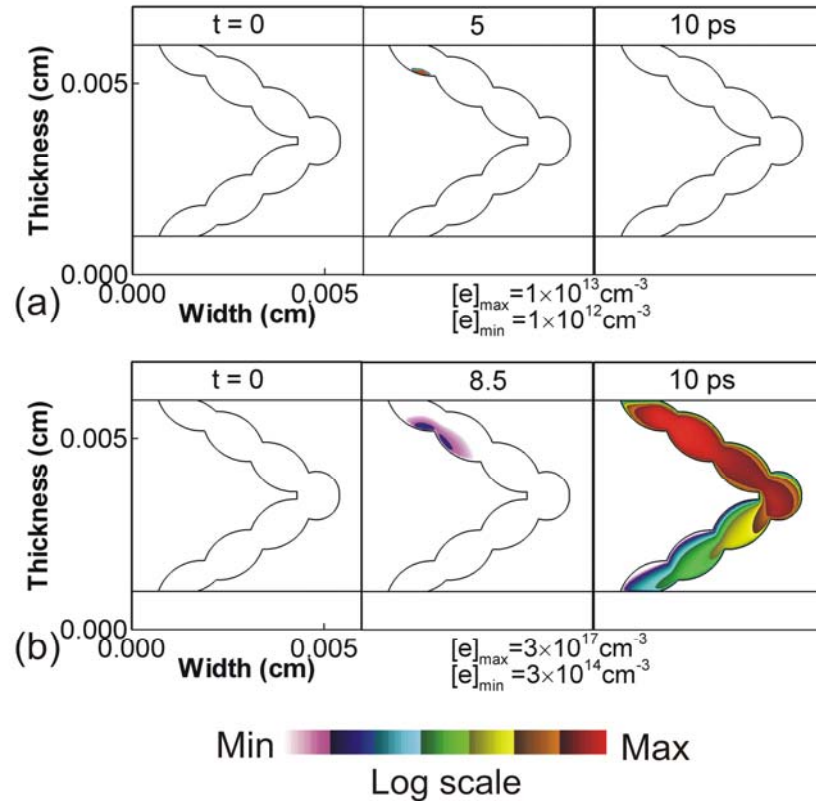


**Fig. 7.5** Plasma properties in an angled porous channel. (a) Plasma density evolution when photoionization cross section  $\sigma_{\text{ph}} = 10^{-19} \text{ cm}^2$ ; (b) Plasma density evolution when  $\sigma_{\text{ph}} = 10^{-14} \text{ cm}^2$ .

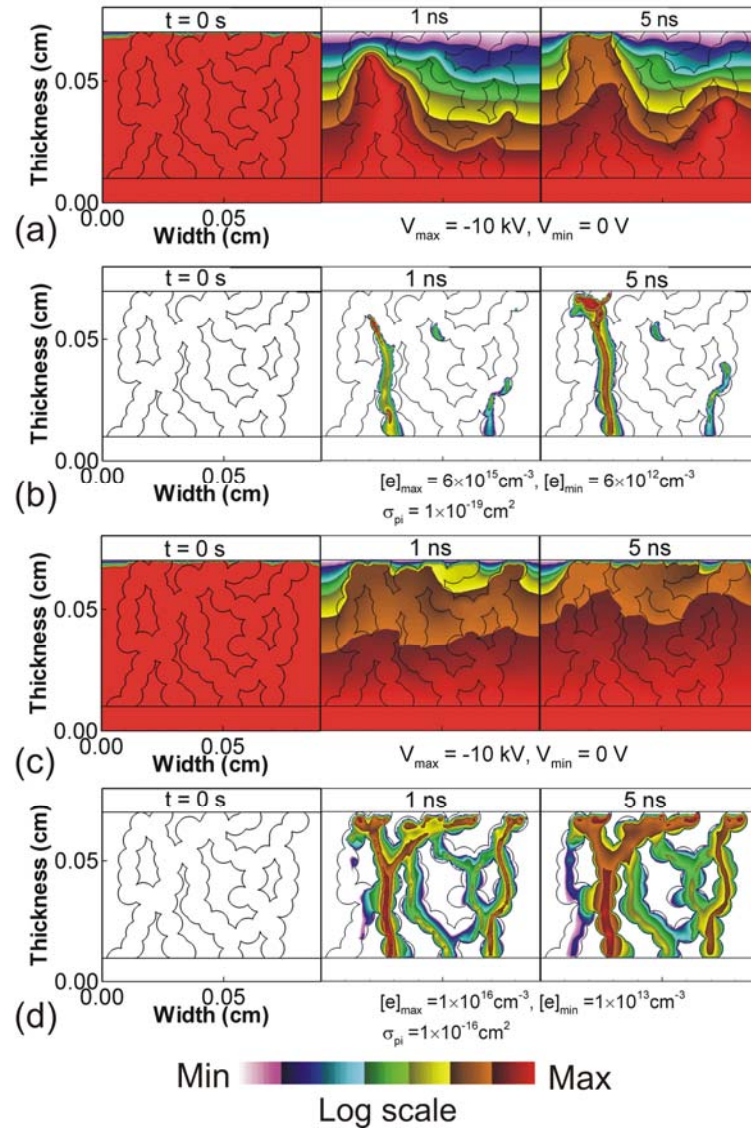


**Fig. 7.6** Plasma breakdown conditions in multiple porous channels. (a) Potential distribution when  $\sigma_{\text{ph}}=10^{-19} \text{ cm}^2$ ; (b) Plasma propagation when  $\sigma_{\text{ph}}=10^{-19} \text{ cm}^2$ ; (c) Potential distribution when  $\sigma_{\text{ph}}=10^{-16} \text{ cm}^2$ ; (d) Plasma propagation when  $\sigma_{\text{ph}}=10^{-16} \text{ cm}^2$ .

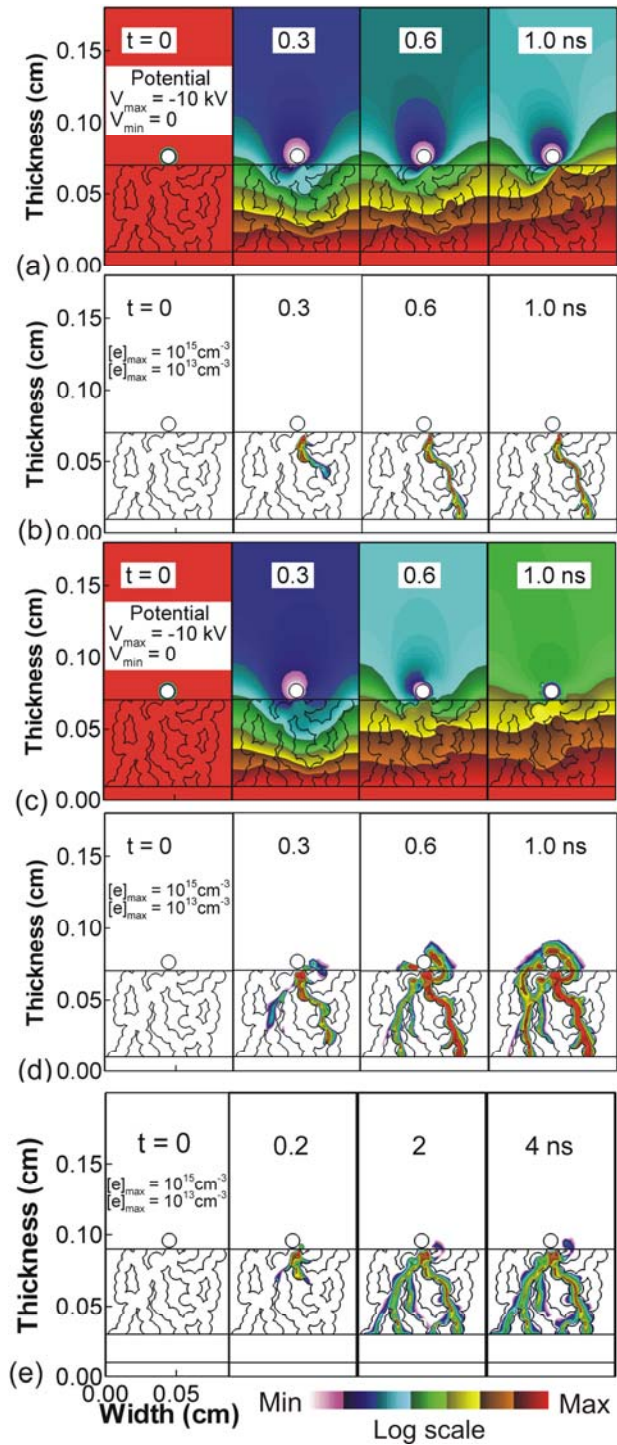


**Fig. 7.7** Plasma breakdown in multiple porous channels with a round powered electrode on the top. (a) Potential distribution when  $\sigma_{ph} = 10^{-19} \text{ cm}^2$ ; (b) Plasma density when  $\sigma_{ph} = 10^{-19} \text{ cm}^2$ ; (d) Potential distribution when  $\sigma_{ph} = 10^{-16} \text{ cm}^2$ ; (d) Plasma density when  $\sigma_{ph} = 10^{-16} \text{ cm}^2$ ; (e) Dielectric layer at bottom electrode surface can induce quenching of plasma to avoid arcing.

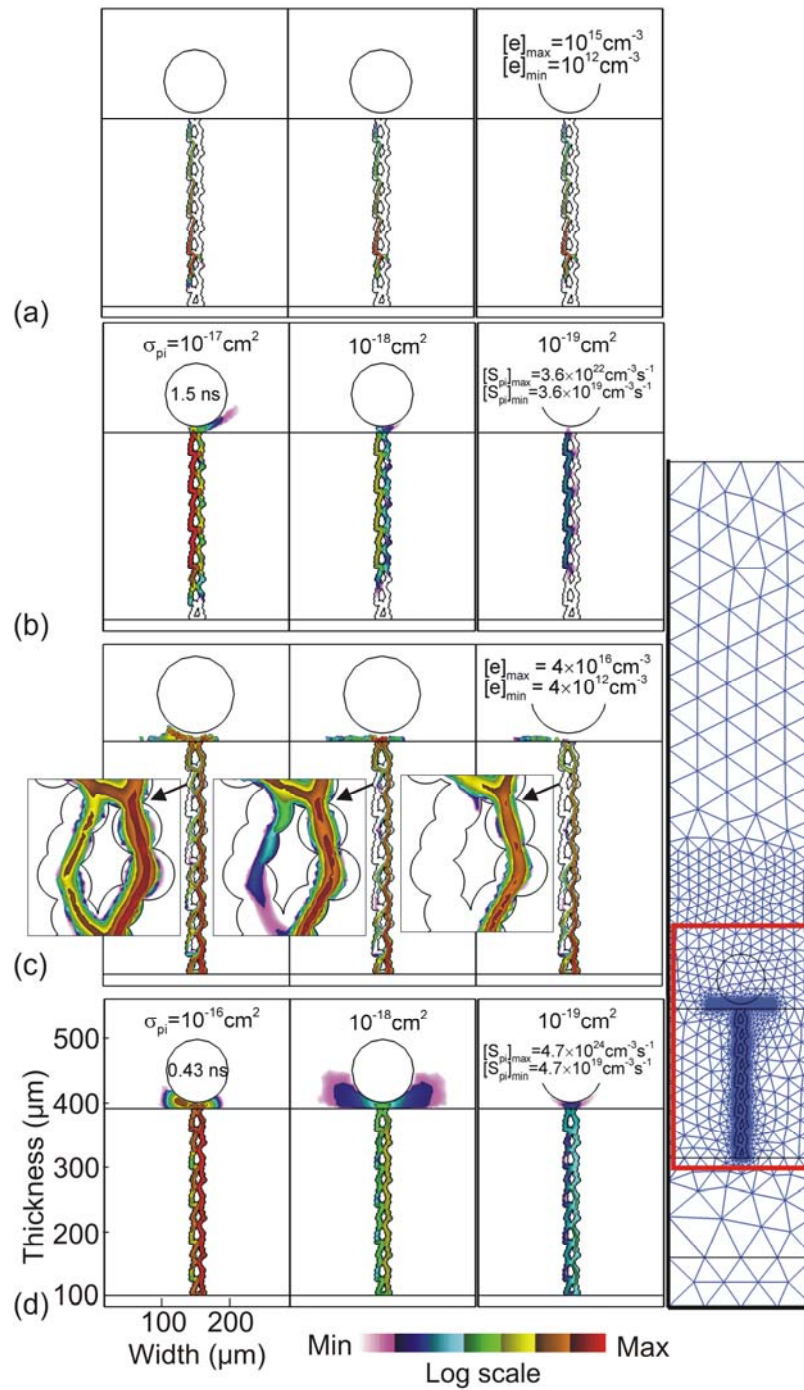


**Fig. 7.8 Plasma breakdown in 10  $\mu\text{m}$  porous channels when  $\sigma_{\text{ph}} = 10^{-16} \text{ cm}^2$ ,  $\sigma_{\text{ph}} = 10^{-18} \text{ cm}^2$ ,  $\sigma_{\text{ph}} = 10^{-19} \text{ cm}^2$ . (a) Plasma density and (b) Photoionization source at gas pressure of 3 atm and bias voltage of -15 kV; (c) Plasma density and (d) Photoionization source at gas pressure of 6 atm and bias voltage of -30 kV.**

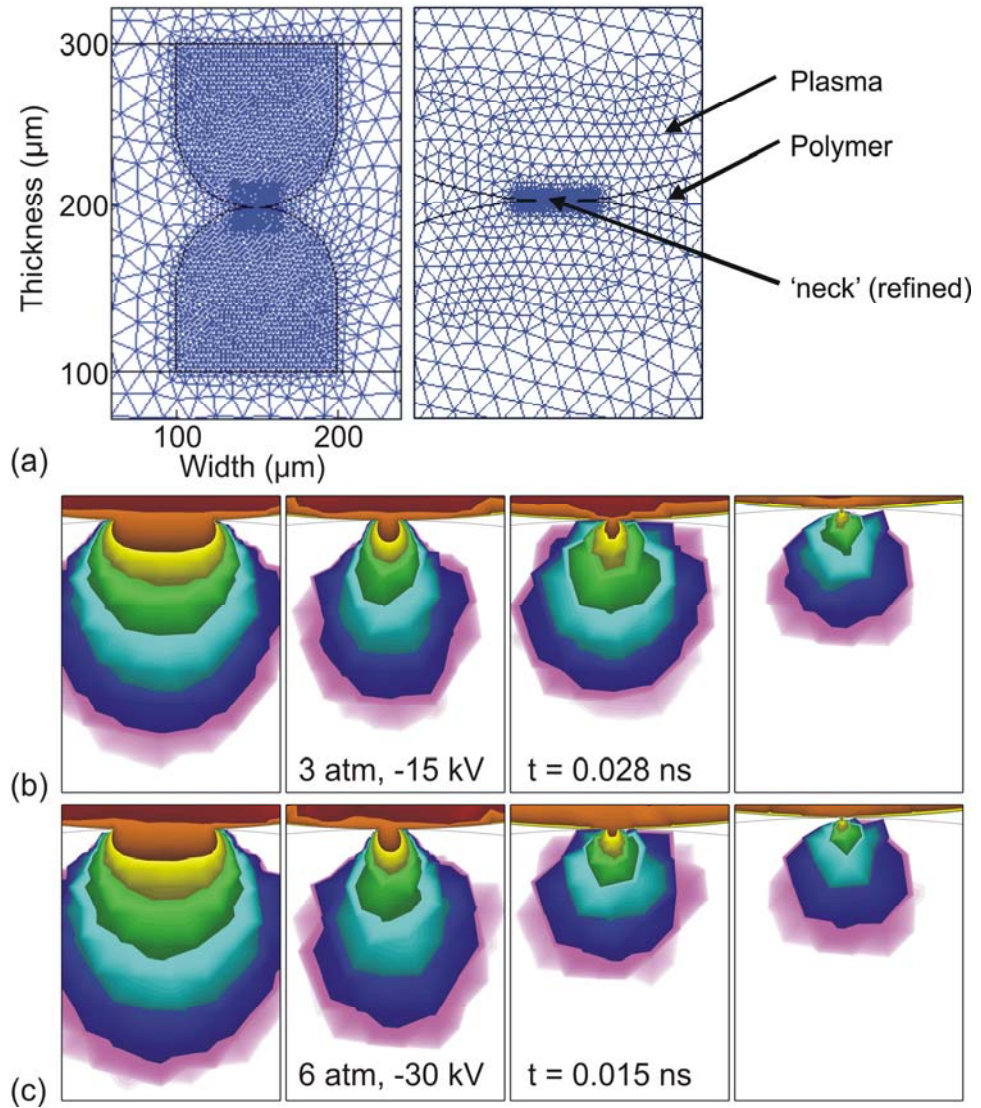


**Fig. 7.9** Plasma propagation through 100 μm porous channel with a 0.1 μm-wide-‘neck’. (a) Schematic of the numerical mesh with a refined ‘neck’ in a 100 μm porous channel; (b) Plasma propagation through the ‘neck’ at 3 atm and -15 kV; (c) Plasma propagation through the ‘neck’ at 6 atm and -30 kV.

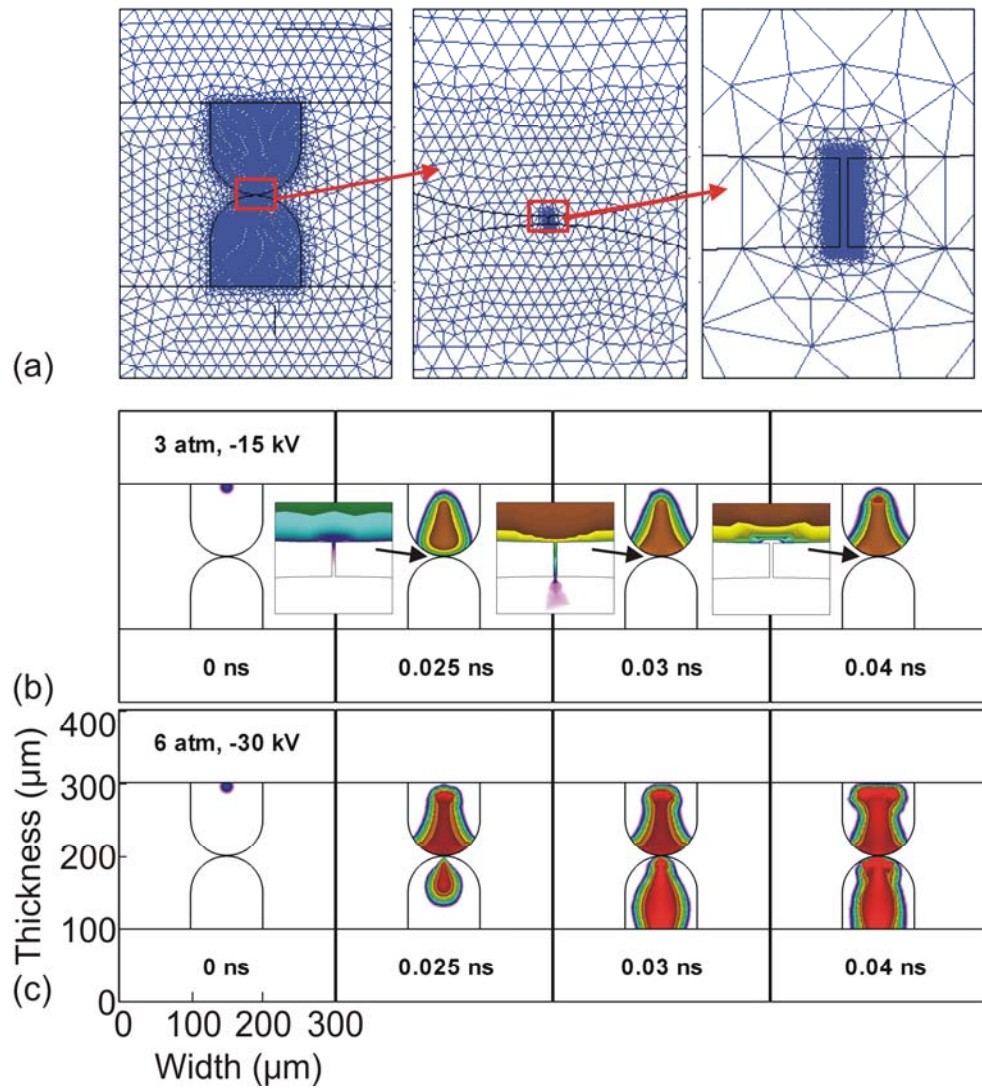


**Fig. 7.10 Plasma propagation in a 100  $\mu\text{m}$  porous channel with a 0.1  $\mu\text{m}$ -wide-'neck' with a thickness of 1  $\mu\text{m}$ . (a) Schematic of the numerical mesh with a refined 'neck' in a 100  $\mu\text{m}$  porous channel; (b) Plasma propagation through the 'neck' at 3 atm and -15 kV; (c) Plasma propagation through the 'neck' at 6 atm and -30 kV.**

## 7.8 References

1. N. Singh, S. M. Husson, B. Zdyrko, I. Luzinov, *J. Membr. Sci.* **262**, 81 (2005).
2. L. Zhu, J. Yu, Y. Xu, Z. Xi, B. Zhu, *Colloid Surface B* **69**, 152 (2009).
3. S. G. Gholap, M. V. Badiger and C. S. Gopinath, *J. Phys. Chem. B* **109**, 13941 (2005).
4. M. Bryjak, I. Gancarz, A. Krajciewicz, and J. Piglowski, *Angew. Makromol. Chem.* **234**, 21 (1996).
5. M. Bryjak, I. Gancarz, and J. Piglowski, *Env. Prot. Eng.* **19**, 113 (1993).
6. I. Gancarz, G. Poźniak, and M. Bryjak, *Eur. Polym. J.* **35**, 1419 (1999).
7. I. Gancarz, G. Poźniak, and M. Bryjak, *Eur. Polym J.* **36**, 1563 (2000).
8. I. Gancarz, G. Poźniak, and M. Bryjak, *Acta. Polym.* **50**, 317 (1999).
9. G. Poźniak, and I. Gancarz, in *Proceedings of International Conference Euromembrane '99*, **2**, 389 (1999).
10. A. Mellinger, O. Mellinger, *IEEE T. Dielect. El. In.* **18**, 43 (2011).
11. A. Settaouti, *Electr. Eng.* **92**, 35 (2010).
12. S. G. Jennings, *J. Aerosol Sci.* **19**, 159 (1988).

## **AUTHOR'S BIOGRAPHY**

Mingmei Wang was born in Qingzhou, Shandong Province, China, in 1978. She received her B.S. degree in Fine Chemical Engineering from Tianjin University, China, in 2000, and her M.S. degree in Applied Chemistry from University of Science and Technology Beijing, China, in 2006. She worked at Tianjin Power Source Institute as an assistant engineer from 2000 to 2003. Her duties were on research and development of high performance Li-ion batteries. Under the guidance of Prof. Mark J. Kushner, she has studied low pressure plasma sources for processing of semiconductor materials and atmospheric pressure plasma sources for functionalization of porous membranes since 2007. Her work has resulted in 4 refereed journal publications and 10 conference presentations. Upon graduation in June 2011 with her Ph.D. from Iowa State University, she will work with GLOBALFOUNDRIES U.S. Inc. in Malta, NY as a Principal Engineer.